TOPOLOGY OPTIMIZATION FOR EIGENVALUE PROBLEMS WITH APPLICATIONS TO PHONONIC CRYSTALS AND STOCHASTIC DYNAMICS

by

Yang Yang

A dissertation submitted to The Johns Hopkins University in conformity with the requirements for the degree of Doctor of Philosophy.

Baltimore, Maryland

May, 2016

Abstract

Topology optimization is the process of exploring the optimal layout of material within a design domain. It is a free-form technique as material can be added or removed from any location, making it more general than sizing and shape optimization. Although the first topology optimization paper was written in late 1980s, it has experienced extremely rapid expansion over the last decade. It has been applied to find optimal solutions for various engineering problems governed by diverse mechanics. However, only a relatively limited number of works have focused on problems governed by eigenvalues, and most of them have assumed deterministic eigenvalues and symmetric matrices. Therefore, this dissertation proposes topology optimization algorithms for general eigenvalue problems with and without considering uncertainties and applies them to the design of materials and structures.

The topology optimization formulation for eigenvalue problems is firstly presented and the numerical challenges are subsequently discussed. Next, the sensitivity of complex eigenvalues and eigenvectors are derived using perturbation method. Then the proposed algorithm combined with a fast mixed variational eigenvalue solver and

ABSTRACT

distributed Graphic Processing Unit computations developed by collaborators is used to reveal 3-D phononic structures which exhibit the largest normalized all-angle all-mode band gaps reported to date.

Uncertainties are considered in this dissertation for mitigating dynamic response under stochastic dynamic excitations. Stochastic equations are formulated in the standard manner by using second order differential equations and state space in which they are described by first order differential equations. Later they are solved both in frequency domain and using state space analysis. It has been found that using state space formulation and further solving in frequency domain requires the least computational effort. In addition, the by-product of this formulation is that it is capable of incorporating non-classical damping. Numerical results are presented to illustrate the comparisons between topologies optimized for stochastic ground motion loading and topologies optimized under free vibration.

Lastly, this dissertation addresses the design of reinforced concrete structure by developing a stress-dependent truss-continuum topology optimization algorithm. Stiffness is formulated such that truss elements carry only tensile forces and thus represent straight steel rebar, while the continuum elements carry only compression forces and thus represent concrete compression load paths. Constructability of reinforcement is also discussed by replacing the volume constraint with a total cost constraint.

Advisor: Dr. James K. Guest

ABSTRACT

Readers: Dr. Takeru Igusa, Dr. Michael D. Shields

Acknowledgments

Firstly, I would like to thank my advisor Dr. James Guest for his thoughtful mentoring, encouragement and patient throughout the years.

Secondly, I would like to thank Dr. Igusa and Dr. Shields for their insightful suggestions on my thesis.

Thirdly, I would like thank my family for their support all the time.

Last but not least, the author acknowledges the support of the National Science Foundation (NSF) under Grant No. CMMI-1400394. This support is gratefully acknowledged.

Dedication

This thesis is dedicated to my beloved family.

Contents

List of Figures

Chapter 1

Introduction

Structural design is crucial to almost every engineering problem. Typically, it starts with an initial guess based on engineer's past experience, and then it is modified for either minimizing cost or satisfying design criteria which inevitably requires time consuming trial and errors process. Structural optimization is a field of study to systematically perform the design process with the aid of computers, and it represents modern design methodology. More importantly, more often than not designs using structural optimization methods are found much superior to that from the trial and errors process. Based on aiming to address different optimization tasks encountered in practice, structural optimization can further be classified into three main categories.

The simplest one is the sizing optimization in which member connectivity is fixed and the design variables are usually geometrical parameters such as, length, width,

height of the part being optimized. This optimization form is very popular in design problems where the configuration has to be fixed due to the consideration of practical constraints. For example, in the design of building structures, space of beams and columns have to fall into some ranges specified by architects. However, by meeting these practical constraints, the results more or less have to sacrifice performance.

The second category of structural optimization is shape optimization. Although it allows the change of topology, topological properties have to be fixed, such as having a fixed number of holes through the design process. Designing aircraft wings or open-channel flows is among its applications in engineering problems. It is also very useful for discrete optimization in which it may require less number of design variables. In general, it is a subset of the third category, topology optimization.

Topology optimization is the process of exploring the optimal layout of material within a design domain. It is the most free-form technique compared to sizing and shape optimization which can only obtain a solution having the same topology as that of the initial design. This advantage makes topology optimization the most valuable as preprocessing tools since generally the most decisive factor for the efficiency of a novel product is the appropriate topology at the conceptual design stage. Topology optimization a relatively new field of study and the first paper is found in late 1980s. But since then, it has been rapidly expanding. In the early stages, minimum compliance design for structures was the state-of-the-art and the corresponding theoretical bases and efficient computational procedures were extensively studied. Later on,

more and more topology optimization works have been published to address various engineering design problems considering different mechanics.

In particular, eigenvalue topology optimization algorithms were developed a couple of years after the first topology optimization paper. An increasing number of related works have been found in the literature to consider different engineering applications and tackle corresponding numerical problems. In Chapter 2, we will first summarize and present the general eigenvalue topology framework. Subsequently, numerical problems, such as spurious modes, are discussed. Next the sensitivities of real eigenvalues and eigenvectors are reviewed here for the sake of deriving sensitivities for complex eigenvalues and eigenvectors. Complex eigenvalue problems appear when unsymmetric matrices are considered. For instance, the use of non-classical damping will make the damping matrix cannot be diagonalized by using real eigenvalue decomposition. In this chapter, we derived the sensitivity of complex eigenvalue and eigenvectors using a similar perturbation method used for real problems. Later in this chapter, the proposed complex eigenvalue topology optimization algorithm is applied to reveal 3-D phononic structures which exhibit the largest normalized all-angle all-mode gaps ever reported. The tough computational task is addressed by our collaborator at Illinois Institute of Technology by a combination of a fast mixed variational eigenvalue solver and distributed Graphic Processing Unit computations. At the end of this chapter, we will incorporate uncertainty analysis into the optimization formulation. Although topology optimization is the most general form of structural

optimization, solutions obtained by performing the optimization in a deterministic setting may be impractical or suboptimal when considering real-world engineering conditions with inherent variabilities including (for example) variabilities in fabrication processes and construction conditions. Such variabilites lead to uncertainties in structural geometry and/or material properties, which can result in potentially significant uncertainties in structural stiffness and mass when dynamic behavior is concerned. The proposed algorithm is very general and it is capable of handling all sources of uncertainties results in the stiffness and mass matrices.

Besides uncertainties in the material and geometry, we will explore more challenging case where the applied load is random in chapter 3. Considering random dynamic loads is of great importance when the information of that is incomplete. In other words, the applied dynamic loads cannot be simply expressed by a deterministic function of time. Various stochastic methods have been studied in this dissertation. Sensitivity analyses are performed for each method. It has been found that considering stochastic load will produce completely different topologies compared to a deterministic eigenvalue optimization.

In the appendix, topology optimization algorithm is developed for design of reinforced concrete structures. In the design of reinforced concrete structure, strut-and-tie models (STMs) are widely used by RC designers. However, selection of a viable model is a challenging task, especially in complex three-dimensional (3D) design domains with irregular cutouts, which are common in building cores and shear walls.

Therefore, topology optimization has been promoted as a means of automating the development of minimum strain energy STMs, which can lead to improved structural behavior. In the proposed algorithm, Stiffness is formulated such that truss elements carry only tensile forces and thus represent straight steel rebar, while the continuum elements carry only compressive forces and thus represent concrete compression load paths. The latter is achieved using a stress-dependent orthotropic material model. It also can be seen the force spreading phenomenon can be captured .

Chapter 2

Topology Optimization for Eigenvalue Problems

2.1 Introduction

Eigenvalues and eigenvectors are used widely in science and engineering. In civil engineering, structures from buildings to bridges have a natural frequency and vibration mode. The natural frequency is determined from an eigenvalue analysis and the vibration mode is obtained from the corresponding eigenvector. In mechanical engineering, many machines use rotational motion, such as washer and drier, centrifuges, wheels, propellers. It makes the calculation of moment of inertia very important. Since the principal axes of a rigid body can be defined by the eigenvectors of the

moment of inertia. It is very helpful to calculate the moment of inertia using eigenvalues. In chemistry, the time-independent Schroedinger equation is represented by an eigenvalue problem, and the eigenvalues are called Energy Levels. Thus it is seen that the use of topology optimization techniques for eigenvalue value problems is of great importance to engineering problems.

In a standard eigenvalue problem, for an $n \times n$ symmetric matrix $\boldsymbol{A}$, scalars λ and vectors $\boldsymbol{x}_{n\times 1} \neq 0$ satisfying $\boldsymbol{A}\boldsymbol{x} = \lambda\boldsymbol{x}$ are called eigenvalues and eigenvectors of $\boldsymbol{A}$, respectively, and any such pair, $(\lambda, \boldsymbol{x})$, is called an eigenpair for $\boldsymbol{A}$. The set of distinct eigenvalues, denoted by $\sigma(\boldsymbol{A})$, is called the spectrum of $\boldsymbol{A}$. In a generalized eigenvalue problem, for two $n \times n$ symmetric matrices $\boldsymbol{A}$ and $\boldsymbol{B}$, scalars λ and vectors $\boldsymbol{x}_{n\times 1} \neq 0$ satisfying $\boldsymbol{A}\boldsymbol{x} = \lambda\boldsymbol{B}\boldsymbol{x}$ are called eigenvalues and eigenvectors. If $\boldsymbol{B}$ is nonsingular, then the generalized problem is equivalent to $\boldsymbol{B}^{-1}\boldsymbol{A}\boldsymbol{x} = \lambda\boldsymbol{x}$ and all theory and properties of standard problem apply to $\boldsymbol{B}^{-1}\boldsymbol{A}$. In this chapter, topology optimization method is applied to optimize the above eigenvalue problems. The optimization framework is presented firstly. The objective is to optimize a specific eigenvalue or the gap between two consecutive eigenvalues. A simple volume constraint is considered to illustrate the general ideas, but it shall be emphasized that more complicated constraints e.g. stresses and/or deflections constraints should be implemented for specific applications. Regarding the eigen equation, the sensitivity of eigenvalue and eigenvector are summarized and discussed. The eigenvalue problem and sensitivity analysis are getting more complicated when the symmetry of either

$\boldsymbol{A}$ or $\boldsymbol{B}$ is not satisfied. For complex eigenvalue problem, we have two equations $\boldsymbol{Ax} = \lambda \boldsymbol{x}$ and $\boldsymbol{y}^* \boldsymbol{A} = \lambda \boldsymbol{y}^*$, the superscript * represents conjugate transpose. The complex sensitivity is derived in this chapter.

The fundamental problems associated with the general formulation is discussed next. Since the most commonly scenario is to maximize the fundamental frequency, spurious modes occurred at low density regions may appear due to the use of SIMP method, and the solutions are summarized and discussed in detail. The most challenging numerical problem appears when multiple eigenvalues are detected. General speaking, multiple eigenvalue is not differentiable and only directional derivative can be used. However, it will be shown that the eigen derivative remains valid for some special cases.

Subsequently, the topology optimization algorithms are used for free vibration and phononic band gap structures. In free vibration, we will maximize the fundamental frequency and discuss the corresponding fundamental numerical problems. Later, we will also present collaborated work about using eigenvalue topology optimization for the design of band gap material. At the end of this chapter, we will explore more interesting scenario where the matrices $\boldsymbol{A}$ amd $\boldsymbol{B}$ are non-deterministic. In order to form the uncertain topology optimization framework, perturbation method is adopted and the detail of sensitivity analysis is provided.

2.2 Topology Optimization Formulation

Generally speaking, the optimization goal is to tune a specific eigenvalue or the gap between two consecutive eigenvalues such that some performance targets are optimized. Typically, a material or a cost constraint is considered simultaneously in the optimization process.

The most common objective is to maximize the lowest eigenvalue since the number of eigenvalues is equal to the number of degree of freedoms and higher order eigenvalues can theoretically take arbitrarily large values, thus maximizing the smallest eigenvalue is more meaningful. There are many other considerations for specific practical problems, for example, in some cases all eigenvalues shall be away from a specified value as much as possible. In those cases, it is equivalently to say the goal is to maximize the lowest eigenvalue when it can do have values higher than the specified value.

The topology optimization formulation for maximizing the lowest eigenvalue is

shown below,

$$\begin{aligned}
&\max_{\rho_1,...,\rho_{Ne}} \min_{j=1,...,J} \{\lambda_j\} \\
&s.t. \quad (\boldsymbol{A} - \lambda_j \boldsymbol{B})\boldsymbol{x}_j = \boldsymbol{0}, \quad j = 1, ..., J, \\
&\boldsymbol{x}_j^T \boldsymbol{B} \boldsymbol{x}_k = \delta_{jk}, \quad j, k = 1, ..., J, \\
&\sum_{e=1}^{Ne} \rho_e v_e \leq V_{\max} \\
&0 \leq \rho_e \leq 1 \qquad \forall e \in \Omega
\end{aligned} \tag{2.1}$$

In the above formulation, $\boldsymbol{A}$ and $\boldsymbol{B}$ are assumed symmetric matrices. The first J eigenvalues are used and there is no need to compute all eigenvalues for this problem. It is also assumed that the eigenvectors are$\boldsymbol{B}$ orthonormalized, where δ_{jk} is Kronecker's delta. The symbol N_e denotes the total number of design variables. Lower and upper limits are also defined for each design variable ρ_e. V_{max} is the given available volume of solid material. However, due to its a max-min formulation, the formulation is generally discontinuous. To improve it, a scalar variable β which plays both the role of an objective function to be maximized and at the same time a variable lower bound for the lowest eigenfrequency, can be introduced and it can be stated as

the following bound formulation

$$
\begin{aligned}
&\max_{\beta,\rho_1,...,\rho_{Ne}} \quad \{\beta\} \\
&s.t. \quad (\boldsymbol{A}-\lambda_j\boldsymbol{B})\boldsymbol{x}_j=\boldsymbol{0}, \quad j=1,...,J, \\
&\qquad \boldsymbol{x}_j^T\boldsymbol{B}\boldsymbol{x}_k=\delta_{jk}, \quad j,k=1,...,J, \\
&\qquad \beta-\lambda_j\le 0, \quad j=1,...J, \\
&\qquad \sum_{e=1}^{Ne}\rho_e v_e \le V_{\max} \\
&\qquad 0\le\rho_e\le 1 \qquad \forall e\in\Omega
\end{aligned} \tag{2.2}
$$

In addition, in some scenarios the gap between two consecutive eigenfrequencies need to maximized. In this case, for example, we want to maximize the gap between two consecutive eigenfrequencies of given orders n and $n-1$ ($n>1$) many be written in the following formulation,

$$
\begin{aligned}
&\max_{\beta_1,\beta_2,\rho_1,...,\rho_{Ne}} \quad \{\beta_2-\beta_1\} \\
&s.t. \quad (\boldsymbol{A}-\lambda_j\boldsymbol{B})\boldsymbol{x}_j=\boldsymbol{0}, \quad j=1,...,J, \\
&\qquad \boldsymbol{x}_j^T\boldsymbol{B}\boldsymbol{x}_k=\delta_{jk}, \quad j,k=1,...,J, \\
&\qquad \beta_2-\lambda_j\le 0, \quad j=n,n+1,...,J, \\
&\qquad \beta-\lambda_j\ge 0, \quad j=1,...,n-1, \\
&\qquad \sum_{e=1}^{Ne}\rho_e v_e \le V_{\max} \\
&\qquad 0\le\rho_e\le 1 \qquad \forall e\in\Omega
\end{aligned} \tag{2.3}
$$

One of the assumptions in the above optimization formulations is $\boldsymbol{A}$ and $\boldsymbol{B}$ are symmetric matrices. If non-symmetric matrices are considered, the eigenvalues and eigenvectors are complex in general. Although the maximization of complex eigenvalue does not have straightforward meanings, complex eigenvalue may appear in the structural analysis and thus the sensitivity information is required, and we will derive them in the next section.

2.3 Sensitivity of Real and Complex Eigenvalues and Eigenvectors

2.3.1 Sensitivity of Real Eigenvalues and Eigenvectors

In this section the sensitivity analysis of real eigenvalues and eigenvectors is presented. These results are well known and three different approaches, adjoint, direct differentiation and perturbation methods are discussed in this section. In the literature, Adelman and Haftka (1986) surveyed methods of calculation of the sensitivities for systems with distinct eigenvalues. Fox and Kapoor (1968) expressed the eigenvector derivative as a series in the system eigenvectors.

For the adjoint method, the eigenvalue sensitivity is expressed as follows,

$$\frac{\partial \lambda_n}{\partial \rho_e} = \frac{\partial \lambda_n}{\partial \rho_e} - \frac{\partial \boldsymbol{\gamma}^T (\boldsymbol{A} - \lambda_n \boldsymbol{B}) \boldsymbol{x}_n}{\partial \rho_e} \tag{2.4}$$

where $\boldsymbol{\gamma}$ is the adjoint variable. Using the chain rule and choosing $\boldsymbol{\gamma} = \boldsymbol{x}_n$, the

eigenvalue sensitivity can be obtained as,

$$\frac{\partial \lambda_n}{\partial \rho_e} = \boldsymbol{x}_n^T (\frac{\partial \boldsymbol{A}}{\partial \rho_e} - \lambda_n \frac{\partial \boldsymbol{B}}{\partial \rho_e}) \boldsymbol{x}_n \tag{2.5}$$

In the direct differentiation method, the derivative of the characteristic equation is as follows,

$$\frac{\partial (\boldsymbol{A} - \lambda_n \boldsymbol{B}) \boldsymbol{x}_n}{\partial \rho_e} = (\frac{\partial \boldsymbol{A}}{\partial \rho_e} - \frac{\partial \lambda_n}{\partial \rho_e} \boldsymbol{B} - \lambda_n \frac{\partial \boldsymbol{B}}{\partial \rho_e}) \boldsymbol{x}_n - (\boldsymbol{A} - \lambda_n \boldsymbol{B}) \frac{\partial \boldsymbol{x}_n}{\partial \rho_e} = 0 \tag{2.6}$$

Multiplying $\boldsymbol{x}_n^T$ on both sides of the above equation, the same results can be obtained.

The first step in the perturbation method is to describe the perturbation by a set of random variables $\boldsymbol{\varepsilon}$. Let us assume, without loss of generality, that this random vector is composed of a (mean) deterministic vector $\boldsymbol{\varepsilon}^0$ and a zero mean random fluctuation vector $\Delta\boldsymbol{\varepsilon}$ as follows:

$$\boldsymbol{\varepsilon} = \boldsymbol{\varepsilon}^0 + \Delta\boldsymbol{\varepsilon} \tag{2.7}$$

For the original eigen equation, we have

$$(\boldsymbol{A}^0 - \lambda_n^0 \boldsymbol{B}^0) \boldsymbol{x}_n^0 = \boldsymbol{0}, \quad for \;\; n = 1, ..., N, \tag{2.8}$$

where $\boldsymbol{A}^0$ and $\boldsymbol{B}^0$ are the original $N \times N$ symmetric matrices, scalar λ_n^0 and vector x_n^0 are the n-th unperturbed eigenvalue and eigenvector, respectively.

For the perturbed eigen equation, we have

$$(\boldsymbol{A}(\boldsymbol{\varepsilon}) - \lambda_n(\boldsymbol{\varepsilon}) \boldsymbol{B}(\boldsymbol{\varepsilon})) \, \boldsymbol{x}_n(\boldsymbol{\varepsilon}) = \boldsymbol{0}, \quad for \;\; n = 1, ..., N, \tag{2.9}$$

Next, the perturbed parameters are approximated by using their Taylor series expansions. It is customary to choose the point about which these Taylor series are to be written to be the mean value of the random vector, $\boldsymbol{\varepsilon}$. Proceeding with this choice, the series expansions for $\boldsymbol{A}(\varepsilon)$, $\boldsymbol{B}(\varepsilon)$, $\lambda_n(\varepsilon)$ and $\boldsymbol{x}_n(\varepsilon)$ to the second order would read:

$$\boldsymbol{A}(\boldsymbol{\varepsilon}) = \boldsymbol{A}^0 + \sum_i \boldsymbol{A}^i \Delta\varepsilon^i + \frac{1}{2}\sum_i \sum_j \boldsymbol{A}^{ij} \Delta\varepsilon^i \Delta\varepsilon^j \tag{2.10}$$

$$\boldsymbol{B}(\boldsymbol{\varepsilon}) = \boldsymbol{B}^0 + \sum_i \boldsymbol{B}^i \Delta\varepsilon^i + \frac{1}{2}\sum_i \sum_j \boldsymbol{B}^{ij} \Delta\varepsilon^i \Delta\varepsilon^j \tag{2.11}$$

$$\lambda_n(\boldsymbol{\varepsilon}) = \lambda_n^0 + \sum_i \lambda_n^i \Delta\varepsilon^i + \frac{1}{2}\sum_i \sum_j \lambda_n^{ij} \Delta\varepsilon^i \Delta\varepsilon^j \tag{2.12}$$

$$\boldsymbol{x}_n(\boldsymbol{\varepsilon}) = \boldsymbol{x}_n^0 + \sum_i \boldsymbol{x}_n^i \Delta\varepsilon^i + \frac{1}{2}\sum_i \sum_j \boldsymbol{x}_n^{ij} \Delta\varepsilon^i \Delta\varepsilon^j \tag{2.13}$$

with $\boldsymbol{A}^0 = \boldsymbol{A}(\boldsymbol{\varepsilon}^0)$, $\boldsymbol{B}^0 = \boldsymbol{B}(\boldsymbol{\varepsilon}^0)$, $\lambda_n^0 = \lambda_n(\boldsymbol{\varepsilon}^0)$, $\boldsymbol{x}^0 = \boldsymbol{x}(\boldsymbol{\varepsilon}^0)$ and where by $\boldsymbol{A}^i$, $\boldsymbol{A}^{ij}$, $\boldsymbol{B}^i$, $\boldsymbol{B}^{ij}$, λ_n^i, λ_n^{ij}, $\boldsymbol{x}_n^i$ and $\boldsymbol{x}_n^{ij}$ we mean

$$\boldsymbol{A}^i = \left.\frac{\partial \boldsymbol{A}}{\partial \varepsilon^i}\right|_{\boldsymbol{\varepsilon}=\boldsymbol{\varepsilon}^0} \quad \boldsymbol{A}^{ij} = \left.\frac{\partial^2 \boldsymbol{A}}{\partial \varepsilon^i \partial \varepsilon^j}\right|_{\boldsymbol{\varepsilon}=\boldsymbol{\varepsilon}^0} \tag{2.14}$$

$$\boldsymbol{B}^i = \left.\frac{\partial \boldsymbol{B}}{\partial \varepsilon^i}\right|_{\boldsymbol{\varepsilon}=\boldsymbol{\varepsilon}^0} \quad \boldsymbol{B}^{ij} = \left.\frac{\partial^2 \boldsymbol{B}}{\partial \varepsilon^i \partial \varepsilon^j}\right|_{\boldsymbol{\varepsilon}=\boldsymbol{\varepsilon}^0} \tag{2.15}$$

$$\lambda_n^i = \left.\frac{\partial \lambda_n}{\partial \varepsilon^i}\right|_{\boldsymbol{\varepsilon}=\boldsymbol{\varepsilon}^0} \quad \lambda_n^{ij} = \left.\frac{\partial^2 \lambda_n}{\partial \varepsilon^i \partial \varepsilon^j}\right|_{\boldsymbol{\varepsilon}=\boldsymbol{\varepsilon}^0} \tag{2.16}$$

$$\boldsymbol{x}_n^i = \left.\frac{\partial \boldsymbol{x}_n}{\partial \varepsilon^i}\right|_{\boldsymbol{\varepsilon}=\boldsymbol{\varepsilon}^0} \quad \boldsymbol{x}_n^{ij} = \left.\frac{\partial^2 \boldsymbol{x}_n}{\partial \varepsilon^i \partial \varepsilon^j}\right|_{\boldsymbol{\varepsilon}=\boldsymbol{\varepsilon}^0} \tag{2.17}$$

Plugging Eqs. (2.10)–(2.13) into Eq. (2.9) and collecting terms of the same order one obtains a sequence of linear systems for the coefficients of different order in Eq. (2.9). The linear system for coefficients of zero-order is shown in Eq. (2.8), and that for the coefficients of higher order is given as follows:

$$\left(\boldsymbol{A}^0 - \lambda_n^0 \boldsymbol{B}^0\right) \boldsymbol{x}_n^i + \left(\boldsymbol{A}^i - \lambda_n^0 \boldsymbol{B}^i\right) \boldsymbol{x}_n^0 - \lambda_n^i \boldsymbol{B}^0 \boldsymbol{x}_n^0 = 0 \tag{2.18}$$

$$\begin{aligned}&\left(\boldsymbol{A}^0 - \lambda_n^0 \boldsymbol{B}^0\right) \boldsymbol{x}_n^{ij} + \boldsymbol{A}^i \boldsymbol{x}_n^j + \boldsymbol{A}^j \boldsymbol{x}_n^i - \lambda_n^0 \boldsymbol{B}^i \boldsymbol{x}_n^j - \lambda_n^0 \boldsymbol{B}^j \boldsymbol{x}_n^i - \lambda_n^i \boldsymbol{B}^0 \boldsymbol{x}_n^j \\ &- \lambda_n^j \boldsymbol{B}^0 \boldsymbol{x}_n^i + \left(\boldsymbol{A}^{ij} - \lambda_n^0 \boldsymbol{B}^{ij} - \lambda_n^i \boldsymbol{B}^j - \lambda_n^j \boldsymbol{B}^i - \lambda_n^{ij} \boldsymbol{B}^0\right) \boldsymbol{x}_n^0 = 0\end{aligned} \tag{2.19}$$

It is noted here that to solve the set of above equations one has to proceed sequentially as for example the solution to the zeroth-order problem has to be known prior to solving the first-order problem.

The sensitivity of of the n-th eigenvector is assumed to be equal to a linear combination of all N eigenvectors and the coefficient c shown below is to be determined.

$$\boldsymbol{x}_n^i = c_n^1 \boldsymbol{x}_1^0 + ... + c_n^s \boldsymbol{x}_s^0 + ... + c_n^N \boldsymbol{x}_N^0 = \sum_{s=1}^{N} c_n^s \boldsymbol{x}_s^0 \tag{2.20}$$

The normalization conditions are

$$(\boldsymbol{x}_n^0)^T \boldsymbol{A}^0 \boldsymbol{x}_n^0 = \lambda_n^0, \quad (\boldsymbol{x}_n^0)^T \boldsymbol{B}^0 \boldsymbol{x}_n^0 = 1, \quad (\boldsymbol{x}_n(\boldsymbol{\varepsilon}))^T \boldsymbol{B}(\boldsymbol{\varepsilon}) \boldsymbol{x}_n(\boldsymbol{\varepsilon}) = 1 \tag{2.21}$$

Plugging Eq. (2.20) into Eq. (2.18) and using the normalization conditions in Eq. (2.21), we can obtain the sensitivity of eigenvalue and eigenvector shown as below:

$$\lambda_n^i = (\boldsymbol{x}_n^0)^T \left(\boldsymbol{A}^i - \lambda_n^0 \boldsymbol{B}^i\right) \boldsymbol{x}_n^0 \tag{2.22}$$

$$\boldsymbol{x}_n^i = -\frac{1}{2}\left((\boldsymbol{x}_n^0)^T \boldsymbol{B}^i \boldsymbol{x}_n^0\right)\boldsymbol{x}_n^0 + \sum_{s=1,s\neq n}^{N}\left(\frac{(\boldsymbol{x}_s^0)^T\left(\boldsymbol{A}^i - \lambda_n^0 \boldsymbol{B}^i\right)\boldsymbol{x}_n^0}{\lambda_n^0 - \lambda_s^0}\right)\boldsymbol{x}_s^0 \tag{2.23}$$

If the same procedure is proceeded, we can further compute the second derivative of eigenvalue and eigenvector. That is we express $\boldsymbol{x}_n^{ij}$ as a linear combination of all unperturbed eigenvectors. By substituting that to 2.19, it can be shown that the following solutions are valid,

$$\begin{aligned}\lambda_n^{ij} =&(\boldsymbol{x}_n^0)^T\boldsymbol{A}^i\boldsymbol{x}_n^j + (\boldsymbol{x}_n^0)^T\boldsymbol{A}^j\boldsymbol{x}_n^i - \lambda_n^0(\boldsymbol{x}_n^0)^T\boldsymbol{B}^i\boldsymbol{x}_n^j - \lambda_n^0(\boldsymbol{x}_n^0)^T\boldsymbol{B}^j\boldsymbol{x}_n^i - \lambda_n^i(\boldsymbol{x}_n^0)^T\boldsymbol{B}\boldsymbol{x}_n^j \\ &- \lambda_n^j(\boldsymbol{x}_n^0)^T\boldsymbol{B}\boldsymbol{x}_n^i + (\boldsymbol{x}_n^0)^T\left(\boldsymbol{A}^{ij} - \lambda_n^0\boldsymbol{B}^{ij} - \lambda_n^i\boldsymbol{B}^j - \lambda_n^j\boldsymbol{B}^i\right)\boldsymbol{x}_n^0\end{aligned} \tag{2.24}$$

$$\begin{aligned}\boldsymbol{x}_n^{ij} =& -\frac{1}{2}\Big((\boldsymbol{x}_n^0)^T\boldsymbol{B}^i\boldsymbol{x}_n^j + (\boldsymbol{x}_n^0)^T\boldsymbol{B}^j\boldsymbol{x}_n^i + (\boldsymbol{x}_n^0)^T\boldsymbol{B}^{ij}\boldsymbol{x}_n^0 + 2(\boldsymbol{x}_n^i)^T\boldsymbol{B}^0\boldsymbol{x}_n^j + (\boldsymbol{x}_n^i)^T\boldsymbol{B}^j\boldsymbol{x}_n^0 \\ &+ (\boldsymbol{x}_n^j)^T\boldsymbol{B}^i\boldsymbol{x}_n^0\Big)\boldsymbol{x}_n^0 + \sum_{s=1,s\neq n}^{N}\frac{1}{\lambda_n^0 - \lambda_s^0}\Bigg((\boldsymbol{x}_s^0)^T\boldsymbol{A}^i\boldsymbol{x}_n^j + (\boldsymbol{x}_s^0)^T\boldsymbol{A}^j\boldsymbol{x}_n^i - \lambda_n^0(\boldsymbol{x}_s^0)^T\boldsymbol{B}^i\boldsymbol{x}_n^j \\ &- \lambda_n^0(\boldsymbol{x}_s^0)^T\boldsymbol{B}^j\boldsymbol{x}_n^i - \lambda_n^i(\boldsymbol{x}_s^0)^T\boldsymbol{B}^0\boldsymbol{x}_n^j - \lambda_n^j(\boldsymbol{x}_s^0)^T\boldsymbol{B}^0\boldsymbol{x}_n^i + (\boldsymbol{x}_s^0)^T\Big(\boldsymbol{A}^{ij} - \lambda_n^0\boldsymbol{B}^{ij} \\ &- \lambda_n^i\boldsymbol{B}^j - \lambda_n^j\boldsymbol{B}^i\Big)\boldsymbol{x}_n^0\Bigg)\boldsymbol{x}_s^0\end{aligned} \tag{2.25}$$

2.3.2 Sensitivity of Complex Eigenvalues and Eigenvector

In this section, the perturbation method used in section 2.3.1 is extended to derive the complex eigenvalue and eigenvector sensitivities. In the standard eigenvalue problem, when A is non-symmetric, the matrix multiplication (eigen decomposition) $\boldsymbol{x}^T\boldsymbol{A}\boldsymbol{x}$ is not diagonal. Thus the sensitivity given previous is not valid. The unperturbed eigenvalue problem is repeated here and it includes a right and left eigenvalue

problems shown below,

$$\boldsymbol{A}^0\boldsymbol{x}_n^0 = \lambda_n^0\boldsymbol{x}_n^0, \quad for \;\; n = 1, ..., N, \tag{2.26}$$

$$(\boldsymbol{y}_n^0)^*\boldsymbol{A}^0 = \lambda_n^0(\boldsymbol{y}_n^0)^*, \quad for \;\; n = 1, ..., N, \tag{2.27}$$

where superscript * represents conjugate transpose, the relation of right and left eigenvectors and the normalization conditions are,

$$(\boldsymbol{y}_j^0)^*\boldsymbol{x}_i^0 = \delta_{ij} \tag{2.28}$$

$$(\boldsymbol{x}_i^0)^*\boldsymbol{x}_i^0 = 1 \tag{2.29}$$

Next, the perturbed parameters are approximated by using their Taylor series expansions as before. The linear systems for the coefficients of zero order is expressed in Eqs. (2.26) and (2.27) and first order is shown below,

$$\boldsymbol{A}^0\boldsymbol{x}_n^i - \lambda_n^0\boldsymbol{I}\boldsymbol{x}_n^i + \boldsymbol{A}^i\boldsymbol{x}_n^0 - \lambda_n^i\boldsymbol{I}\boldsymbol{x}_n^0 = \boldsymbol{0} \tag{2.30}$$

$$(\boldsymbol{y}_n^i)^*\boldsymbol{A}^0 - \lambda_n^0(\boldsymbol{y}_n^i)^* + (\boldsymbol{y}_n^0)^*\boldsymbol{A}^i - \lambda_n^i(\boldsymbol{y}_n^0)^* = \boldsymbol{0} \tag{2.31}$$

where I is an $N \times N$ identity matrix. The sensitivity of of the n-th right eigenvectors is shown in Eq. (2.20), and the left eigenvectors is assumed to be equal to a linear combination of all N left eigenvectors and the coefficient b shown below are to be determined.

$$(\boldsymbol{y}_n^i)^* = b_n^1(\boldsymbol{y}_1^0)^* + ... + b_n^s(\boldsymbol{y}_s^0)^* + ... + b_n^N(\boldsymbol{y}_N^0)^* = \sum_{s=1}^{N} b_n^s(\boldsymbol{y}_s^0)^* \tag{2.32}$$

Plugging Eq. (2.20) to Eq. (2.30) and left multiply $(\boldsymbol{y}_k^0)^*$, it leads to the following expression,

$$c_n^k(\lambda_k^0 - \lambda_n^0) + (\boldsymbol{y}_k^0)^*(\boldsymbol{A}^i - \lambda_n^i \boldsymbol{I})\boldsymbol{x}_n^0 = \boldsymbol{0} \tag{2.33}$$

Plugging Eq. (2.32) to Eq. (2.31) and right multiply $\boldsymbol{x}_k^0$, it leads to the following expression,

$$b_n^k(\lambda_k^0 - \lambda_n^0) + (\boldsymbol{y}_k^0)^*(\boldsymbol{A}^i - \lambda_n^i \boldsymbol{I})\boldsymbol{x}_n^0 = \boldsymbol{0} \tag{2.34}$$

If $k = n$, the sensitivity of the complex eigenvalue is shown as:

$$\lambda_n^i = (\boldsymbol{y}_n^0)^* \boldsymbol{A}^i \boldsymbol{x}_n^0 \tag{2.35}$$

For the sensitivity of complex eigenvector, we first consider the case when $k = n$, the coefficients c_n^n and b_n^n can be derived from the following two conditions,

$$(\boldsymbol{y}_n(\boldsymbol{\varepsilon}))^* \boldsymbol{x}_n(\boldsymbol{\varepsilon}) = 1 \tag{2.36}$$

$$(\boldsymbol{x}_n(\boldsymbol{\varepsilon}))^* \boldsymbol{x}_n(\boldsymbol{\varepsilon}) = 1 \tag{2.37}$$

The linear systems for the coefficients of first order is,

$$(\boldsymbol{y}_n^0)^* \boldsymbol{x}_n^i + (\boldsymbol{y}_n^i)^* \boldsymbol{x}_n^0 = 0 \tag{2.38}$$

$$(\boldsymbol{x}_n^0)^* \boldsymbol{x}_n^i + (\boldsymbol{x}_n^i)^* \boldsymbol{x}_n^0 = 0 \tag{2.39}$$

Eq. (2.38) indicates $c_n^n + b_n^n = 0$ and Eq. (2.39) gives

$$c_n^n = -(\boldsymbol{x}_n^0)^* \sum_{s=1, s\neq n}^{N} c_n^s \boldsymbol{x}_s^0 \tag{2.40}$$

For the case when $k \neq n$, coefficient c_n^k and b_n^k are determined from Eqs. (2.33) and (2.34),

$$c_n^k = \frac{(\boldsymbol{y}_s^0)^* \boldsymbol{A}^i \boldsymbol{x}_n^0}{\lambda_n^0 - \lambda_s^0} \tag{2.41}$$

$$b_n^k = \frac{(\boldsymbol{y}_n^0)^* \boldsymbol{A}^i \boldsymbol{x}_s^0}{\lambda_n^0 - \lambda_s^0} \tag{2.42}$$

Thus, the complex sensitivity of right and left eigenvectors are,

$$\boldsymbol{x}_n^i = c_n^n \boldsymbol{x}_n^0 + \sum_{s=1, s\neq n}^{N} c_n^s \boldsymbol{x}_s^0 \tag{2.43}$$

$$(\boldsymbol{y}_n^i)^* = b_n^n (\boldsymbol{y}_n^0)^* + \sum_{s=1, s\neq n}^{N} b_n^s (\boldsymbol{y}_s^0)^* \tag{2.44}$$

2.3.3 Discussion on Multiple Eigenvalue Sensitivity

In sections 2.3.1 and 2.3.2, the key assumption is eigenvalues are distinct. When multiple eigenvalues occur, the sensitivity of eigenvalue is more challenging. To avoid multiple eigenvalues, Ma et al. (1995) developed a scalar weighted function of eigenfrequencies, so eigenvalues can be well separated. Along similar lines, Kosaka and Swan (1999) used a symmetry reduction method to reduce the size of the optimization problem which eases the difficulties in design sensitivity of repeated vibrational eigenvalues because one of the main sources of repeated eigenvalues is structural symmetry. General approaches to design sensitivity analysis of repeated eigenvalues have been published Friswell (1996), Seyranian et al. (1994) and Lund (1994). Krog and Olhoff (1999) further improved those methods. Du and Olhoff (2007) utilized an inner loop with the Method of Moving Asymptotes (MMA) to find the optimization

direction of design variables when repeated eigenvalues have been encountered. The method discussed in Friswell (1996) is summarized here and discussion of continuity is given subsequently.

$$(\boldsymbol{A} - \lambda_n \boldsymbol{B})\, \boldsymbol{x}_n = \boldsymbol{0}, \quad for \;\; n = 1, ..., N, \tag{2.45}$$

Suppose the eigensystem defined by Eq. (2.45) has a repeated root of order m. Assume that the eigenvalues are ordered so that $\lambda_1 = \lambda_2 = ... = \lambda_m$. The eigenvectors associated with these repeated eigenvalue are not unique; any linear combination of the eigenvectors is also an eigenvector. If $\boldsymbol{X}$ denotes one particular set of $\boldsymbol{B}$ normalized and orthogonal eigenvectors, so that

$$\boldsymbol{X} = [\boldsymbol{x}_1, \boldsymbol{x}_2, ..., \boldsymbol{x}_m] \tag{2.46}$$

then

$$\boldsymbol{\Psi} = \boldsymbol{X}\boldsymbol{H} \tag{2.47}$$

is also a set of $\boldsymbol{B}$ normalized, orthogonal eigenvectors for any orthogonal matrix $\boldsymbol{H}$. Thus, we may start with an arbitrary set of eigenvector,$\boldsymbol{\Psi}$, and transform this set to any other valid set of eigenvectors using the matrix $\boldsymbol{H}$. It should be noticed that different set of $\boldsymbol{\Psi}$ will not produce the same sensitivity result if Eq. (2.22), which is only valid for distinct eigenvalues, is used. When the eigenvalue derivative is required the correct set of eigenvectors mush be chosen. This corresponds to choosing the correct transformation, $\boldsymbol{H}$, that is consistent with the design parameter that is

varied. As the parameter of interest varies the eigenvalues may separate and produce distinct eigenvalues and their associated, unique mass normalized eigenvectors. The eigenvectors must be chosen to anticipate this separation of the eigenvalues. This approach can be formalized by calculating the derivative of the ith eigenvector, $\boldsymbol{\psi_i}$. Thus we have

$$\boldsymbol{\psi_n} = \boldsymbol{\Psi h}_n \tag{2.48}$$

where $\boldsymbol{h}_i$ denotes the ith column of $\boldsymbol{H}$. Differentiating Eq. (2.45), using Eq. (2.48) and premultiplying $\boldsymbol{X}^T$ yields,

$$\boldsymbol{X}^T \left(\boldsymbol{A}^i - \boldsymbol{\lambda}_n \boldsymbol{B}^i \right) \boldsymbol{X h}_n = \boldsymbol{\lambda}_n^i \boldsymbol{h}_n \tag{2.49}$$

It can be seen that the columns of $\boldsymbol{H}$ are the eigenvectors of the matrix $\boldsymbol{X}^T \left(\boldsymbol{A}^i - \boldsymbol{\lambda}_n \boldsymbol{B}^i \right) \boldsymbol{X}$. The eigenvalues of this matrix are the eigenvalue derivatives, $\boldsymbol{\lambda}_n^i$. Two points should be noted. Any eigenvector may be multiplied by a constant to produce another eigenvector. In this case the orthogonality of $\boldsymbol{H}$ implies that $\boldsymbol{h}_n$ must be of unit length. The second points concerns repeated eigenvalues of Eq. (2.49), which means that at least two of the eigenvalue derivatives of the original problem are equal. The vector $\boldsymbol{h}_n$, and hence the matrix $\boldsymbol{H}$, are not unique. In this case the second derivatives must be considered to determine the choice of eigenvector basis.

Once the matrix $\boldsymbol{H}$ has be found then the eigenvalue derivatives are given by

$$\mathbf{diag}(\lambda_1^i, \lambda_2^i, ..., \lambda_m^i) = \boldsymbol{\Psi}^T \left(\boldsymbol{A}^i - \boldsymbol{\lambda}_n \boldsymbol{B}^i \right) \boldsymbol{\Psi} \tag{2.50}$$

The eigenvector derivatives may now be calculated using extension to Nelson's method(Ojalvo (1987), Mills-Curran (1988), Mills-Curran (1990) and Dailey (1989)).

In the above method, in general, the set of eigenvectors will be different for each design parameter. Eigenvalue continuity and differentiability can be shown to hold if the mode shape can be tracked which means the sensitivity shown in (2.50) is updated correctly according each vibration mode. The basic idea is the eigenvalues should really be associated with physical modes, not ordered by their magnitude. For a physical example, suppose a cantilever beam has dimensions so that the frequency of its second bending mode coincides with that of its first longitudinal mode. Suppose further that the cross-sectional area of the beam is taken as the design parameter. If the cross sectional area is reduced then the frequency of the bending mode will be lower than the longitudinal mode. If the area is increased then the frequency of the bending mode will be higher. If the modes are ordered by magnitude then the bending and longitudinal modes will swap when going from a smaller cross sectional area to a larger area. Thus eigenvalues must be associated with physical modes if eigenvalue continiuity and differentiability are to be satisfied. A similar effect effect also occurs when more than one design parameter is varied(Friswell (1996)).

Eigenvector sensitivity is more complected and if the changes to the system are a function of a single design variable then continuity and differentiability can be shown to hold. If more design parameters are varied simultaneously the situation is further more complicated. In particular, the eigenvectors are not necessarily continuous

functions of the design parameters. This arises because of the transformation, $\boldsymbol{H}$ defined in Eq. (2.47), required to obtain the eigenvector basis for changes to a single parameter. In general, this transformation will be different for each design parameter. For continuity the eigenvectors should be the same by varying different design parameters(Friswell (1996)).

2.4 Application in Vibration Problems

2.4.1 Introduction

Regarding topology optimization for vibration problems, early work focused largely on optimizing structures for free vibrations, which mathematically equates to an eigenvalue optimization problem. By properly tuning the natural frequencies, the dynamic response could be substantially mitigated. Diaz and Bendsøe (1992) first maximized the natural frequencies with a given volume constraint. Subsequently, Soto and Diaz (1993) optimized the layout of plate structures by minimizing a function of the structures natural frequencies. In the above two papers, optimization results were obtained using optimality criteria method, and the first use of mathematical programming method for maximization of the natural frequencies was proposed by Tenek and Hagiwara (1993). Later a more concise method using only one variable to indicate the material properties, the density method, was developed by Kawabe and Yoshida (1996) for the maximization of natural frequencies. Constrained adap-

tive topology optimization technique and evolutionary methods are implemented for free vibration problems by Belblidia and Bulman (2001). As an alternation to the popular SIMP method, the level-set method for vibration and multiple loads structural optimization was developed by Allaire and Jouve (2005). Finally, to reduce the computational effort of topology optimization for free vibrations, Bogomolny (2010) used a combined approximations method which is based on the integration of several concepts and methods, including matrix factorization, series expansion, and reduced basis. In recent papers, Bruggi and Taliercio (2012) and Niu et al. (2009) performed topology optimziation for maximum fundamental eigenfrequency of structures composed of micropolar solids and cellular material, respectively.

Apart from the maximization of the natural frequencies, topology optimization of mode shapes has also been considered for free vibration problems (Pedersen (2000)). However, since the mode shape may change during optimization iterations, it is necessary to track the modes when maximizing a specific natural frequency as proposed by Kim and Kim (2000).

There are many challenges to solving the free vibration, or eigenvalue/ eigenvector optimization problem. A key difficulty is the non-smoothness of repeated eigenvalues. The solutions are discussed in section 2.3.3. Another challenge in solving eigenvalue optimization problems are localized or spurious modes that arise numerically from low-density elements. To eliminate those artificial modes, Pedersen (2000) linearized the stiffness for low-density regions while Tcherniak (2002) removed the mass as-

sociated with low-density elements. Similarly, Du and Olhoff (2007) used different penalization powers on structural stiffness and mass matrices to prevent spurious modes which is the method we employ here with slight modifications.

Although dynamic forces are not considered in free vibration problems, the above algorithms provide the basic tools for more complex forced vibration problems which have also been studies extensively. Under forced vibration, the frequency response optimization problem is often of primary concern. Ma et al. (1993), Ma et al. (1995), Calvel and Mongeau (2005), Jensen (2007), and Shu et al. (2011) applied topology optimization to find the stiffest structures against a single specified frequency or range of excitation frequencies by minimizing the dynamic compliance.

More general cases with periodic loading are studied by Jog (2002). Olhoff and Du (2013) considered topological design for minimum dynamic compliance subjected to harmonic periodic loading. Yang and Li (2013) also minimized dynamic compliance of a bi-material plate in a thermal environment. Practically speaking, problems possessing solutions in the form of analytical frequency response functions for periodic excitation are rare. Structures subjected to arbitrary loading, on the other hand, require numerical integration schemes such as those proposed by Min et al. (1999). Since the computational effort is generally very expensive for dynamic problems, efficient methods using modal reduction schemes were developed by Yoon (2010).

Properly designed dampers and active control devices may also attenuate the frequency response dramatically. For example, optimal configuration of viscous dampers

in a structure to mitigate vibrations has been considered such as in Taflanidis and Scruggs (2010) and Gidaris and Taflanidis (2015). However, this problem has not been addressed using topology optimization. Ou and Kikuchi (1996) proposed an integrated design procedure for structural, control and actuator locations designs, and dynamic response based on optimized structures are compared. Tcherniak (2002) developed topology optimization algorithms for placement of resonating actuators to counter vibrations. Kang et al. (2012) have used topology optimization to optimize damping layers for shell structures.

2.4.2 Topology Optimization Formulation for Free Vibration Problems

Topology optimization formulation for free vibration problems is discussed in this section. According to the SIMP model, the finite element elasticity matrix E_e is expressed in terms of the element volumetric material density ρ_e, $0 \leq \rho_e \leq 1$, in a power p, $p \geq 1$, as

$$E_e(\rho_e) = \rho_e^p E_e^* \tag{2.51}$$

where E_e^* is the elasticity matrix of a corresponding element with the fully solid elastic material the structure is to be made of. The power p is a penalization factor and it is usually gradually increased from 1 to 5 during the optimization process.

The finite element stiffness and mass matrices used are slightly modified and

expressed as

$$\boldsymbol{K}_e(\rho_e) = (\rho_e^p + \rho_{min}^k)\boldsymbol{K}_e^* \tag{2.52}$$

$$\boldsymbol{M}_e(\rho_e) = (\rho_e^q + \rho_{min}^m)\boldsymbol{M}_e^* \tag{2.53}$$

where $\boldsymbol{K}_e^*$ and $\boldsymbol{M}_e^*$ represent the element stiffness and mass matrices corresponding to fully solid material, respectively. The power q is a penalization factor associated with mass matrix. It is used to avoid spurious modes or localized modes. The reason is that for low density regions, the use of p higher than 1 will substantially decrease the stiffness while the mass is kept unchanged without q. The outcome is that the eigenvalues associated with these spurious modes becomes extremely small and they will dominate in the objective function. Du and Olhoff (2007) proposed to use the below interpolation scheme to get rid of spurious modes.

$$\boldsymbol{M}_e(\rho_e) = (\rho_e + \rho_{min}^m)\boldsymbol{M}_e^*, \quad \rho > 0.1 \tag{2.54}$$

$$\boldsymbol{M}_e(\rho_e) = (10^5\rho_e^6 + \rho_{min}^m)\boldsymbol{M}_e^*, \quad \rho \leq 0.1 \tag{2.55}$$

In Du and Olhoff (2007), ρ_{min}^k and ρ_{min}^m are set to zero, so it may produce a trial solution that when the entire domain is full of void elements, the frequencies tend to be artificially large. The use of these lower bounds higher than zero combined with Heaviside Projection Method will provides a upper bound on the ratio of stiffness to the mass matrix which generally represents frequencies. With the material interpolation scheme shown in Eqs. (2.52), (2.54) and (2.55) and the bound formulation

Eq. (2.2), the topology optimization formulation for maximizing the fundamental natural frequency can be stated as,

$$\begin{aligned}
&\max_{\beta,\rho_1,...,\rho_{Ne}} \quad \{\beta\} \\
&s.t. \quad (\boldsymbol{K} - \lambda_j \boldsymbol{M})\boldsymbol{\phi}_j = \mathbf{0}, \quad j = 1, ..., J, \\
&\qquad \boldsymbol{\phi}_j^T \boldsymbol{M} \boldsymbol{\phi}_k = \delta_{jk}, \quad j, k = 1, ..., J, \\
&\qquad \beta - \lambda_j \leq 0, \quad j = 1, ...J, \\
&\qquad \sum_{e=1}^{Ne} \rho_e v_e \leq V_{\max} \\
&\qquad 0 \leq \rho_e \leq 1 \qquad \forall e \in \Omega
\end{aligned} \tag{2.56}$$

where λ_j equals the square of the j-th circular natural frequency, ϕ_j is the corresponding vibration modes.

2.4.3 Numerical Examples

The first example is a fixed-fixed beam, and the design objective is to maximize the fundamental eigenfrequency for a prescribed 50% material volume fraction. The design domain is shown in Fig. 2.1. The length to height ratio is 8. The material is isotropic with Young's modulus $E = 10^7$, Poisson's ratio $\nu = 0.3$, and mass density $\rho_m = 1$. The optimized result is shown in Fig. 2.2. The optimized frequency is 395 rad/s. It is seen that the first frequency has been increased a lot while only half of entire volume is used. Also, it should be mentioned that multiple eigenvalues have been found (The vibration modes are shown in Figs. 2.3 and 2.4) and when it

occurs the rate of increase of frequency is very slow due to the ignorance of multiple eigenvalues in the algorithm (Fig. 2.5). In Du and Olhoff (2007), the optimal result is 456.4 rad/s by improving the algorithm for multiple eigenvalues. Their algorithm is similar to 2.3.3, but it should be emphasized that generally only directional derivative exits and multiple eigenvalue is non-differentiable.

Figure 2.1: Design domain of a fixed-fixed beam

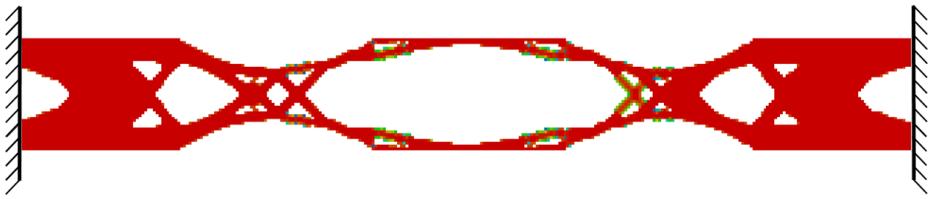

Figure 2.2: Optimized result for fixed-fixed beam

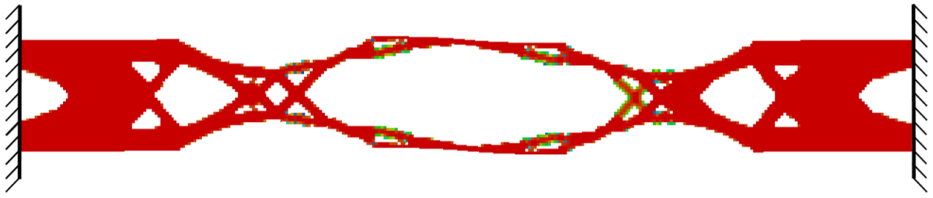

Figure 2.3: First vibration mode

The effect of ρ^k_{min} and ρ^m_{min} is investigated next. From Fig. 2.6 it is seen that when a constant material density is used for the entire domain (cases 1, 2 and 4), the

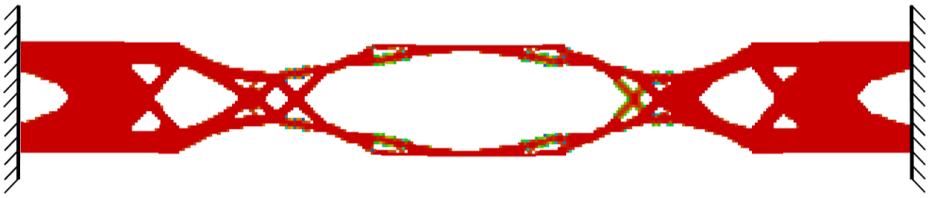

Figure 2.4: Second vibration mode

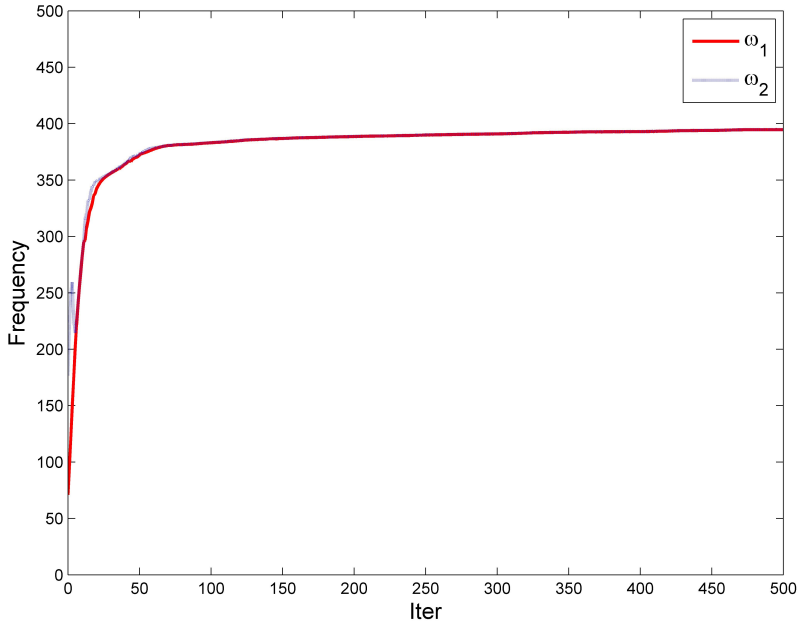

Figure 2.5: Optimization history for fixed-fixed beam

natural frequencies are kept unchanged if no penalization is applied to the stiffness and mass matrices. This observation is completely different from the popular minimum compliance problems where higher value of ρ_e will lead to smaller compliance value. When SIMP is implemented as is shown in case 3, having intermediate density will lead to much lower frequencies, so that a binary solution can be obtained. However, if ρ_{min}^k and ρ_{min}^m are set equal to 0 (Du and Olhoff (2007)), we can see the frequencies are actually arbitrarily large. This will produce a trial solution and indicates that optimal solution is achieved when the entire domain is full of void elements. In Du and Olhoff (2007), it also suggests to use a lower bound on the material density ρ_e, e.g. $\rho_e \geq 0.001$. However, it is seen that this lower bound is closely related to the penalization factors p and q. It is very common that high penalization factors are required to obtain a clear binary solution for dynamic problems, and potentially using a fixed value of lower bound will produce very small coefficients in stiffness and mass matrices, therefore this method is very sensitive to numerical problems.

When nonzero values of ρ_{min}^k and ρ_{min}^m are used, it can be seen the trial solution is eliminated. For the case when $\rho_{min}^k = \rho_{min}^m$ (cases 6 and 8), the natural frequencies are the same as the cases without SIMP. If smaller value is assigned to ρ_{min}^m, the ratio of stiffness to mass for a void element becomes less, thus it indicates the solution with full of void elements is not favored and have a much lower frequencies.

The above conclusions are obtained by assuming a uniform distribution of material density with considering different density values. In the following examples, $\rho_{min}^k =$

$\rho^m_{min} = 1e^{-6}$ is used.

CASE	ρ	$\rho^k_{\min}$	$\rho^m_{\min}$	p	q	ω_1 (rad/s)	ω_2 (rad/s)	ω_3 (rad/s)
1	1	0	0	1	1	291	725.9	1245.1
2	0.5	0	0	1	1	291	725.9	1245.1
3	0.5	0	0	3	6	145	363	622.5
4	0.001	0	0	1	1	291	725.9	1245.1
5	0.001	0	0	3	6	29100	72590	124510
6	0.001	0.001	0.001	3	6	291	725.9	1245.1
7	0.001	0.0001	0.01	3	6	29.1	72.59	124.51
8	0.001	0.000001	0.000001	3	6	291	725.9	1245.1

Figure 2.6: The effect of ρ^k_{min} and ρ^m_{min}

In the second example, we consider a cantilever beam with a concentrated mass on the free end shown in Fig. 2.7. The concentrated mass is equal to 10% of the total mass when the entire domain is full of solids. The design domain is discretized by a rectangular mesh of 160 by 80, namely 12800 four-node plain stress continuum elements. The optimized result is plotted in Fig. 2.8. The first two vibration modes are shown in Figs. 2.9 and 2.10. It is seen that the first mode is bending mode, and in the optimized result we can see materials are placed in the top and bottom regions near the supports which makes it much stiffer in this mode. In the second mode (2.10), it is a longitudinal mode, and it is also seen its natural frequency is always higher that in the bending mode, thus it proves that mode swap and multiple eigenvalue do not appear for this problem.

The effect of ρ^k_{min} and ρ^m_{min} is also investigated for this example. It is found the final topologies are slightly different when different values of the lower bounds are utilized. However, in general, we can conclude that the difference is so small, that it

Figure 2.7: Design domain of a cantilever beam with concentrated mass

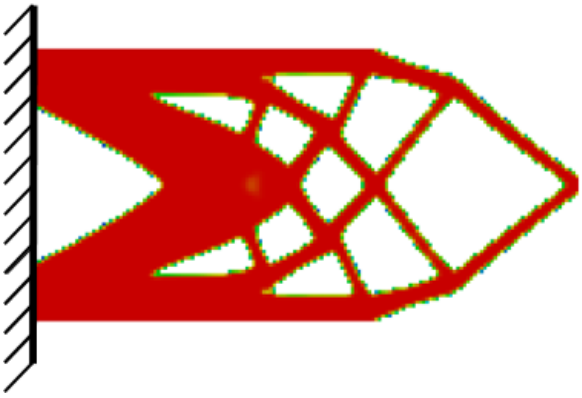

Figure 2.8: Optimized result for cantilever beam with concentrated mass ($\omega_1 = 0.5299 rad/s$)

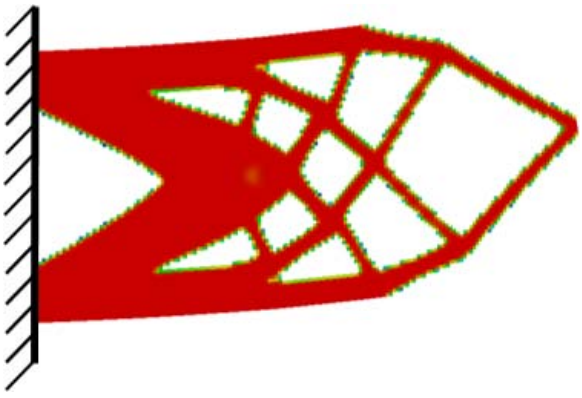

Figure 2.9: First vibration mode

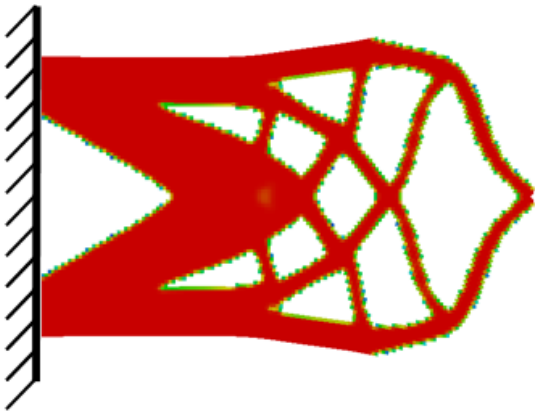

Figure 2.10: Second vibration mode

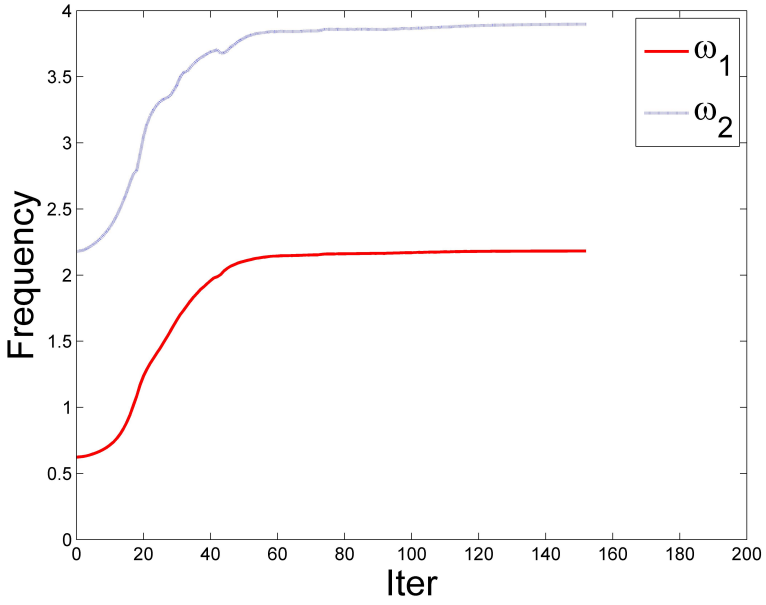

Figure 2.11: Optimization history for cantilever beam

can be neglected for this problem. However, as it has been mentioned before, there exists a trial solution for the case shown in Fig. 2.12.

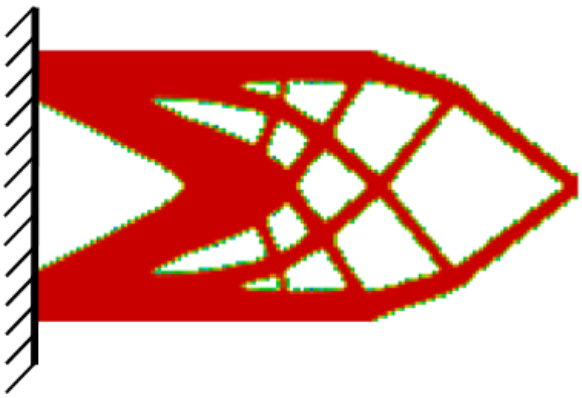

Figure 2.12: Optimized result for cantilever beam with concentrated mass ($\omega_1 = 0.5365 rad/s$, $\rho^k_{min} = 0$ and $\rho^m_{min} = 0$)

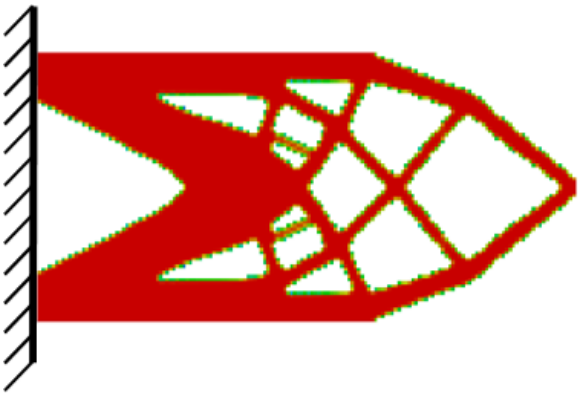

Figure 2.13: Optimized result for cantilever beam with concentrated mass ($\omega_1 = 0.5360 rad/s$, $\rho^k_{min} = 0.001$ and $\rho^m_{min} = 0.001$)

Another popular problem is the reinforcement problem where the beam has prescribed frame layout and the optimization target is to enhance its dynamic behavior.

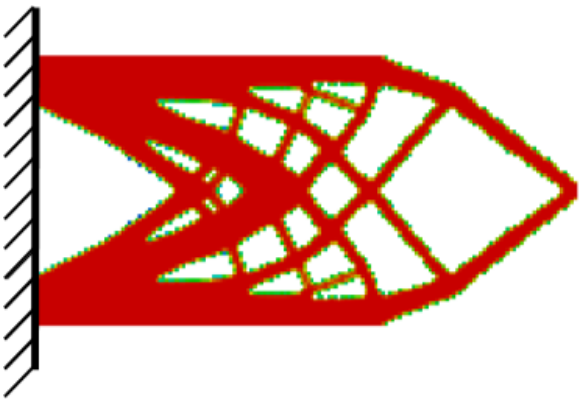

Figure 2.14: Optimized result for cantilever beam with concentrated mass ($\omega_1 = 0.5306 rad/s$, $\rho^k_{min} = 0.0001$ and $\rho^m_{min} = 0.1$)

In the third example, we investigated the same cantilever beam as shown in the second example, but it has six prescribed layers of solid elements in the top, right and bottom sides in Fig. 2.15. The optimized result is shown in Fig. 2.16 and the first two vibration modes are plotted in Fig. 2.17 and Fig. 2.18.

Figure 2.15: Design domain of a cantilever beam with prescribed elements

Figure 2.16: Optimized result of cantilever beam with prescribed elements

Figure 2.17: First vibration mode

Figure 2.18: Second vibration mode

2.5 Application in Phononic Band Gap Structures

2.5.1 Introduction

In this section, we apply eigenvalue topology optimization technique to maximize band-gap in phononic structures. There has been a recent surge of research effort towards achieving exotic dynamic response through novel microstructural design of periodic composites. Within mechanics and elastodynamics these responses can be categorized in two broad areas: phononics and metamaterials. Phononics is the study of stress wave propagation in periodic elastic composites. The phononic band-structure (Martinezsala et al. (1995)) results from the periodic modulation of stress waves, and as such has deep similarities with areas like electronic band theory (Bloch (1928)) and photonics (Ho et al. (1990)). These periodic modulations provide for very rich wave-physics and the potential for novel applications such as wave guiding (Khelif et al., 2003), ultrasound tunneling(Yang et al., 2002), acoustic rectification(Li et al., 2011), sound focusing (Yang et al., 2004), thermal property tuning (Cleland et al., 2001; Landry et al., 2008; Zen et al., 2014) and novel wave refraction applications (Cervera et al., 2001; Nemat-Nasser, 2015a,b; Sukhovich et al., 2008). The definitive characteristic of a phononic crystal which distiguishes it from a homogeneous or randomly heterogeneous media is the existence of a frequency re-

gion where wave propagation is prohibted. This region, called the phononic bandgap, directly or indirectly affects most of the proposed applications of phononic crystals. Therefore, it is of significant interest and impact to find out those phononic topologies for which the phononic bandgap is very large. This is a tough computational problem, especially in 3-D, which requires the use of fast phononic solvers coupled with sophisticated topology optimization routines.

There have been some recent applications of topology optimization on bandgap structures. For photonic crystals Cox and Dobson (Cox and Dobson, 2000; Dobson and Cox, 1999) applied topology optimization to maximize band gaps in two-dimensional photonic crystals for E and H polarization. Jensen and Sigmund (2004) presented results for optimized waveguide design. Recently, Men et al. (2014) has presented robust topology optimization results for the design of 3-D photonic crystals considering fabrication errors. In the area of phononics, Sigmund and Jensen (2003) first used a gradient based topology optimization method to systematically design both phononic band-gap materials and structures. Gazonas et al. (2006) and Bilal and Hussein (2011) implemented a genetic algorithm based TO method for the optimization of phononic bandgap structures. In addition, various structures and other materials exhibiting the band-gap phenomenon are also investigated by other researchers. For example, Jensen (2003) considered mass-spring structures, Diaz et al. (2005) designed band-gap grid structures, Halkjær et al. (2006) maximized band gaps in plated structures, Olhoff et al. (2012) and Halkjær and Sigmund (2004) optimized

band-gap beam structures. There also have been several recent advances in phononic topology optimization, for example, Vatanabe et al. (2014) maximized phononic band gaps in piezocomposite materials by means of topology optimization. Liu et al. (2016) explored the solid-solid phononic crystals for multiple separate band gaps with different polarizations.

Despite the considerable attention that topology optimization for 2-D phononic crystals has received, no work has been done for the optimization of 3-D crystals. This is despite the potentially more useful nature of optimized 3-D designs. Optimizing 2-D phononic crystals results in plate type designs which can have impacts on applications where wave propagation is constrained in 2-dimensions. However, wave propagation is inherently a 3-D phenomenon and optimization in 3-D can result in bulk materials with desirable and heretofor unachievable properties. This task is complicated by the challenging fact that phononic bandstructure evaluations are computationally expensive and that the computational complexity increases when band structure calculations are conducted repeatedly during the optimum searching process. The solution requires, first and foremost, an efficient phononic solver.

At this point there exist several numerical techniques for the evaluation of the phononic band structure. A good reference that discusses some of the most prominent techniques was published by Hussein (2009) where the authors also presented a method of accelerating the existing algorithms through a secondary expansion. The Plane Wave Expansion (Ho et al., 1990; Leung and Liu, 1990; Zhang and Sat-

pathy, 1990) method (PWE) and the Finite Element method (Hladky-Hennion and Decarpigny, 1991; Veres and Berer, 2012; White et al., 1989) are two of the most commonly used solvers owing to the ease of their implementation and their versatility. In this paper we have used a mixed variational method (Minagawa and Nemat-Nasser, 1976; Nemat-Nasser, 1972, 2015b; Nemat-Nasser et al., 1975; Srivastava and Nemat-Nasser, 2014) to calculate phononic bandstructures. The mixed variational method is derived from the Hu-Washizu (Hu, 1955; Washizu, 1955) variational theorem and it admits variations on both the stress and displacement fields. The mixed method has been known to converge faster than Rayleigh quotient which forms the basis of the traditional displacement based Finite Element method (Babuška and Osborn, 1978). In a recently published comprehensive study it has been shown that the mixed method also displays faster convergence than the PWE method (Lu and Srivastava, 2016). In addition to using the mixed variational method as our solver we have achieved further computational accelerations by implementing it over distributed Graphical Processing Units (Srivastava, 2015).

In this work we have considered three main varieties of the cubic phononic crystal lattice (FCC, BCC, and SC). Our aim is to find the 3-D topologies in a 2-material phononic crystal system that produce large all-angle, all-mode, normalized bandgaps for each of the three symmetries considered. We evaluate the phononic band structures along the Irreducible Brillouin Zones (IBZ) (Brillouin, 2003; Setyawan and Curtarolo, 2010) of the respective unit cells. The calculations are distributed over four

compute nodes of a CPU-GPU hybrid cluster. We use a SIMP based topology optimization routine which is coupled with Heaviside projection for the control of minimum feature sizes. The sensitivity analyses required for TO are again calculated in parallel through GPU computations. We present the first ever topology optimization results for 3-D phononic crystals and also the largest normalized bandgaps ever reported in 3-D.

2.5.2 Phononic Band Structure Calculation

2.5.2.1 Mixed variation formulation

In the following calculations, the elastodynamic eigenvalue problem is formulated using the mixed variation method (Lu and Srivastava, 2016; Minagawa and Nemat-Nasser, 1976; Nemat-Nasser, 1972; Nemat-Nasser et al., 1975; Srivastava and Nemat-Nasser, 2014). The propagation of waves in a three dimensional elastic medium is governed by

$$\sigma_{mn,n} = -\lambda \rho u_m, \tag{2.57}$$

$$u_{(j,k)} = D_{jkmn}\sigma_{mn}, \tag{2.58}$$

where $\lambda = \omega^2$, σ and u are the space and time dependent stress tensor and displacement vector respectively, ρ is the mass density and D is the compliance tensor. The Latin indices vary from 1 to 3 and subject to the summation conventions unless otherwise indicated. By varying independently on the stress and displacement field and

enforcing Bloch periodic boundary conditions, Eqs. (2.57) and (2.58) render to the following functional stationary,

$$\lambda_{u\sigma} = \frac{\langle \sigma_{mn}, u_{m,n} \rangle + \langle u_{j,k}, \sigma_{jk} \rangle - \langle D_{jkmn}\sigma_{mn}, \sigma_{jk} \rangle}{\langle \rho u_m, u_m \rangle}, \tag{2.59}$$

and the minimum of the above quotient is the solutions to the phononic eigenvalue problem. This minimization problem can be solved by expanding the displacement and stress fields to satisfy the Bloch periodic boundary conditions,

$$\bar{\sigma}_{jk} = \sum_{\alpha,\beta,\gamma} S_{jk}^{\alpha,\beta,\gamma} f^{\alpha,\beta,\gamma}(\mathbf{x}) \tag{2.60}$$

$$\bar{u}_j = \sum_{\alpha,\beta,\gamma} U_{j}^{\alpha,\beta,\gamma} f^{\alpha,\beta,\gamma}(\mathbf{x}). \tag{2.61}$$

The test functions should satisfy orthogonality in the sense that the Hermitian inner product $\left\langle f^{\alpha,\beta,\gamma}, f^{\theta,\eta,\xi} \right\rangle$ is proportional to $\delta_{\alpha\theta}\delta_{\beta\eta}\delta_{\gamma\xi}$, δ being the Kronecker delta. There are two ways of choosing test function: one of them is to set the coefficient $U_j^{\alpha,\beta,\gamma}$ and $S_{jk}^{\alpha,\beta,\gamma}$ to satisfy Bloch boundary condition and then the test function can employ arbitrary basis such as Lagrange basis functions (Lu and Srivastava, 2016) and cubic splines (Goffaux and Sánchez-Dehesa, 2003); the other is to let the test functions satisfy Bloch boundary condition

$$f^{\alpha\beta\gamma}(\mathbf{x} + \mathbf{h}^k) = f^{\alpha\beta\gamma}(\mathbf{x}) \exp\left[\mathrm{i}(\mathbf{k} \cdot \mathbf{h}^k)\right], \tag{2.62}$$

where $\mathbf{h}^k$ is the primary lattice vector on k^{th} direction for the phononic calculations and $\mathbf{k} = Q_i \mathbf{q}^i$ is the wave vector expressed in the reciprocal coordinates $\mathbf{q}^i$. The wave vector is mainly used to describe the patter of the displacement field. Since

only the unit cell, the smallest repetitive unit is analyzed, some assumptions have to be imposed to the pattern of the solution of the unit cell. For details, the reader should refer to (Sigmund and Jensen, 2003). For example, if the base cell is Y and wave vector is 0, then the solution mode will be $Y-$ periodic. Theoretically, all wave vector should be searched and analyzed to compute the frequency band, but due to the periodicity we may restrict the wave vector to the first Brillouin zone. Due to the symmetry of the base cell, the area can be restricted further to the triangular pyramid defined by the lines $R-\Gamma$, $\Gamma-M$,$M-X$ and $X-R$ shown in Fig. (2.21)

In this study, we use the trigonometric terms to expand the stress and displacement

$$f^{\alpha\beta\gamma}(\mathbf{x}) = \exp\left[\mathrm{i}2\pi Q_k^{\alpha\beta\gamma} x_k\right]. \tag{2.63}$$

The test functions immediately satisfy the Bloch boundary conditions. By substituting Eqs. (2.60) and (2.61) into the mixed variation formulation Eq. (2.59) and setting the derivative of $\lambda_{u\sigma}$ with respect to the unknown displacement and stress coefficients equal to zero, we obtain the following homogeneous equations

$$\langle \bar{\sigma}_{mn,n} + \lambda_{u\sigma}\rho\bar{u}_m, f^{\theta\eta\xi}\rangle = 0, \tag{2.64}$$

$$\langle D_{jkmn}\bar{\sigma}_{mn} - \bar{u}_{(j,k)}, f^{\theta\eta\xi}\rangle = 0. \tag{2.65}$$

The matrix form of the above equations can be written as

$$\mathbf{HS} + \lambda_{u\sigma}\mathbf{\Omega U} = 0, \tag{2.66}$$

$$\mathbf{\Phi S} + \mathbf{H}^*\mathbf{U} = 0, \tag{2.67}$$

where (*) indicates the complex conjugate operation of the matrix, and the expressions for the matrices are

$$[\mathbf{H}] = \mathrm{i}2\pi Q_k^{\theta\eta\xi} \int_\Omega \exp\left[\mathrm{i}2\pi(Q_l^{\alpha\beta\gamma} - Q_l^{\theta\eta\xi})x_l\right] d\Omega, \tag{2.68}$$

$$[\mathbf{\Omega}] = \int_\Omega \rho(x_1, x_2, x_3) \exp\left[\mathrm{i}2\pi(Q_l^{\alpha\beta\gamma} - Q_l^{\theta\eta\xi})x_l\right] d\Omega, \tag{2.69}$$

$$[\mathbf{\Phi}] = \int_\Omega D_{jkmn}(x_1, x_2, x_3) \exp\left[\mathrm{i}2\pi(Q_l^{\alpha\beta\gamma} - Q_l^{\theta\eta\xi})x_l\right] d\Omega. \tag{2.70}$$

The eigenvalues can be solved in this general matrix form

$$\mathbf{H}\mathbf{\Phi}^{-1}\mathbf{H}^*\mathbf{U} = \lambda_{u\sigma}\mathbf{\Omega}\mathbf{U}. \tag{2.71}$$

If M trigonometric expansion terms are used, i.e. α, β, γ vary from $-M$ to M independently and consider the symmetry of the stress tensor, the size of the eigenvalue problem Eq. (2.71) will be $3(2M+1)^3 \times 3(2M+1)^3$. When the unit cell consists of materials whose mass density and compliance are not constant over the entire domain, the mixed variation result will be neither upper bound or lower bound of the eigenvalue solution (Nemat-Nasser et al., 1975). Babuska and Osborn(Babuška and Osborn, 1978) has shown that for a unit cell with piecewise constant material properties, the mixed variation method lead to a convergence rate of $M^{-2+\epsilon}$. Therefore, the mixed variation method can rapidly converge to very accurate solutions.

2.5.2.2 GPU computations

In order to calculate the entire band structure of a unit cell the matrices have to be assembled and the eigenvalues have to be calculated at multiple wave-vector points

along the edge of the IBZ. This results in considerable computational complexity. However, since the assembly and eigenvalue solving processes are independent of each other they can be executed in parallel if the formulation is properly recast. The most basic computational unit in the formulation is the following integral in (Eq. (2.68)):

$$I_{\alpha\beta\gamma\theta\eta\xi} = \int_{\Omega} f d\Omega = \int_{\Omega} \exp\left[\mathrm{i}2\pi(Q_l^{\alpha\beta\gamma} - Q_l^{\theta\eta\xi})x_l\right] d\Omega = \sum_{i=1}^{N} f_i(\alpha,\beta,\gamma,\theta,\eta,\xi)v_i, \tag{2.72}$$

where f_i is the evaluation of the integrand at the centroid of the i^{th} element, v_i is the element volume and N is the number of elements which discretizes the unit cell. $Q_l^{\alpha\beta\gamma}$ are viewed as vectors of size $(2M+1)^3$, then the combination of $(Q_l^{\alpha\beta\gamma} - Q_l^{\theta\eta\xi})x_l$ will result in a matrix of size $(2M+1)^3 \times (2M+1)^3$ and the integral (Eq. (2.72)) can be rewritten as

$$I_{jk} = \sum_{i=1}^{N} f_{ijk} v_i, \tag{2.73}$$

where $j, k = 1, 2, \cdots, (2 * M + 1)^2$. To compute the above matrix of integrals using Graphical Processing Units we need to pass the vectors, volumes and centroids from the CPU to the GPU. On the GPU, the computation kernals are executed by a grid of thread blocks, where each thread has a unique id which corresponds to a set of indices i, j, k. Since the actual computation on each thread is relatively simple and many threads are operating in parallel, the method shows significantly reduced computation times comparing to serial computations over a CPU. Furthermore, the eigenvalue computations along the IBZ can be distributed over multiple GPUs in a distributed GPU cluster. In this case each compute node will solve for a part of the

band structure simultaneously thus decreasing the computation time further.

2.5.2.3 Hardware and Computation efficiency

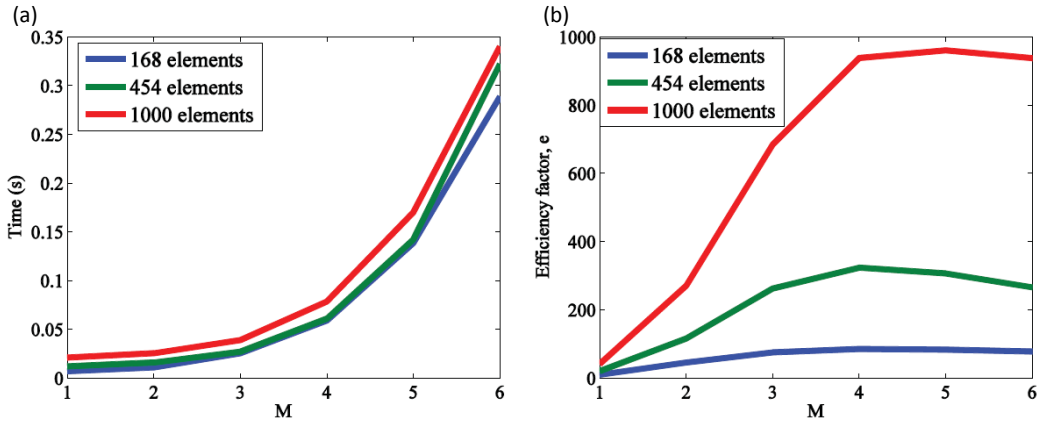

Figure 2.19: (a) GPU accelerated computation time for eigenfrequencies solved at one wavevector point. (b) Efficiency factor comparing the parallel formulation with the serial formulation (The analysis and comparison have been done by our collaborators)

The computation cluster used for this work consists of 4 compute nodes, each of which has 2 NVIDIA GTX-780 graphic cards and 2 Intel(R) Xeon(R) E5-2630 v2 CPUs installed to form the mixed CPU/GPU architecture. Each GPU has 2304 CUDA cores and each CPU has 6 cores. In order to determine the parallel computation efficiency, we define an efficiency factor (Srivastava, 2015) which measures the performance improvement through the parallel computations over serial computations in terms of the time it takes to do the same problem through the two methods:

$$e = \frac{t_{serial}}{t_{parallel}} \tag{2.74}$$

Fig. (2.19(a)) shows the time taken for solving eigenfrequences of a 2-D problem at one wave vector and the efficiency factors are plotted in Fig. (2.19(b)). As the number of field variable increases, the computation is 1000 times faster than the straightforward loop implementation. For a 2-D case, when M=2, the matrix size is 50×50 and the parallel computation time is about 0.03s when using 1000 elements. When using M=2 in a 3-D case, the matrix size will be 375×375, and the actual computation will be 118.5 times more complex, due to the complexity of eigenvalue problem is of $O(N^{2.37})$, where N is the size of the matrix. Therefore, each eigenvalue problem takes about 3.55s to solve and it takes less than 40s to compute 80 eigenvalue problems in parallel on 8 GPUs to complete the entire band structure.

2.5.3 Topology Optimization Formulation

In topology optimization of periodic composite materials, the goal is to optimize the distribution of two (or more) base material phases across the unit cell, which for finite element-based approaches, reduces to determining whether each element is to contain base material 1 or material 2. This fundamentally is a binary (or integer) programming problem of extremely high dimension, motivating relaxation of the binary condition and representation of each element's material properties as a continuous combination of the two base materials. In order to obtain a binary design, penalization methods such as the Solid Isotropic Material with Penalization (SIMP) method are used to make mixtures of the two materials at a location inefficient.

Interestingly, (Sigmund and Jensen, 2003) found that the use of penalization is not required in the design of band-gap structures as sharp contrasts in stiffness (Young's modulus) are desirable to produce large band-gaps. This allows use of a simple simple linear interpolation model for Young's modulus, given as

$$E_e(\rho_e) = \rho_e E^1 + (1 - \rho_e)\, E^2, \tag{2.75}$$

where E^1 and E^2 denote the Youngs modulus corresponding to the two base materials. We note this is equivalent to the SIMP interpolation for composites (Bendsøe and Sigmund, 1999) with exponent penalty term set to one.

The goal of the optimization is to maximize the gap between the j-th mode and j+1th mode, and thus we use the objective function given as

$$f(\rho_e) = 2\frac{\min_k \lambda_{j+1}(\mathbf{k}, \rho_e) - \max_k \lambda_j(\mathbf{k}, \rho_e)}{\min_k \lambda_{j+1}(\mathbf{k}, \rho_e) + \max_k \lambda_j(\mathbf{k}, \rho_e)} \tag{2.76}$$

and the resulting topology optimization formulation can be written as

$$\begin{aligned} &\max \;\; f(\rho_e) \\ &\text{s.t.} \;\; \left(\mathbf{H}\mathbf{\Phi}^{-1}\mathbf{H}^* - \lambda\mathbf{\Omega}\right)\mathbf{U} = 0 \\ &\qquad 0 \leq \rho_e \leq 1, \; e = 1, \cdots, N \end{aligned} \tag{2.77}$$

Note that we do not impose a volume constraint and allow the algorithm to freely distribute the two base materials, although it would straightforward to restrict the design problem in that manner.

The sensitivity of the natural frequencies (Sigmund and Jensen, 2003) can be calculated by differentiating Eq. (2.77) with respect to the design variables ρ_e, as

follows

$$\frac{\partial \lambda}{\partial \rho_e} = \boldsymbol{\psi}^* \left[-\boldsymbol{\Omega}^{-1} \frac{\partial \boldsymbol{\Omega}}{\partial \rho_e} \boldsymbol{\Omega}^{-1} \left(\mathbf{H} \boldsymbol{\Phi}^{-1} \mathbf{H}^* \right) - \boldsymbol{\Omega}^{-1} \left(\mathbf{H} \boldsymbol{\Phi}^{-1} \frac{\partial \boldsymbol{\Phi}}{\partial \rho_e} \boldsymbol{\Phi}^{-1} \mathbf{H}^* \right) \right] \boldsymbol{\theta} \tag{2.78}$$

We want to emphasize Eq. (2.77) generally indicates an asymmetric eigenvalue problem, as a result the eigenvalues and corresponding eigenvectors are complex numbers. The normalization conditions shown in Eq. (2.36)are used.

The sensitivity is calculated element-wise and therefore, substituting Eq. (2.73) into Eq. (2.69) and Eq. (2.70), the derivative of $\boldsymbol{\Omega}$ and $\boldsymbol{\Phi}$ with respect to the design variable of the i^{th} element, $\rho_{e(i)}$, can be calculated by

$$\frac{\partial [\boldsymbol{\Omega}]_{jk}}{\partial \rho_{e(i)}} = \left(\rho^1 - p^2 \right) f_{ijk} v_i, \tag{2.79}$$

$$\frac{\partial [\boldsymbol{\Phi}]_{jk}}{\partial \rho_{e(i)}} = \left(D^1_{jkmn} - D^2_{jkmn} \right) f_{ijk} v_i, \tag{2.80}$$

where no summation is implied. The sensitivity of the objective function in Eq. (2.77) can now be calculated by differentiating Eq. (2.76).

Finally we note that the Heaviside Projection Method (HPM) (Guest et al., 2004a) is used within these formulations to control the minimum length scale of designed features and create so-called single length scale microstructures (Sigmund, 1994). In particular, a reduced design variable field (Guest and Smith Genut, 2010) is adopted. For HPM, it essentially expresses continuum design ρ_e variables as a closed-form function of an independent design variable field, without any other changes to the above equations. For brevity, the details are omitted here; however, the reader is referred to Guest (Guest, 2009b; Guest et al., 2011b) for full algorithmic details.

Here, a continuation strategy is used on the Heaviside parameter, beginning at $\beta = 10$. The projection radius is 7.5% of the unit cell length. It should be noted that HPM is capable of controlling the minimum length scale of designed features and thus preventing solution mesh dependency, although such dependencies have not been observed for phononic band-gap materialsSigmund and Jensen (2003).

2.5.4 A Note on Normalized Band Gaps

The band structure is a plot of eigenfrequencies on different wave vectors and, therefore, the normalized band gap is calculated as the indicator of the relative size of the gap size by taking the ratio between the band gap width and the mid gap frequency. The simple way to control the normalized band gap sizes is to change the volume fraction of the inclusion. In the following cases, steel is used as the inclusion material and epoxy is used as the matrix material. The material properties are: $\rho_{steel} = 7780kg/m^3$, $E_{steel} = 207.1475GPa$, $\nu_{steel} = 0.2787$ and $\rho_{epoxy} = 1180kg/m^3$, $E_{epoxy} = 4.3438GPa$, $\nu_{epoxy} = 0.3679$. The 1-D phononic crystals are layered composites, shown in Fig. (2.20(a)). By changing the thickness of the stiff material phase, the maximal normalized band gap appears at volume fraction 0.729, where the band gap size is 1.408. Since the thickness is the only design variable in this 1-D case, this maximal gap size has to be the optimum. For the 2-D phononic crystal shown in Fig. (2.20(b)), the circular inclusions inside a 1×1 square unit cell is considered. We observe that when volume fraction is approximately 0.553 corresponding to 0.4196 in

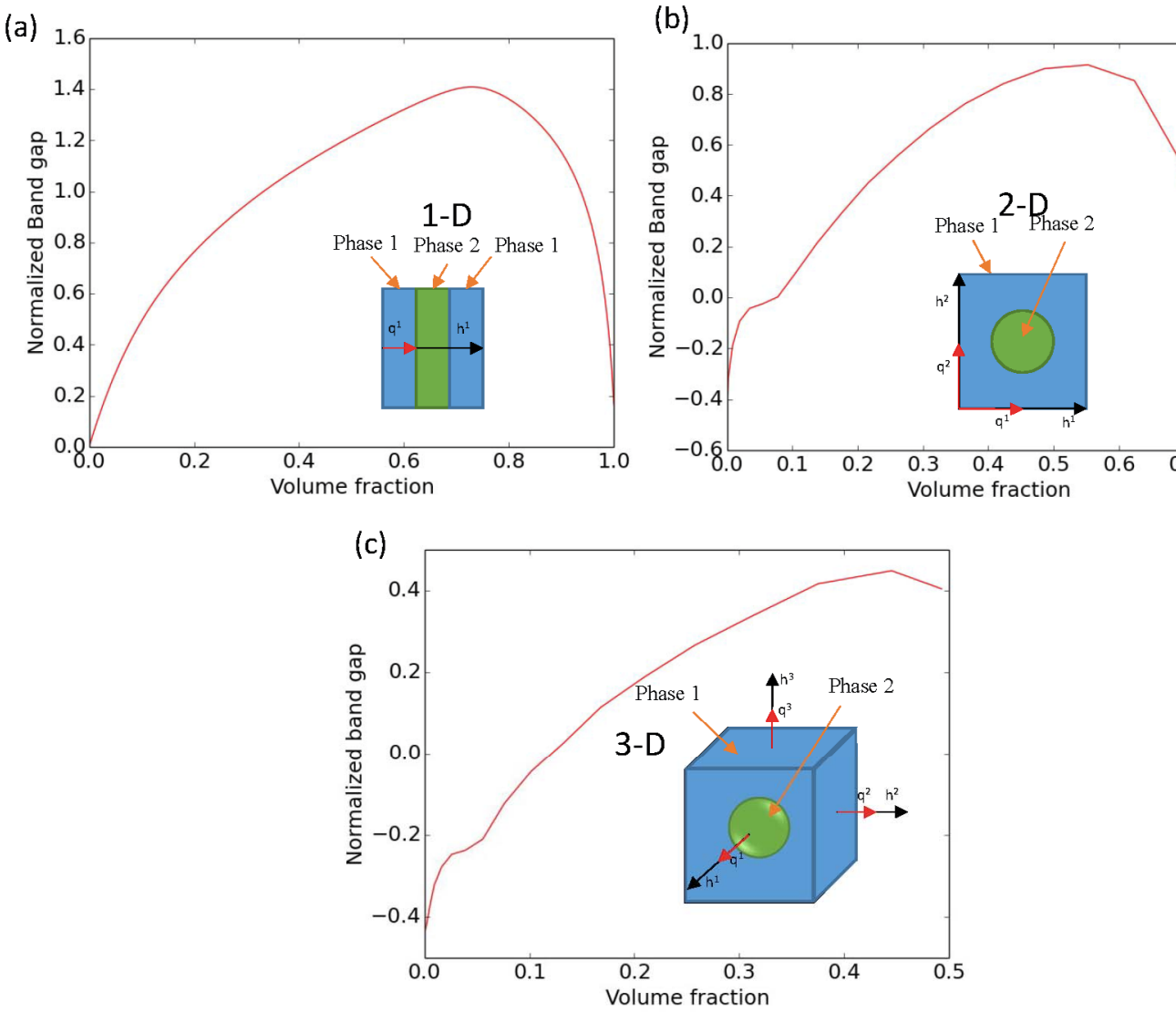

Figure 2.20: The relation between the normalized band gap and volume fraction of the stiff material phase. (a) 1-D 2-phase layered composite; (b) 2-D 2-phase composite with circular inclusion.

radius, we avchieve the largest normalized band gap of 0.915. This is smaller than the band gap reported by Bilal and HusseinBilal and Hussein (2011) where the midgap ratio is 1.113 and geometry of the inclusion is more complex. Fig. (2.20(c)) shows a 3-D case where the size of the cubic unit cell is $1 \times 1 \times 1$, the sphere inclusion leads to the maximum 0.448 normalized band gap at volume fraction of 0.445 corresponding to 0.4736 in radius. However, 3-D phononic crystal optimization has not yet been reported in literature and we believe that larger band gaps can be achieved by further increasing the volume fraction and improving the inclusion geometry. It can be seen from the three cases that in higher dimensions it is more difficult to obtain band gaps which are as large as the ones found in the lower dimensional cases.

2.5.5 Study of Cubic Unit cell

In this section the design domains are the cubic Bravais lattices. It should be emphasize that the phononic structures under consideration are synthetic materials and continuum mechanics is used to analyze the behavior. Therefore the cubic Bravais lattice here refers to different patterns for the synthetic composite material. The length of each unit cell edge is assumed to be 1cm, and it can be scaled but it cannot be too small that continuum mechanic approach is not accurately enough to predict the material behavior. There are three main varieties of the cubic Bravais lattices, which are simple cubic (SC), body-centered cubic (BCC) and face-centered cubic(FCC)(Hahn, 2005) lattice. The three lattices have their own variations based on

different space groups. For example, Maldovan et al. (2003) studied the photonic band gaps of 11 FCC structures. Although the rules of crystal symmetry are complex, there are simple ways to model the geometry which guarantee the basic crystal structures of the unit cells and the efficiency of computation. One of the most basic rules is that the material on each lattice point should have the same geometry and it can be realized by enforcing translational symmetry. As shown in Fig. (2.21(a),(b),(c)), the crystal structures can be replicated by translating the material along the edges of the SC lattice, the body diagonals of the BCC lattice and the face diagonals of the FCC lattice. Fig. (2.21(d),(e),(f)) shows that the same colored groups of elements are translational symmetric. Therefore, if an unconstrained SC, BCC or FCC is to be generated, the design domain should consist of the minimum number of element groups which include all the different colors. However, we implement the most time consuming sensitivity analyses on only a small portion of the total elements and then the sensitivity information is replicated by using other built-in symmetry of each unit cell, thereby also reducing the design domain. Specifically, the sensitivity analysis of SC is performed on $\frac{1}{8}$ of the unit cell and the complete sensitivity information is reconstructed by taking reflection symmetry of the block in Fig. (2.21(g)) against the orthogonal planes. For BCC, the sensitivity of $\frac{1}{16}$ of the unit cell is calculated and the first octant is reconstructed by rotating the small block 180° about y-axis and reflecting against x-z plane, then the elements in the first octant are copied by reflecting against x-z and y-z plane to create the upper half of the unit cell, and finally

taking the translation operation described in Fig. (2.21(e)). In order to construct the first octant of FCC in Fig. (2.21(i)), the small blue block which occupies $\frac{1}{32}$ of the unit cell is rotated 180° about y-axis to generate the small block above it and the two blocks are rotated together 180° about x-axis to complete the rest of the first octant. The first octant is then reflected against the y-z plane to obtain the second octant, and finally we take the translational operation in Fig. (2.21(f)) to complete the unit cell.

2.5.6 Results and Discussions

We use steel and epoxy to construct the $1cm^3$ cubic unit cell, and, for reasons described below, also report performance for tungsten carbide and epoxy systems where $\rho_{WC} = 13800kg/m^3$, $E_{WC} = 387.5559GPa$, $\nu_{WC} = 0.3459$. During each iteration the stress and displacement fields are expanded using 375 trigonometric terms ($M = 2$). After the optimum is obtained we used 2187 trigonometric terms ($M = 4$) to evaluate much more accurately the final band structure. The objective function of this study is the midgap ratio between the 6^{th} and 7^{th} band, where a complete band gap opens naturally for spherical inclusions. A homogeneous distribution of material was used as the initial guess for the BCC and FCC cases, while a spherical inclusion of radius $3.5mm$ was employed as the SC initial design (with an initial 15.4% midgap ratio). A homogenous distribution was also attempted for the SC case but the algorithm became stuck in a local minima, perhaps due to the fact that the SC design space is

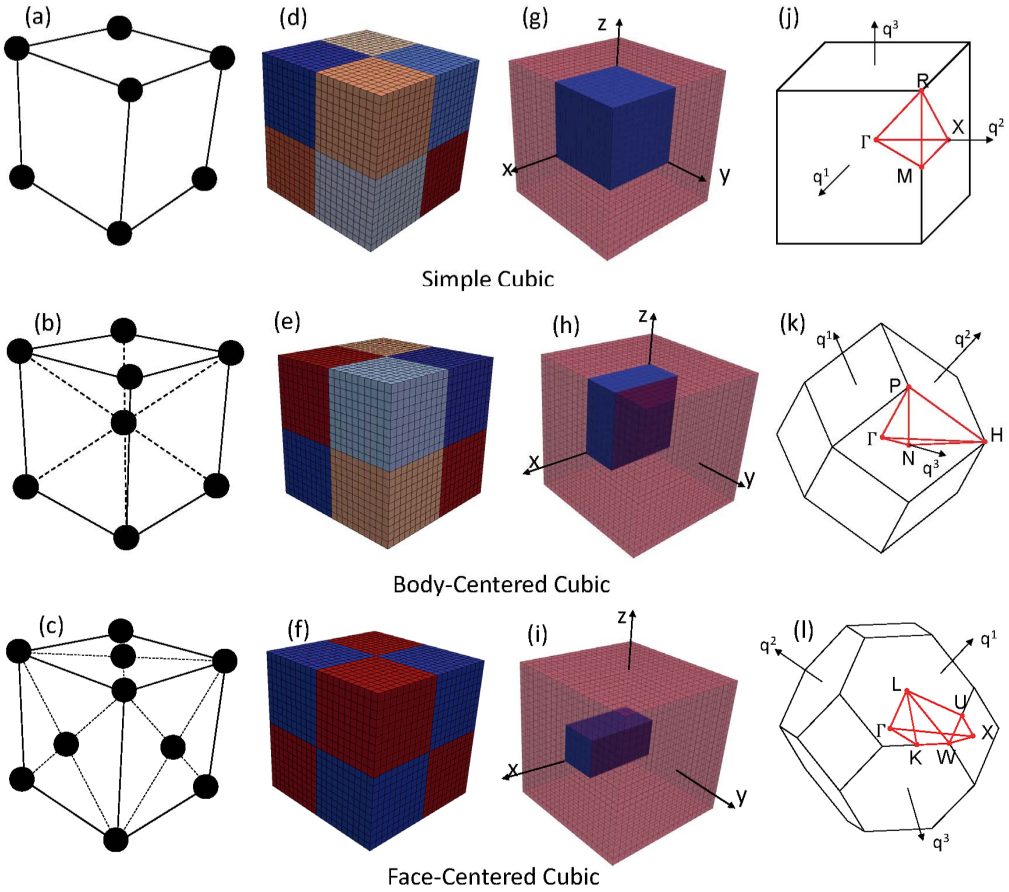

Figure 2.21: (a), (b), (c) are the schematics of the SC, BCC, FCC structure. (d), (e), (f) describe the translational symmetry corresponding to the cubic lattice on the left. Each color represents a group of elements, and if two cubic blocks of elements have the same color, these two blocks are translational symmetric. (g), (h), (i) show the design domains that are actually used in the sensitivity analyses. (j), (k), (l) are the Brillouin zones of the three cubic lattices. The red regions inside the Brillouin zones are the IBZs.

much larger than the BCC and FCC cases which have more strict geometric restrictions. This is not totally surprising, as topology optimization problems are nonconvex and global optimality can not typically be confirmed.

2.5.6.1 Simple Cubic Lattice

The SC lattice is discretized into $22 \times 22 \times 22$ cubic elements and the optimization is performed on $\frac{1}{8}$ of the total elements. Each iteration spends about 370 seconds on the band structure evaluation on 80 wave vectors, sensitivity analyses, data transfer and storage. After total 1247 iterations, we obtain the optimal results in Fig. (2.22(a),(b)). The result shows that the the structure has a band gap from 78.97kHz to 144.31kHz, which leads to a 58.5% midgap ratio. The corresponding volume fraction is 0.472.

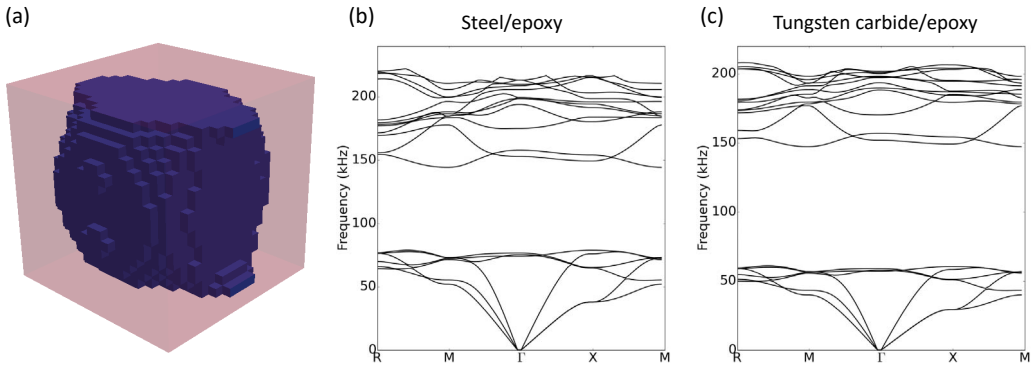

Figure 2.22: (a) the optimal SC unit cell on 22×22 mesh. Its band structure (b), (c) are calculated using steel/epoxy and tungsten carbide/epoxy, respectively.

2.5.6.2 Body-centered Cubic Lattice

The BCC lattice is discretized into $24 \times 24 \times 24$ cubic elements and $\frac{1}{16}$ of the total elements contribute as the design domain. Each iteration takes about 260 seconds and after total 1119 iterations, we obtain the optimal results as shown in Fig. (2.23(a),(b)). The optimal BCC structure has a band gap from 98.08kHz to 206.18kHz, which leads to a 71.06% frequency midgap ratio. The corresponding volume fraction is 0.465.

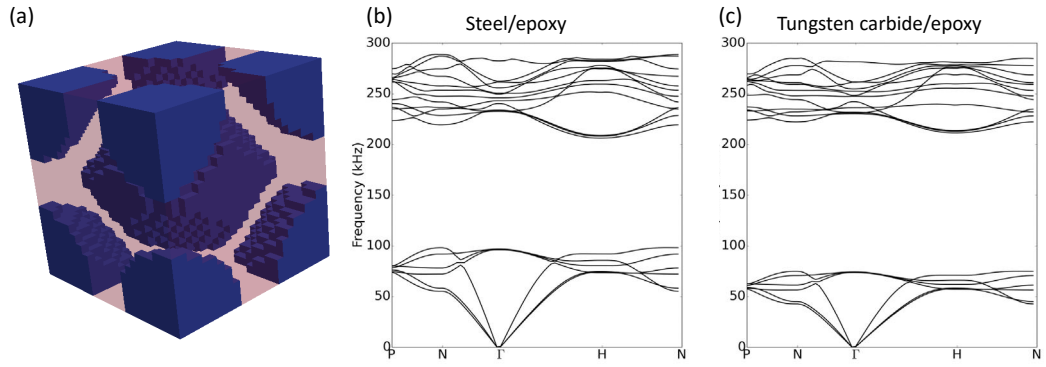

Figure 2.23: (a) is the optimal BCC unit cell. Its band structure (b), (c) are calculated using steel/epoxy and tungsten carbide/epoxy, respectively.

2.5.6.3 Face-centered Cubic Lattice

The FCC lattice is discretized into $24 \times 24 \times 24$ cubic elements and the design domain is $\frac{1}{32}$ of the total elements. We obtain the optimal results as shown in Fig. (2.24(a),(b)) through 580 iterations, where each iteration takes about 140 seconds. The result shows that the structure has a band gap from 126.30kHz to 270.0kHz,

which leads to a 72.5% frequency midgap ratio. The corresponding volume fraction is 0.498.

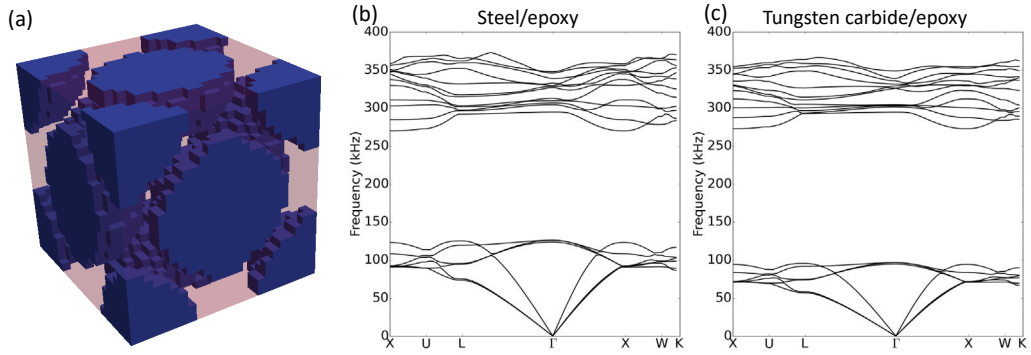

Figure 2.24: (a) is the optimal FCC unit cell and its band structure (b), (c) are calculated using steel/epoxy and tungsten carbide/epoxy, respectively.

We are interested in determining if the structures identified by the topology optimization algorithm do indeed offer improved performance over existing solutions reported in literature. (Page et al., 2005) reported that a hand-assembled close packed FCC lattice consisting of $0.8mm$-diameter tungsten carbide beads embedded in epoxy has the largest measured 3-D band gap. Its corresponding complete band gap appear between $1.5MHz$ and $3.9MHz$, which leads to a 88.9% midgap ratio. We show that by substituting tungsten carbide into the optimized inclusion structures, the band gaps are widened due to higher material contrast. In Fig. (2.22(c)), Fig. (2.23(c)) and Fig. (2.24(c)) it is clear that the tungsten carbide/epoxy unit cells narrows the first pass band and thus lead to larger band gap, where the midgap ratios for SC, BCC and FCC are 82.7%, 95.26% and 95.17% respectively. The BCC and FCC gaps

are bigger than the one that has ever reported and they have much smaller volume fraction than the reported closed packed FCC, which should be 0.74.

2.5.7 Comparison with Genetic Algorithm Result

Genetic algorithms (GA), a class of population-based stochastic search algorithms, have recently been successfully applied to optimize 2-D phononic crystals (Bilal and Hussein, 2011; Gazonas et al., 2006). Genetic algorithms perform a broad search of the design space which tends to reduce the influence of the initial guess, but rely on an extreme number of computations and tend to break down in large dimension spaces, such as high resolution 3D domains. Fig. (2.25(a)) shows a GA-optimized SC structure. In order to reduce the computation time, $\frac{1}{48}$ of total 11808 elements, close to the number of elements shown in Fig. (2.22(a)), are used as the design domain, which is in the shape of a tetrahedra. We have not been able to find a converged result for finer mesh. The resulting band gap is 55.3%, slightly narrower than the previous SC result. In Fig. (2.25(a)), it is clear that a more symmetric structure than the previously shown SC has been generated and the optimized structure shows several spikes stemming from the steel inclusion and reaching the faces of the unit cell. When the unit cell is assembled periodically based on the lattice structure, these spikes form one-node hinges which are known to introduce numerical errors. Therefore, it can be said that the GA produced a less realistic result with a smaller complete band gap compared to the previous SC case. Due to the symmetry limit of the mesh, it is not

feasible to optimize the BCC and FCC structure.

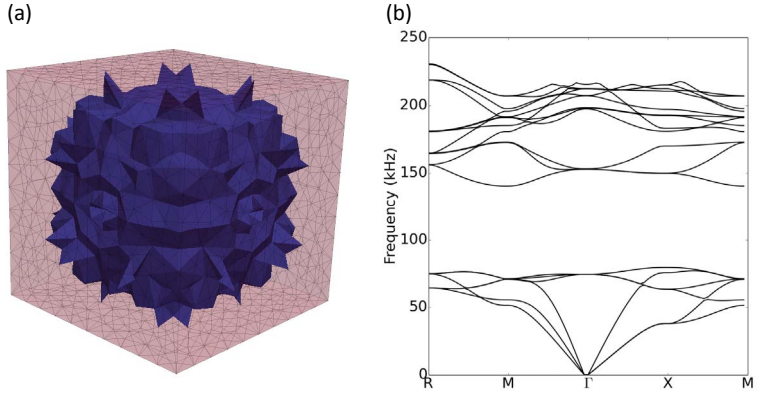

Figure 2.25: The band structure produced by steel/epoxy using genetic algorithm: (a) SC unit cell, (b) corresponding band structure.

2.5.8 Conclusions

We have presented optimized results of 3-D phononic crystals with ultra-wide band gaps. Topology optimization, enabled through GPU accelerated mixed variation method, provides an efficient optimization tool for 3-D cubic phononic crystals. The three cubic crystal lattices have been studied, where the translational symmetries are the primary rules of maintaining the basic crystal structures. The design domains are defined using the built-in symmetries of the lattice structures respectively such that the results can be generated with less computation effort. It is shown that the optimal results have very large band gaps and when material with high property contrast is substituted into the optimal geometry, larger than ever recorded band gaps are generated in BCC and FCC. The method presented in this paper provides larger

band gap and more realistic SC lattice than GA and exhibits significant versatility when perform optimization on different lattice structures.

2.5.9 Acknowledgements

This research has been conducted under UCSD/ONR W91CRB-10-1-0006 award to the Illinois Institute of Technology (DARPA AFOSR Grant RDECOM W91CRB-101-0006 to the University of California, San Diego) and NSF Grant1538367 to Johns Hopkins University.

2.6 Non-deterministic Eigenvalue Optimization

Although topology optimization is the most general form of structural optimization, solutions obtained by performing the optimization in a deterministic setting may be impractical or suboptimal when considering real-world engineering conditions with inherent variabilities including (for example) variabilities in fabrication processes and construction conditions. Such variabilites lead to uncertainties in structural geometry and/or material properties, which can result in potentially significant uncertainties in structural stiffness and mass when dynamic behavior is concerned. In the literature, several researchers have proposed robust topology optimization algorithms for considering uncertainty in applied loads (see e.g. Ben-Tal and Nemirovski (1997); Lógó (2007); Lógó et al. (2009)). Fewer works have considered topology optimization under

uncertainties in structural stiffness and mass. The structural responses, such as the displacements, are now an inverse of the random stiffness and mass matrices resulting from considering uncertainties. Sandgren and Cameron (2002) took a Monte Carlo approach, combining a genetic algorithm for optimizing truss topology and using randomly generated parameters to simulate the uncertainties in geometry and material properties. In Doltsinis and Kang (2004), the authors used the random field finite elements method of Liu et al. (1986) for modeling uncertainty in load, material properties, members cross sections (thicknesses) and nodal locations and performed sizing optimization for truss and truss-membrane structures. Guest and Igusa (2008) used second order perturbation and sought topologies with minimum "average" compliance under geometric uncertainties while Chen et al. (2010) employed KarhunenLoeve expansion along with a univariate dimension reduction technique to find optimal level set topologies in the presence of uncertainties in load and material properties.

In this work we follows the basic idea presented in (Asadpoure et al., 2011; Guest and Igusa, 2008) and use perturbation to quantify the effect of uncertainties on eigenvalues and eigenvectors and consequently sensitivity analysis. Physically speaking, when dynamic behavior is of concern, natural frequencies are represented by the eigenvalues and the vibration modes are describled by corresponding eigenvectors.

The details of perturbation method used for eigenvalue problems are shown in Section 2.3.1. The second order statistics of the eigenvalue λ can be computed from

those of the random fluctuation vector $\Delta\boldsymbol{\varepsilon}$ using Eq. (2.12)

$$\begin{aligned} E\left(\lambda_n(\boldsymbol{\varepsilon})\right) &= E\left(\lambda_n^0 + \sum_i \lambda_n^i \Delta\varepsilon_i + \frac{1}{2}\sum_i\sum_j \lambda_n^{ij}\Delta\varepsilon_i\Delta\varepsilon_j\right) \\ &= \lambda_n^0 + \frac{1}{2}\sum_i\sum_j \lambda_n^{ij}\sigma^{ij} \end{aligned} \tag{2.81}$$

$$\begin{aligned} Cov\left(\lambda_n(\boldsymbol{\varepsilon})\right) &= E\left(\lambda_n(\boldsymbol{\varepsilon}) - E\left(\lambda_n(\boldsymbol{\varepsilon})\right)^2\right) \\ &= \sum_i\sum_j \lambda_n^i\lambda_n^j\sigma^{ij} + \frac{1}{2}\sum_i\sum_j\sum_k (\lambda_n^i\lambda_n^{jk} + \lambda_n^{ij}\lambda_n^k)\sigma^{ijk} \\ &+ \frac{1}{4}\sum_i\sum_j\sum_k\sum_l \lambda_n^{ij}\lambda_n^{kl}(\sigma^{ijkl} - \sigma^{ij}\sigma^{kl}) \end{aligned} \tag{2.82}$$

where by $E(\cdot)$ we mean the operation of mathematical expectation and:

$$\sigma^{ij} = E\left(\Delta\varepsilon^i\Delta\varepsilon^j\right) \tag{2.83}$$

$$\sigma^{ijk} = E\left(\Delta\varepsilon^i\Delta\varepsilon^j\Delta\varepsilon^j\right) \tag{2.84}$$

$$\sigma^{ijkl} = E\left(\Delta\varepsilon^i\Delta\varepsilon^j\Delta\varepsilon^k\Delta\varepsilon^l\right) \tag{2.85}$$

It is seen that higher order statistical moments, σ^{ijk} and σ^{ijkl}, for the random vector $\Delta\boldsymbol{\varepsilon}$ do not appear in the second order estimate of the mean and are seen in the second order estimate of covariance matrix. These higher statistical properties are not usually available, however, ignoring them by truncating after the first term in the covariance expression provides satisfactory results in many practical cases (For detailed discussion, the reader is refered to Asadpoure et al. (2011)). In this work, these higher order terms are neglected.

Using the mean and covariance expressions shown in Eqs. (2.81) and (2.82), the robust eigenvalue topology optimization formulation can now be stated as follows:

$$
\begin{aligned}
&\max_{\beta,\rho_1,...,\rho_{Ne}} \quad \beta \\
&s.t. \quad (\boldsymbol{A} - \lambda_j \boldsymbol{B})\boldsymbol{x}_j = \boldsymbol{0}, \quad j = 1, ..., J, \\
&\qquad \boldsymbol{x}_j^T \boldsymbol{B} \boldsymbol{x}_k = \delta_{jk}, \quad j, k = 1, ..., J, \\
&\qquad \beta - \alpha_E E(\lambda_j) - \alpha_s \sqrt{Cov(\lambda_j)} \leq 0, \quad j = 1, ...J, \\
&\qquad \sum_{e=1}^{Ne} \rho_e v_e \leq V_{\max} \\
&\qquad 0 \leq \rho_e \leq 1 \qquad \forall e \in \Omega
\end{aligned}
\tag{2.86}
$$

where $\sqrt{Cov(\lambda_j)}$ is the standard deviation of compliance and the weighting coefficients α_E and α_S are real non-negative numbers.

To perform the sensitivity analysis, we full expend the inequality constraint as follows;

$$
Constraint = \beta - \alpha_E \left(\lambda_n^0 + \frac{1}{2} \sum_i \sum_j \lambda_n^{ij} \sigma^{ij} \right) - \alpha_s \left(\sum_i \sum_j \lambda_n^i \lambda_n^j \sigma^{ij} \right), \; n = 1, ...J, \tag{2.87}
$$

From Eq. (2.87), we can see that the sensitivity requires the computation of the first, second and third derivative of the eigenvalues. One simple way is to follow the ideas in Section 2.3.1. In this method, we need to first plug Eq. (2.24) into Eq. (2.87) to remove the second order derivative of eigenvalue, otherwise, the third derivative has

to be computed. However, this will inevitably require the sensitivity of the first and second order derivative of the eigenvectors, which can be computational expensive.

Alternatively, we can follow the idea discussed in Asadpoure et al. (2011) and use the adjoint method.

Chapter 3

Topology Optimization under Stochastic Dynamic Excitations

3.1 Introduction

In this chapter, topology optimization methods are developed and applied for structures subjected to random dynamic loads. Considering random dynamic loads is of great importance when the information of that is incomplete. In other words, the applied dynamic loads cannot be simply expressed by a deterministic function of time. In practice, a good example is seismic loads induced by earthquake ground motions. Housner (1947) first considered earthquake ground motion as a random stochastic process. After Housner's work, many researchers in earthquake engineering commu-

nity started to investigate earthquake ground motions by the use of stochastic process. Nowadays, most important structures and structures in earthquake prone areas are designed to be functional under seismic waves generated by stochastic analysis methods. Another example is that aircraft and aerospace vehicles are subjected to diverse sources of random dynamic excitation during their service life (Rong et al. (2000)). Such excitations include: (a) the ground loads induced during taxi, takeoff and landing of an aircraft, or during the transportation of a launch vehicle to the launch pad; (b) the gust excitation caused by atmospheric turbulence; (c) the aerodynamic excitation due to boundary layer turbulence and fluctuating wake forces; and (d) the excitation due to jet and rocket noise. Therefore, topology optimization algorithms for the above applications should be able to address the stochastic load.

The fundamental definition of one or more stochastic processes is in terms of the underlying probability distribution, as given by probability density functions or cumulative distribution functions. However, in many cases, such as the problems in this chapter, we can gain the information that we need for stochastic processes from considering their moments. Generally speaking, statistical properties of most stochastic loads are time dependent. However, stationarity assumption is often used to simplify the stochastic analysis and this simplification will give acceptable results for some real engineering problems. The property of stationarity of a stochastic process $X(t)$ is referred to some aspect of the description of the process being unchanged by any arbitrary shift along the t axis. Here the assumption that all statistical prop-

erties, such as the mean and second moment, are stationary is adopted which can significantly reduce the computation effort which in turn provides a possibility for the computational intense topology optimization methods to optimize stochastic dynamic problems. Furthermore, due to this stationary assumption, we also assume the stochastic process under investigation is a zero mean problem for convenience since we can always shift the non-zero problems by adding or subtracting a constant.

For a zero mean stationary problem, the key statistical property is the autocorrelation function, and it is states as

$$R_{XX}(\tau) = R_{XX}(t_2 - t_1) = E[X(t_1)X(t_2)] \tag{3.1}$$

In most cases, it has been found that it is easier to describe a stochastic process by another quantity, autospectral density function $S_{XX}(\omega)$, which contains the same information as the corresponding autocorrelation function R_{XX}. $S_{XX}(\omega)$ and $R_{XX}(\tau)$ are closely related by Fourier transform,

$$R_{XX}(\tau) = \int_{-\infty}^{+\infty} S_{XX}(\omega) e^{i\omega\tau} d\omega \tag{3.2}$$

$$S_{XX}(\omega) = \frac{1}{2\pi} \int_{-\infty}^{+\infty} R_{XX}(\tau) e^{-i\omega\tau} d\tau \tag{3.3}$$

The variance of the covariant stationary process can be found by setting $\tau = 0$, giving

$$\sigma_X^2 = R_{XX}(0) = \int_{-\infty}^{+\infty} S_{XX}(\omega) e^{i\omega\tau} d\omega \tag{3.4}$$

In the above integral, when S_{XX} has a constant value S_0, it can be seen the integration can be solved relatively easily and this case is commonly referred to as white noise,

by analogy with white light, which supposedly contains equal contributions from all relevant frequency components.

Given the characterization of the stochastic process, $X(t)$, described above, we aim to minimize the response variance by propagating a given input stochastic process through the structural system to be optimized.

In the literature, only few researchers have applied topology optimization to mitigate stochastic dynamic response and nearly all of these have considered the white noise excitation. For example, Rong et al. (2000) used the Evolutionary Structural Optimization (ESO) method to optimize continuum structures considering white noise stochastic dynamic loads in the frequency domain. Pagnacco et al. (2012) investigated the ESO of structures subject to white noise stochastic loads with respect to multiaxial fatigue criteria also in frequency domain. Lin et al. (2011) designed piezoelectric energy harvesting devices subjected to broadband random vibrations by applying topology optimization method. Qiao et al. (2012) considered both static loads and white noise stochastic loads for the layout optimization of multi-component structures. Rong et al. (2013) developed Sequential Quadratic Programming method for the topology optimization of structures under random white noise excitation.

Until recently, topology optimization for non-white noise random excitation had not been considered. In this chapter, we propose a new topology optimization algorithm to minimize the dynamic response of continuum structures subjected to filtered white noise excitation. The augmented state space formulation (Taflanidis

and Scruggs (2010)) is used for both the structural and filter systems. The problem is then solved in the frequency domain and a closed-form integration result for the response variance is obtained according to Igusa (1992). Note that, given its formulation in state space, non-classical damping can be considered in the proposed algorithm. In the optimization algorithm, the SIMP method is used to drive to a 0 $\sim$ 1 design. To circumvent the numerical problems associated with continuum problems and control the minimum length scale, we utilize the Heaviside Project Method (HPM) (Guest et al. (2004b)). Sensitivity analysis is performed analytically and the derivatives of real and complex eigenvalues and eigenvectors are given. The gradient-based optimizer Method of Moving Asymptotes (MMA) (Svanberg (1987)) is used as the optimizer. Several numerical examples are given to demonstrate the capabilities of the proposed algorithm.

3.2 Stochastic Dynamic Analysis

In this section, the stochastic dynamic analysis methods are discussed. We assume that the information about the structural system is complete and therefore the mass, stiffness, and damping can be treated as deterministic parameters. Uncertainty is present only in the externally applied dynamic loads.

First the problem is formulated by the popular second order matrix differential equation, then the solution methods are discussed and its pros and cons are commented. Second, alternatively we state the problem by using first order differential

equations, the state space method. Solution methods are also discussed in detail. Comparison of these two formulations are presented and their advantages and limitations are given.

3.2.1 Standard Formulation

First of all, the discretized equation of motion for the N degree of freedom continuum system is written in the popular second order matrix form as

$$\boldsymbol{M}\ddot{\boldsymbol{u}}_s(t) + \boldsymbol{C}\dot{\boldsymbol{u}}_s(t) + \boldsymbol{K}\boldsymbol{u}_s(t) = \boldsymbol{f}(t) \tag{3.5}$$

where $\boldsymbol{M}$, $\boldsymbol{C}$, $\boldsymbol{K}$ are the N by N mass, damping and stiffness matrices respectively. Since $\boldsymbol{f}(t)$, which without loss of generality is a zero mean stationary stochastic process, denotes the vector random force process, the resulting displacement vector $\boldsymbol{u}_s(t)$ is also a vector stationary random process. In addition, in practice it is almost always impossible to obtain the exact probability distribution function of $\boldsymbol{f}(t)$ with respect to time t, so second-order moments (which are often available) are instead used to quantify the input stochastic process. In particular, the stochastic excitation $\boldsymbol{f}(t)$ is characterized by its autocorrelation function $\boldsymbol{R}_{ff}(\tau)$, or equivalently the autospectral density function $\boldsymbol{S}_{ff}(\omega)$ in the frequency domain.

Given the characterization of the stochastic process excitation, $\boldsymbol{f}(t)$, described above, we aim to determine the properties of a given scalar response process given by

$$z(t) = \boldsymbol{l}^T\boldsymbol{u}_s(t) \tag{3.6}$$

where $\boldsymbol{l}$ is a location indicator vector that can be modified to consider response at different locations on the structure, the superscript T denotes transpose, and $\boldsymbol{u}_s(t)$ denotes the vector of displacements for each degree of freedom. The stochastic analysis can also be conveniently performed in frequency domain. The input and output autospectral density functions can be related in frequency domain by the following equation,

$$S_{zz}(\omega) = \boldsymbol{l}^T \boldsymbol{H}(\omega) \boldsymbol{S}_{ff}(\omega) \boldsymbol{H}(\omega)^* \boldsymbol{l} \tag{3.7}$$

where superscript * denotes conjugate transpose operation and $\boldsymbol{H}(\omega)$ is the harmonic transfer function, or frequency response function, that can be determined from modal analysis as:

$$\boldsymbol{H}(\omega) = \boldsymbol{\Phi}(\boldsymbol{\Lambda} - \omega^2 \boldsymbol{I} + i\omega \overline{\boldsymbol{C}}) \boldsymbol{\Phi}^T \tag{3.8}$$

where,

$$(\boldsymbol{K} - \lambda_n \boldsymbol{M}) \boldsymbol{\phi}_n = \boldsymbol{0} \tag{3.9}$$

$$\boldsymbol{\phi}_i^T \boldsymbol{M} \boldsymbol{\phi}_j = \delta_{ij} \tag{3.10}$$

in which $\boldsymbol{I}$ is the identity matrix, $\boldsymbol{\Lambda}$ is a diagonal matrix of the eigenvalues λ_i and $\boldsymbol{\Phi}$ is a matrix of the eigenvectors $\boldsymbol{\phi}_i$ for modes $n = 1, ..., m \leq N$, δ_{ij} is the Kronecker delta function, and $\overline{\boldsymbol{C}}$ is the modal damping matrix equal to $\boldsymbol{\Phi}^T \boldsymbol{C} \boldsymbol{\Phi}$. When Raleigh damping is used, all terms in the parenthesis in Eq.3.8 are diagonal matrices. Having

computed $S_{zz}(\omega)$, the response variance is computed as:

$$\sigma_{zz}^2 = R_{zz}(0) = \int_{-\infty}^{+\infty} S_{zz}(\omega)d\omega = 2\int_{0}^{+\infty} S_{zz}(\omega)d\omega \tag{3.11}$$

When the stochastic excitation is represented by a white noise process, then $\boldsymbol{S}_{ff}(\omega)$ is a constant quantity and does not depend on ω. Mathematically, this is convenient because Eq.3.7 simplifies such that the response spectral density depends only on the frequency response function - thus it is dependent on the structure alone - and analytical solutions can be derived from Eq.3.11(Clough and Penzien (1995), Lutes (1997)). White noise excitation is a specific type of excitation that is convenient but not often realistic. For non-white noise excitation Eq.3.11 must be solved numerically in general. What's more, given the large scale of the problems of interest here (hundreds of thousands of degrees of freedom, or more) and the fact that Eq.3.11 must be solved a large number of times at each iteration of the optimization, this rapidly becomes intractable given present computational constraints.

In this chapter we will consider the earthquake stochastic ground motion, which is characterized by a filtered white noise model, called the Kanai-Tajimi model. Physically, filtered white noise can be interpreted as passing a white noise process through a linear system (filter) with frequency response function tuned to produce a response with the desired power spectral density. The Kanai-Tajimi model has the following form

$$S_{aa}^{KT}(\omega) = S_0 \frac{\omega_g^4 + (2\zeta_g\omega_g\omega)^2}{(\omega_g^2 - \omega^2)^2 + (2\zeta_g\omega_g\omega)^2} \tag{3.12}$$

$$S_0 = \frac{\sigma_0^2}{\pi\omega_g(2\zeta_g + \frac{1}{2\zeta_g})^2} \tag{3.13}$$

Where ω_g, ζ_g, S_0, σ_0 are the natural circular frequency and damping ratio of the filter (in this case the ground), the intensity of the input white noise excitation and the variance of the excitation respectively.

3.2.2 State Space Formulation

To alleviate the computational expense associated with solving Eq.3.11. Eq.3.5 is modified to make use of the augmented state space formulation based on the filtered white noise model (Taflanidis and Scruggs (2010)).

$$\dot{\boldsymbol{x}}(t) = \boldsymbol{A}\boldsymbol{x}(t) + \boldsymbol{e}w(t) \tag{3.14}$$

$$z(t) = \tilde{\boldsymbol{l}}^T\boldsymbol{x}(t) \tag{3.15}$$

where $\boldsymbol{x}(t)$ is the state vector (corresponding to augmentation of the original structural system states - displacement and velocities - together with ancillary states related to the filtered white noise system), $w(t)$ is white noise input with spectral intensity scalar equal to S_0, $\tilde{\boldsymbol{l}}$ is the new location indicator that extracts the displacement component under investigation, $\boldsymbol{A}$ and $\boldsymbol{e}$ are the state-space matrix and vector.

Next, we derive the expressions for the parameters in the above augmented state space formulation. When ground excitation is considered the right hand side of Eq.3.5 is $\boldsymbol{f}(t) = -\boldsymbol{M}\boldsymbol{\tau}a_g(t)$. Where $\tau = \lfloor 0\,1\,\ldots\ldots\,0\,1 \rfloor$ for y-direction ground motion for

2d problems, is the influence vector ((Clough and Penzien, 1995)) and $a_g(t)$ represents the ground acceleration. For the filter system, it can be modeled by a single degree of freedom system as

$$\ddot{u}_g(t) + 2\zeta_g\omega_g\dot{u}_g(t) + \omega_g^2 u_g(t) = -w(t) \tag{3.16}$$

The output power spectral density function by passing $w(t)$ with S_0 through the single degree of freedom system in Eq.3.16 will be equal to the Kanai-Tajimi power spectral density function.

The state space representation of the structural system, described by the first order differential equation, is shown as follows,

$$\dot{\boldsymbol{x}}_s(t) = \boldsymbol{A}_s\boldsymbol{x}_s(t) + \boldsymbol{q}_s(t) \tag{3.17}$$

$$z(t) = \tilde{\boldsymbol{l}}^T\boldsymbol{x}_s(t) \tag{3.18}$$

where $\boldsymbol{x}_s \in R^{2N}$ is the state vector composed with displacements and velocities of the structural system. $\tilde{\boldsymbol{l}}_s$ is the location indicator and it extracts the target displacement from $\boldsymbol{x}_s$. The matrix $\boldsymbol{A}_s$ and vector $\boldsymbol{q}_s(t)$ are

$$\boldsymbol{A}_s = \begin{bmatrix} \boldsymbol{0}_{N\times N} & \boldsymbol{I}_{N\times N} \\ -\boldsymbol{M}^{-1}\boldsymbol{K} & -\boldsymbol{M}^{-1}\boldsymbol{C} \end{bmatrix} \quad \boldsymbol{q}_s(t) = \boldsymbol{M}^{-1}\begin{Bmatrix} \boldsymbol{0}_N \\ \boldsymbol{f}(t) \end{Bmatrix} \tag{3.19}$$

In particular, when ground excitation is considered, we have

$$\boldsymbol{q}_s(t) = \boldsymbol{e}_s a_g(t) \tag{3.20}$$

The vector $\boldsymbol{e}_s$ can be found according to the following expression

$$\boldsymbol{e}_s = \left\{ \begin{array}{c} \mathbf{0}_N \\ \\ -\boldsymbol{\tau} \end{array} \right\} \tag{3.21}$$

For the filter system, the state space representation is

$$\dot{\boldsymbol{x}}_f(t) = \boldsymbol{A}_f \boldsymbol{x}_f(t) + \boldsymbol{e}_f w(t) \tag{3.22}$$

$$a_g(t) = \boldsymbol{c}_f^T \boldsymbol{x}_f(t) \tag{3.23}$$

where $\dot{\boldsymbol{x}}_f(t) \in R^2$ is the state vector composed with displacements and velocities of the filter system. The matrix and vectors are

$$\boldsymbol{A}_f = \left[\begin{array}{cc} 0 & 1 \\ \\ -\omega_g^2 & -2\zeta_g\omega_g \end{array} \right] \quad \boldsymbol{e}_f = \left\{ \begin{array}{c} 0 \\ \\ -1 \end{array} \right\} \quad \boldsymbol{c}_f = \left\{ \begin{array}{c} -\omega_g^2 \\ \\ -2\zeta_g\omega_g \end{array} \right\} \tag{3.24}$$

Combining Eq.3.18 and Eq.3.23 leads to the representation of the form Eqs. (12) and (13) with the following definitions (Taflanidis and Scruggs (2010)),

$$\boldsymbol{x}(t) = \left[\begin{array}{c} \boldsymbol{x}_s(t) \\ \\ \boldsymbol{x}_f(t) \end{array} \right] \quad \boldsymbol{A} = \left[\begin{array}{cc} \boldsymbol{A}_s & \boldsymbol{e}_s\boldsymbol{c}_f^T \\ \\ \mathbf{0}_{2\times 2N} & \boldsymbol{A}_f \end{array} \right] = \left[\begin{array}{cc} \boldsymbol{A}_s & \boldsymbol{B} \\ \\ \mathbf{0}_{2\times 2N} & \boldsymbol{A}_f \end{array} \right] \quad \tilde{\boldsymbol{l}} = \left[\begin{array}{c} \tilde{\boldsymbol{l}}_s \\ \\ \mathbf{0}_{2\times 1} \end{array} \right] \tag{3.25}$$

After obtained the above parameters, we can solve Eq.3.15 for the covariance matrice of $\boldsymbol{x}(t)$ and $z(t)$. It is noted that the covariance matrix of $x(t)$ can be computed from the Lyapunov matrix equation (Khot et al. (1988), Taflanidis and Scruggs (2010) and Curadelli and Amani (2014)) for a zero-mean stationary white noise random process. Since we are dealing with large continuum topology optimization problems,

solving the Lyapunov equation - which requires vectorization and Kronecker products techniques - presents major computational challenges. The computational complexity of this approach is $O(n^6)$.

Having reformulated the problem in the augmented state space, we can solve the system in the frequency domain. In this formulation, the frequency response function (related to Eq.3.15) has the form

$$\boldsymbol{H}(\omega) = (-\boldsymbol{A} + i\omega\boldsymbol{I})^{-1} \tag{3.26}$$

The matrix inverse operation in Eq.3.26 requires substantial computational cost, so we will use eigen decomposition to attenuate it. The eigenvalue problem of unsymmetric real matrix $\boldsymbol{A}$ involves two basic equations, the right and left eigenvalue problems as stated below,

$$(\boldsymbol{A} - \mu_i\boldsymbol{I})\boldsymbol{\theta}_i = \boldsymbol{0} \tag{3.27}$$

$$\boldsymbol{\psi}_i^*(\boldsymbol{A} - \mu_i\boldsymbol{I}) = \boldsymbol{0} \tag{3.28}$$

$$\boldsymbol{\theta}_i^*\boldsymbol{\theta}_j = \delta_{ij} \tag{3.29}$$

$$\boldsymbol{\psi}_i^*\boldsymbol{\theta}_j = \delta_{ij} \tag{3.30}$$

where where μ_i, θ_i, ψ_i are the i-th complex eigenvalue, right and left eigenvectors, respectively, for modes $i = 1, \ldots, 2m \leq 2N + 2$. The size of eigenvalue problems is much larger and equals $2N + 2$. Making use of Eqs.3.30, Eq.3.30 can be further simplified to

$$\boldsymbol{H}(\omega) = \boldsymbol{\Theta}(-\boldsymbol{\mu} + i\omega\boldsymbol{I})^{-1}\boldsymbol{\Psi}^* \tag{3.31}$$

where $\boldsymbol{\mu}$ is a diagonal matrix and it stores the first $2m$ eigenvalues, the columns of $\boldsymbol{\Theta}$ and $\boldsymbol{\Psi}$ contains the corresponding right and left eigenvectors. In Eq.3.31, we can see all terms in the parenthesis are indeed diagonal. The variance of the response can be calculated (similar to Eq.3.11) as:

$$\sigma_{zz}^2 = R_{zz}(0) = 2\int_0^{+\infty} S_{zz}(\omega)d\omega = 2S_0\tilde{\boldsymbol{l}}^T(\int_0^{+\infty} \boldsymbol{H}(\omega)S_{ee}\boldsymbol{H}(\omega)^* d\omega)\tilde{\boldsymbol{l}} \tag{3.32}$$

in which S_{ee} is a matrix of size $2N+2$ by $2N+2$ and $S_{ee_{ij}} = 0$, except that $S_{ee_{2N+2,2N+2}} = 1$ except that. Although higher dimension, the integral in Eq.3.32 can be solved analytically using the method developed by Igusa (1992). It uses Stieltjes transform and the result is given below,

$$\gamma_{ij} = \int_0^{+\infty} (-\mu_i + i\omega)(-\mu_j - i\omega)d\omega = \frac{-i}{\mu_i + \mu_j}\ln(\frac{-\mu_i}{\mu_j}) - \frac{2\pi}{\mu_i + \mu_j} \tag{3.33}$$

$$\gamma_{ji} = \frac{i}{\mu_i + \mu_j}\ln(\frac{-\mu_i}{\mu_j}) \tag{3.34}$$

Thus no numerical integration scheme needs to be carried out, and it has been found that the use of the above analytical result makes the algorithm very efficient. Another advantage of this method is that it is capable of taking non-classical damping into consideration, this by-product is of great interest for damping optimization. For classically damped systems, the large complex eigenvalue problems (Eqs.3.30) need not be solved in practice. Actually, the real and complex eigenvalues and eigenvectors shown in Eqs.3.10 and Eqs.3.30 are closely related and is discussed next. Therefore the computational cost from solving the eigenvalue problem is not substantially increased compared to other methods when investigating classically damped problems.

Due to the fact that the proposed augmented state space formulation is very general and capable of dealing with non-classical damping, the computational effort to treat non-classical damping is substantially increased compared to the classical damping case, and especially the use of complex eigenvalues and eigenvectors may further increase the complexity of the analysis. However, it has been found that when the damping is classical, there is no need to perform additional eigenvalue analysis for the augmented system.

Once the real eigenvalue problem is solved, we have λ_n, $\boldsymbol{\phi_n}$, natural circular frequency $\omega_n = \sqrt{\lambda_n}$ and the damping ratio ζ_n for $n = 1, \ldots, N$. Then the corresponding complex eigenvalues and eigenvectors of the structural system for $n = 1, \ldots, 2N$, can be computed as follows(Igusa (1992))

$$\boldsymbol{\mu} = \begin{cases} \mu_{2n-1} & = \omega_n(-\zeta_n - i\sqrt{1-\zeta_n^2}) \quad if \quad n = odd \\ \mu_{2n} & = \omega_n(-\zeta_n + i\sqrt{1-\zeta_n^2}) \quad if \quad n = even \end{cases} \tag{3.35}$$

$$\boldsymbol{\theta}^s_{2n-1} = \begin{Bmatrix} \boldsymbol{\phi}_n \\ \mu_{2n-1}\boldsymbol{\phi}_n \end{Bmatrix} \quad if \quad n = odd \tag{3.36}$$

$$\boldsymbol{\theta}^s_{2n} = \begin{Bmatrix} \boldsymbol{\phi}_n \\ \mu_{2n}\boldsymbol{\phi}_n \end{Bmatrix} \quad if \quad n = even \tag{3.37}$$

$$\boldsymbol{\psi}_{2n-1}^{s} = \beta_{2n-1} \left\{ \begin{array}{c} -(\mu_{2n-1}^{-1})^{*} \boldsymbol{K} \boldsymbol{\phi}_{n}^{s} \\ \\ \boldsymbol{M} \boldsymbol{\phi}_{n}^{s} \end{array} \right\} \quad if \quad n = odd \tag{3.38}$$

$$\boldsymbol{\psi}_{2n}^{s} = \beta_{2n} \left\{ \begin{array}{c} -(\mu_{2n}^{-1})^{*} \boldsymbol{K} \boldsymbol{\phi}_{n}^{s} \\ \\ \boldsymbol{M} \boldsymbol{\phi}_{n}^{s} \end{array} \right\} \quad if \quad n = even \tag{3.39}$$

$$\boldsymbol{\beta} = \left\{ \begin{array}{lll} \beta_{2n-1} & = (-(\mu_{2n-1}^{-1})^{*} \omega_{n}^{2} + \mu_{2n-1}^{*})^{-1} & if \quad n = odd \\ \beta_{2n} & = (-(\mu_{2n}^{-1})^{*} \omega_{n}^{2} + \mu_{2n}^{*})^{-1} & if \quad n = even \end{array} \right. \tag{3.40}$$

The normalizations of eigenvectors are shown as follows,

$$(\boldsymbol{\theta}_{n}^{s})^{*} \boldsymbol{\theta}_{l}^{s} = \delta_{nl} \tag{3.41}$$

$$(\boldsymbol{\psi}_{n}^{s})^{*} \boldsymbol{\psi}_{l}^{s} = \delta_{nl} \tag{3.42}$$

The eigenvalues and eigenvectors of the filtered system can be computed similarly (Igusa (1992)). Regarding the whole system, the eigen-pairs can be combined and only the first few of them are used in the stochastic analysis.

Thus, we simply have

$$\mu_{n} = \mu_{n}^{s} \tag{3.43}$$

$$\boldsymbol{\theta}_{n} = \left\{ \begin{array}{c} \boldsymbol{\theta}_{n}^{s} \\ \\ \mathbf{0}_{2\times 1} \end{array} \right\} \tag{3.44}$$

$$\boldsymbol{\psi}_{n} = \left\{ \begin{array}{c} \boldsymbol{\psi}_{n}^{s} \\ \\ -\left(\left[\boldsymbol{A}_{f}^{*} - (\mu_{n}^{s})^{*} \boldsymbol{I} \right]^{-1} \right) \boldsymbol{B}^{*} \boldsymbol{\psi}_{n}^{s} \end{array} \right\} \tag{3.45}$$

3.3 Topology Optimization Formulation

The goal of topology optimization is to optimally distribute material within a design domain. In the design of continuum structures discretized by finite element method, this typically means to decide whether the elements exist or not. Although existence problems are discrete in nature, by introducing relationships between stiffness and the volumetric density of material ρ ranged from 0 to 1, we can relax this problem and drive them to binary solutions using the popular SIMP method (Bendsøe (1989); Zhou and Rozvany (1991)).

According to the SIMP method, the elemental stiffness is now expressed as

$$\boldsymbol{K}^e(\rho_e) = (\rho_e^p + \rho_{min}^k)\boldsymbol{K}_0^e \tag{3.46}$$

where $\boldsymbol{K}_0^e$ is the element stiffness for the unit design variable magnitude. The power p in Eqs.3.46, called the penalization power, is introduced with a view to yield distinctive "0-1" designes, and is normally gradually increased till a satisfactory "0-1" design is achieved. $\rho_{min}^k = 0.00001$ is the lower bound of the element density for the stiffness matrix. For dynamic problems, an additional power q is often added to the expression for the element mass matrix. The main reason to use that is to remove localized modes, or alternatively called spurious modes. For instance, when the fundamental frequency is maximized, the use of penalization factor p higher than 1 is more likely to generate fundamental vibration modes involving local void elements only. This vibration mode is numerically produced when SIMP is used and is not

realistic in practice. In this paper, the interpolation scheme used in Du and Olhoff (2007) is adopted and modified such that the mass matrix is expressed as,

$$\boldsymbol{M}^e(\rho_e) = \begin{cases} (\rho_e^q + \rho_{min}^m)\boldsymbol{M}_0^e & if \quad \rho_e > 0.1 \\ (c_0\rho_e^q + \rho_{min}^m)\boldsymbol{M}_0^e & if \quad \rho_e \leq 0.1 \end{cases} \tag{3.47}$$

By properly setting the value of c_0, C^0 continuity is guaranteed, but C^1 is not ensured. But, the difference is negligible as discussed in Du and Olhoff (2007). The value of q used in this work is equal to $p+1$. ρ_{min}^m is set to 0.01, a value much higher than ρ_{min}^k to provide a lower bond on the ratio of ρ_{min}^k and ρ_{min}^m, so that the trivial design with $\rho_e = 0$ everywhere is not optimal. The global stiffness and mass matrices are assembled according to the standard routine.

The topology optimization formulation can now be stated as follows,

$$\begin{aligned} \min \quad & \sigma_{zz}^2 = 2S_0\tilde{\boldsymbol{l}}^T \left(\int_0^{+\infty} \boldsymbol{H}(\omega)\boldsymbol{S}_{ee}\boldsymbol{H}(\omega)^* d\omega \right) \tilde{\boldsymbol{l}} \\ s.t. \quad & (\boldsymbol{A} - \mu_i^2 \boldsymbol{I})\boldsymbol{\theta}_i = \boldsymbol{0} \\ & \boldsymbol{\eta}_i^*(\boldsymbol{A} - \mu_i^2 \boldsymbol{I}) = \boldsymbol{0} \\ & \boldsymbol{\rho}_e^T \boldsymbol{v}_e \leq V_{\max} \\ & 0 \leq \rho_e \leq 1 \quad \forall e \in \Omega \end{aligned} \tag{3.48}$$

The Heaviside projection method (Guest et al. (2004b)) is used to avoid the well-known numerical instabilities of checkerboards and mesh dependency associated with continuum topology optimization, and it also can control the minimum length scale. This essentially expresses continuum design variables $\boldsymbol{\rho}_e$ as a closed-form function of

independent design variables used in Guest et al. (2004b). For brevity, the details are omitted here; however, the reader is refer to Guest et al. (2011b) for full algorithmic details. Here, a constant Heaviside parameter of $\beta = 25$ is used.

To compute the sensitivity, we first substitute Eq.3.31 to Eq.3.32, yielding the following form for the response variance,

$$\sigma_{zz}^2 = 2S_0 \tilde{\boldsymbol{l}}^T \boldsymbol{\Theta} \left(\int_0^{+\infty} (-\boldsymbol{\mu} + i\omega \boldsymbol{I})^{-1} \boldsymbol{\Psi}^*(\omega) \boldsymbol{S_{ee}} \boldsymbol{\Psi} (-\boldsymbol{\mu} - i\omega \boldsymbol{I})^{-1} d\omega \right) \boldsymbol{\Theta}^T \tilde{\boldsymbol{l}} \tag{3.49}$$

Applying the analytical integration result to Eq.3.49 gives the simplified expression,

$$\sigma_{zz}^2 = 2S_0 \tilde{\boldsymbol{l}}^T \boldsymbol{\Theta} (\boldsymbol{\Gamma} \cdot \boldsymbol{D}) \boldsymbol{\Theta}^T \tilde{\boldsymbol{l}} \tag{3.50}$$

where $\boldsymbol{D} = \boldsymbol{\Psi}^* \boldsymbol{S_{ee}} \boldsymbol{\Psi} = \hat{\boldsymbol{\psi}}^* \hat{\boldsymbol{\psi}}$, $\hat{\boldsymbol{\psi}}$ denotes the last row ($2N + 2$-th row) of $\boldsymbol{\Psi}$, and $\boldsymbol{\Gamma}$ is the matrix form of Eqs. 3.33 and 3.34.

Sensitivity analysis of the objective function is carried out by computing the derivative of the variance in Eq.3.50 as,

$$\frac{\partial \sigma_{zz}^2}{\partial \rho_e} = 2S_0 \tilde{\boldsymbol{l}}^T \left(\frac{\partial \boldsymbol{\Theta}}{\partial \rho_e} (\boldsymbol{\Gamma} \cdot \boldsymbol{D}) \boldsymbol{\Theta}^T + \boldsymbol{\Theta} \left(\frac{\partial \boldsymbol{\Gamma}}{\partial \rho_e} \cdot \boldsymbol{D} + \Gamma \cdot \frac{\partial \boldsymbol{D}}{\partial \rho_e} \right) \boldsymbol{\Theta}^T + \boldsymbol{\Theta} (\boldsymbol{\Gamma} \cdot \boldsymbol{D}) \frac{\partial \boldsymbol{\Theta}}{\partial \rho_e} \right) \tilde{\boldsymbol{l}} \tag{3.51}$$

where $\frac{\partial \boldsymbol{\Theta}}{\partial \rho_e}$ and $\frac{\partial \boldsymbol{D}}{\partial \rho_e}$ are the derivatives of the complex eigenvectors. The term $\frac{\partial \boldsymbol{\Gamma}}{\partial \rho_e}$ involves the derivative of the complex eigenvalues as,

$$\frac{\partial \gamma_{ij}}{\partial \rho_e} = \frac{\left(\frac{\partial \mu_i}{\partial \rho_e} + \frac{\partial \mu_j}{\partial \rho_e} \right)}{(\mu_i + \mu_j)^2} \left(i \ln(\frac{-\mu_i}{\mu_j}) + 2\pi \right) + \frac{i}{(\mu_i + \mu_j)} \left(\frac{\mu_j}{\mu_i} \right) \left(\frac{-\frac{\partial \mu_i}{\partial \rho_e} \mu_j + \mu_i \frac{\partial \mu_j}{\partial \rho_e}}{\mu_j^2} \right) \tag{3.52}$$

$$\frac{\partial \gamma_{ji}}{\partial \rho_e} = -\frac{\left(\frac{\partial \mu_i}{\partial \rho_e} + \frac{\partial \mu_j}{\partial \rho_e} \right)}{(\mu_i + \mu_j)^2} \left(i \ln(\frac{-\mu_i}{\mu_j}) \right) - \frac{i}{(\mu_i + \mu_j)} \left(\frac{\mu_j}{\mu_i} \right) \left(\frac{-\frac{\partial \mu_i}{\partial \rho_e} \mu_j + \mu_i \frac{\partial \mu_j}{\partial \rho_e}}{\mu_j^2} \right) \tag{3.53}$$

3.4 Numerical Examples

The topology optimization process outlined in previous sections is applied here to optimize continuum structures with stochastic support excitation. Specifically, given a stationary support excitation described by the filtered white noise model in Eqs. 3.12 and 3.13, we aim to minimize the variance of a translational displacement at a specific node subject to a volume constraint.

3.4.1 Cantilever Beam with Concentrated Mass on the Free End

Figure 3.1: Design domain of a cantilever beam with a concentrated mass

As a first example, we consider the case with a concentrated mass at the middle of the cross section on the free end of the cantilever beam shown in Fig.3.1. We aim to minimize the variance of the vertical displacement at the node where the concentrated mass is located. The rectangular design domain is 20m by 10m, and the thickness is 1m. The material is isotropic with Youngs modulus $E = 10000\text{N/m2}$,

Poissons ratio $\upsilon = 0.3$, and mass density $\rho_{mass} = 1\text{kg/m3}$. The concentrated mass is equal to 10% of the total mass when the entire domain is full of solids. The design domain is discretized by a rectangular mesh of 160 by 80, namely 12800 four-node plain stress continuum elements. The damping ratio and natural circular frequency of the filter system are $\zeta_g = 0.64$ and $\omega_g = 8\text{rad/s}$ respectively, and according to Eq.3.13 the corresponding the power spectral density of the filtered white noise process has $S_0 = 0.019\text{N}^2/\text{Hz}$. For the structural system, Rayleigh damping is considered and the first and fourth damping ratios are assumed fixed at 5% regardless how the topology changes. The total allowed volume is equal to 50% of the entire volume.

Referring to the analytical results from white noise support excitation (Clough and Penzien (1995) and Lutes (1997)), it is observed the contribution to the variance of each mode is proportional to the corresponding modal frequency raised to the -3 power. It is also observed that that high-frequency modes will generally contribute much less to the response that will low-frequency modes. Thus, optimization for white noise excitation is to some extent similar to maximizing the lowest natural frequency (e.g. maximizing stiffness). This solution provides a convenient and intuitive basis for comparison. In the following, we compare results from the proposed stochastic optimization algorithm with results produced by maximizing the fundamental natural frequency.

Fig.3.2a shows the optimized structure considering the prescribed filtered white noise support excitation, and Fig.3.2b shows the corresponding structure optimized

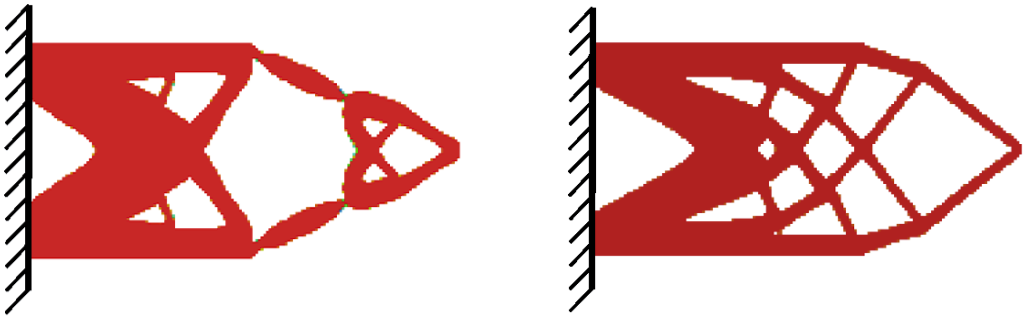

(a) $\sigma_{zz}^2 = 0.075m^2, \omega_1 = 1.74rad/s$ (b) $\sigma_{zz}^2 = 0.132m^2, \omega_1 = 2.22rad/s$

Figure 3.2: Comparison of optimized results between (a) stochastic excitation and (b) free vibration

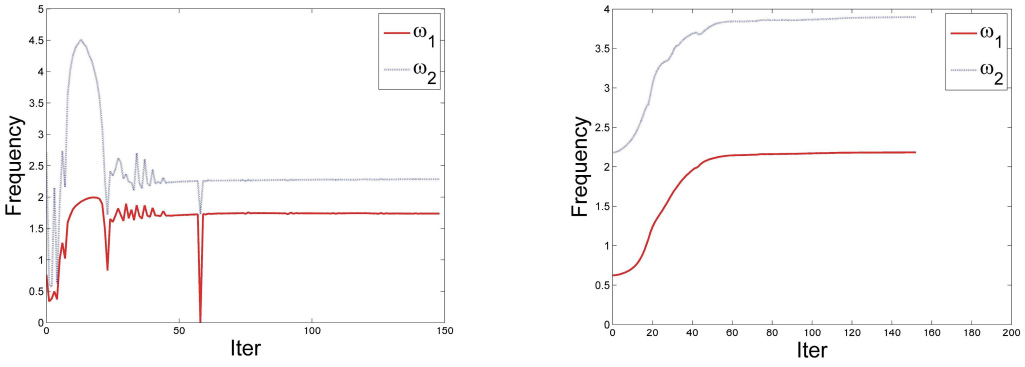

(a) (b)

Figure 3.3: Optimization history for (a) stochastic optimization and (b) free vibration

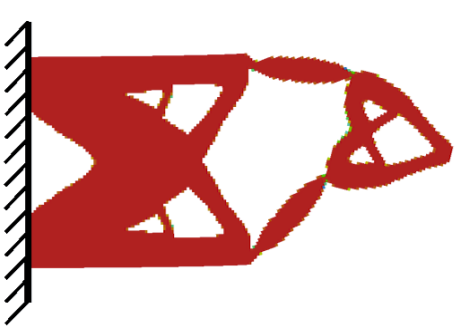

(a) First vibration mode for stochastic support excitation

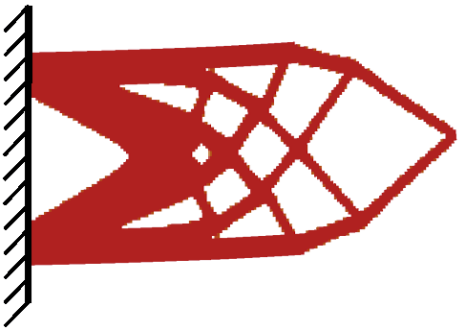

(b) First vibration mode for maximizing fundamental frequency

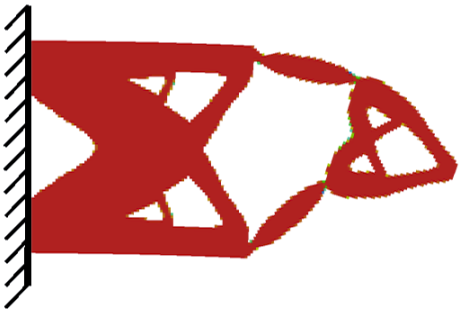

(c) Second vibration mode for stochastic support excitation

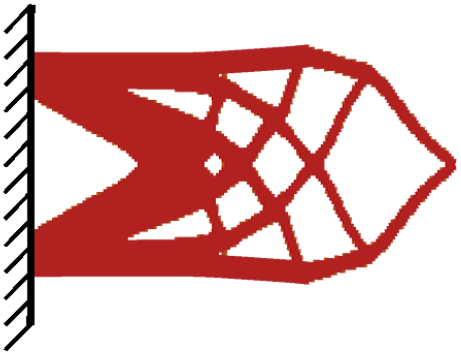

(d) Second vibration mode for maximizing fundamental frequency

Figure 3.4: Vibration modes: (a) and (b) first and second modes for stochastic optimization; (c) and (d) first and second modes for free vibration

to maximize the lowest natural frequency. Figures 3.3a and 3.3b plot the optimization history of the first two natural frequencies. It can be found that at the beginning of the optimization process, the frequencies are increasing monotonically in Figure 3.3a, which is in good agreement with Figure 3.3b. However, as the progress of the optimization iteration, both frequencies are decreasing until convergent criterion is satisfied. This basically tells us the optimal structure does not tend to be as stiff as possible where it is true for the case of maximizing fundamental frequency shown in Figure 3.3b.

In Figure 3.2a, we can observe four one-node hinges, which make this design relatively flexible. From the first vibration mode (Figure 3.4a), we can see the main structure is moving upward, while due to the local rotation of the one-node hinges, the right part tends to move downward, thus the vertical displacement is mitigated. In contrast, Figure 3.4b shows the entire cantilever beam is bending upward which produces a larger vertical displacement. From the second mode plotted in Figure 3.4c, it can be found that the local rotation of one-node hinges further amplifies the displacement. But since the contribution of first mode is much higher than that from second mode, we can say this amplification is not manifest in the total lateral displacement. Figure 3.4d indicates there is no lateral displacement for the case shown in Figure 3.2b. Although the solution shown in Figure 3.2a is not as stiff as that in Figure 3.2b, we can see that the variance is indeed much lower.

3.4.2 Cantilever Beam with Prescribed Solid Elements

Figure 3.5: Design domain of a cantilever beam with prescribed solid elements

In the second example, we consider the same structure with 6 layers of prescribed solid elements on the top, bottom, and free end, respectively. The variance of the same tip displacement is minimized considering the same volume constraint and support excitation as the first numerical example. Results are again compared with optimization to maximize the lowest natural frequency (i.e. maximum stiffness design). It has

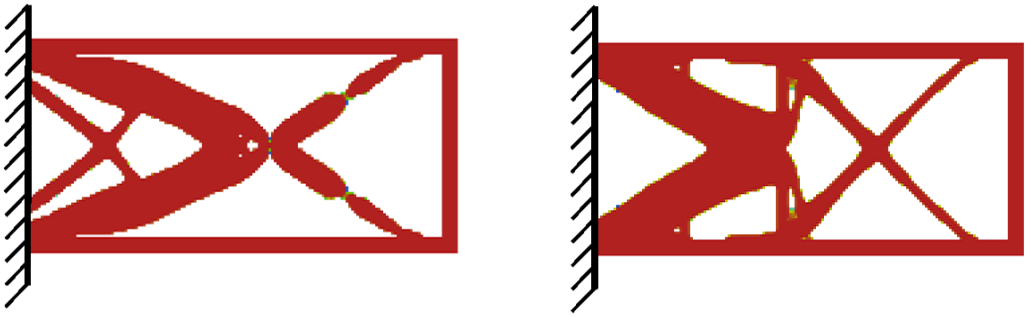

(a) $\sigma_{zz}^2 = 0.035m^2, \omega_1 = 1.56rad/s$ (b) $\sigma_{zz}^2 = 0.143m^2, \omega_1 = 2.45rad/s$

Figure 3.6: Comparison of optimized results between (a) stochastic excitation and (b) free vibration

been found that the natural frequencies of the two cases shown in Figure 3.6 are very close.

Next, the effect of number of modes considered in calculating the variance is investigated. The result is plotted in Figure 3.7. At the starting point, all cases give almost the same prediction on the variance, which implies only the first 2 modes in the augment state space formulation need to be considered when computing the objective function. Whereas, as the optimization progress, all cases deviate from each other due to the accuracy of their sensitivity analyses (Exact sensitivity is obtained if all modes are considered). It can be found that when the number of modes is larger than 10, the optimization process tends to converge.

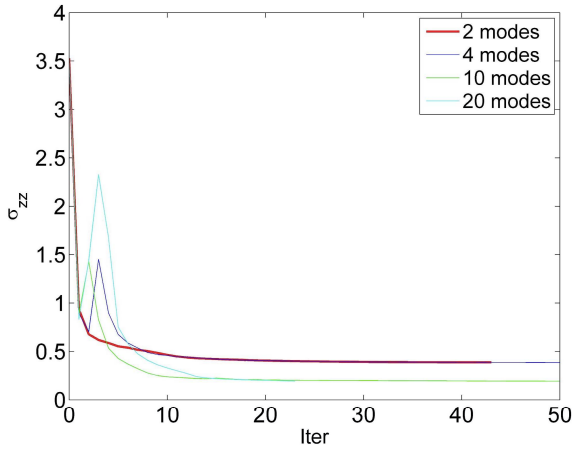

Figure 3.7: Effect of number of modes

3.4.3 Parametric Study on the Filter Design

In this section, we consider the effects of the filter parameters (filter frequency) and (filter damping) on the optimized response. First, we consider different values of ω_g while keeping ζ_g unchanged. In the design optimization, 10 modes were considered in all cases. The power spectral density is shown in Figure 3.8, and the optimization results are shown in Figure 3.9. It should be noted that the form of the optimized designs are independent of the excitation magnitude. Thus, while the excitation power spectra in Figure 3.8 have significantly different variance, it is the shape of the power spectrum that is important as the magnitude can be taken outside of the integral meaning it only has the effect of scaling the response variance and will not change the form of the response power spectrum. It is seen that for high ω_g , the

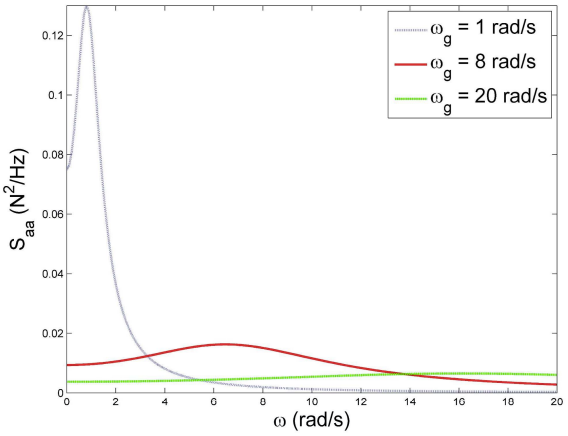

Figure 3.8: Plot of power spectral density for different ω_g

optimized structures look like similar. Whereas, for relatively low, e.g. $\omega_g = 1rad/s$, the optimization result tends to converge from the left side of the curve in Figure 3.8.

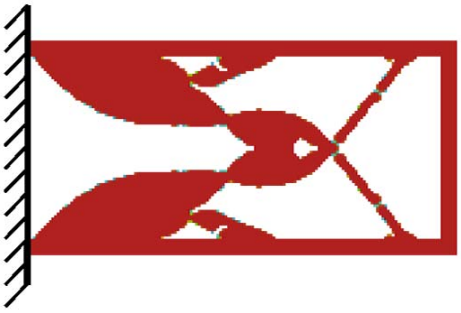

(a) Optimized structure for $\omega_g = 1$

($\omega_1 = 1.73 rad/s$)

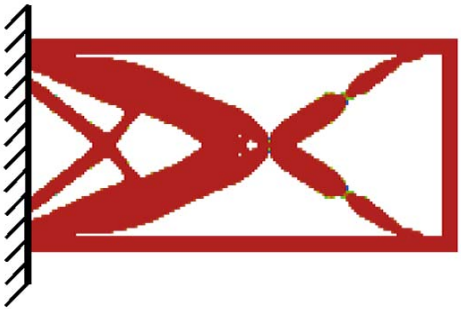

(b) Optimized structure for $\omega_g = 8$

($\omega_1 = 1.56 rad/s$)

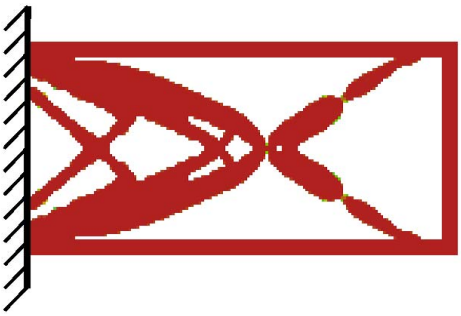

(c) Optimized structure for $\omega_g = 20$

($\omega_1 = 1.56 rad/s$)

Figure 3.9: Optimization results for $\omega_g = 1$, 8 and 20 rad/s

It is not able to climb the hill since for low , the slope of the curve near the peak is significantly sharp. If the fundamental frequency in the initial design is on the right side of the input power spectral density function, then it should look like Figure 3.9.

Then, we consider different values of ζ_g while keeping $\omega_g = 8rad/s$ unchanged. The power spectral density is shown in Figure 3.10, and the optimization results are shown in Figure 3.11. It is seen that for low ζ_g , the natural frequency of the

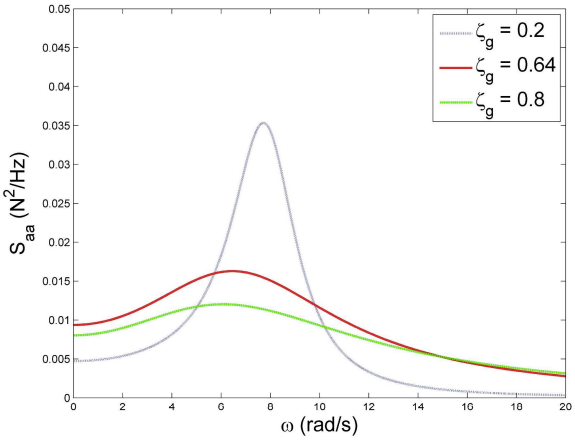

Figure 3.10: Plot of power spectral density for different ζ_g

optimized structures in Figure 3.11a is the lowest. For relatively large , the natural frequencies of the optimized structures shown in Figure 3.11 are very close, meaning large ζ_g has little effect on the optimal solution.

3.5 Conclusions

Topology optimization of continuum structures for the minimization of the variance of displacement under stochastic filtered white noise excitation is investigated

(a) Optimized structure for $\zeta_g = 0.2$

($\omega_1 = 1.86 rad/s$)

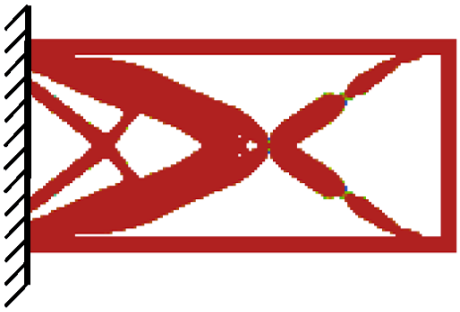

(b) Optimized structure for $\zeta_g = 0.64$ ($\omega_1 = 1.56 rad/s$)

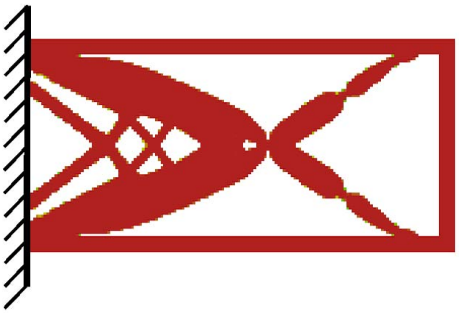

(c) Optimized structure for $\zeta_g = 0.8$

($\omega_1 = 1.68 rad/s$)

Figure 3.11: Optimization results for $\zeta_g = 0.1$, 0.64 and 0.80

in this paper. The paper derives a computationally efficient means of conducting the topology optimization that formulates the linear stochastic dynamics problem using the augmented state space and solves the system in the frequency domain taking advantage of useful analytical expressions for the response variance computation that save significant computational effort. The corresponding design sensitivities are derived and challenges associated with computing complex eigenvalues and the associated sensitivities are overcome. An additional benefit of the presented formulation is that it can optimize structures with non-classical damping. Two numerical examples are presented that explore the differences between designing a cantilever beam to mitigate stochastic dynamic effects and designing the same cantilever to maximize stiffness (as is commonly done). In these examples, we further study the effect of the number of eigenmodes used in the optimization and find that using 10-20 modes is sufficient in our example and, more importantly, that designs identified from using 10-20 modes differ significantly from those that utilize only 2-4 modes. This highlights that the optimizer is able to make use of higher mode contributions to mitigate vibrations. We also study the effects of the input excitation on the response and show that the optimizer will identify different solutions for different excitations catering the mode shapes of the optimal design to the frequency content of the excitation.

Chapter 4

Concluding Remarks and Future Research

This thesis presents eigenvalue topology optimization under deterministic conditions and also uncertainties. In the first part, a general eigenvalue topology optimization problem was introduced. Then we reviewed the sensitivity analysis method for real eigenvalues and eigenvectors and discussed numerical challenges and mitigation strategies. However, in order to compute the correct multiple eigenvalues sensitivity, more robust algorithms should be proposed to track the mode shapes.

Later in this part, we derived the sensitivities of complex eigenvalues and eigenvectors. Next, the proposed algorithm considering complex eigenvalue problems was applied to maximize phononic band-gap structures. Interesting results have been

found and the largest normalized all-angle all-mode band gaps reported in literature was revealed. At the end of this part, we have formulated the topology optimization formulation for non-deterministic eigenvalue optimization. Perturbation method was used to derive the topology optimization formulation. Sensitivity analysis was also performed.

In chapter 3, stochastic dynamic load is under consideration. In particular, earthquake ground motion was investigated. The problem was formulated in state space and solved in frequency domain. Filtered white noise autospectral density has been considered. However, more general form of autospectral density should be investigated and it should not be limited to white noise and filtered white noise cases.

The design of reinforced concrete structures using strut-and-tie model was addressed in the last part of the thesis. A stress-dependent truss-continuum topology optimization has been proposed. In addition, the constuctability of reinforcement was also studied. Whereas, the construction cost per bar should be defined more accurately, since a single long bar should have the same construction cost as the one consists of a large number of short bars which currently has a much larger construction cost.

Topology optimization as a form finding design tool is useful to give inspirations in the preliminary design phase. Academically, the methodologies and solutions in this work pave the way for the future implementation of topology optimization governed by complex eigenvalue problems. Furthermore, the optimization framework for

stationary stochastic excitations provides a basic tool and reference for more sophisticated problems, such as problems governed by non-stationary stochastic process. The hybrid stress-dependent model can be used to optimize general composite materials.

Practically, with the derivation of complex eigenvalues and eigenvectors sensitivity, topology optimization for non-classically damped structures can be implemented and optimized. Also, the proposed stochastic topology optimization framework is very general, and it can be applied to consider other types of stochastic dynamic loads except for ground motions.

Appendix A

Three-Dimensional Force Flow Paths and Reinforcement Design in Concrete via Stress-Dependent Truss-Continuum Topology Optimization

A.1 Introduction

It is common practice in reinforced concrete design to divide structural components into two regions, one where plane sections remain plane and stresses linearly

vary on a cross-section, often referred as B-regions, and the other where the strain distribution is significantly nonlinear (e.g., near concentrated loads, corners, openings, etc.) known as discontinuous-regions, or D-regions. A common approach to designing B-regions is to assume the flow of forces can be represented as a truss. This truss analogy, first proposed by Ritter (1899) and Morsch (1909), assumes that the cracked concrete structure acts as a truss with top and bottom longitudinal chords and an inclined web composed of concrete strut. D-regions, on the other hand, have been designed using rules of thumb or past experience for many years. The landmark paper by Jrg Schlaich and his colleagues at the University of Stuttgart Schlaich et al. (1987) proposed generalizing the truss analogy, applying it in the form of strut-and-tie-models (STM) to both B-regions and D-regions. STM is a general truss model that consists concrete compression struts, steel tension ties, and joints. The use of STMs provides a lower bound on the strength of the actual structure which has been confirmed with plasticity theory (Marti, 1980). The option to design by STM exists in most reinforced concrete design specifications. Selecting appropriate STM configurations, however, can be difficult, as there are an infinite number of possibilities for a STM. Once selected, conventional methods can be used to solve the STM, such as the load path method (Marti, 1985). Another challenge is that the geometry and topology (connectivity) of the STM is strictly related to a particular load configuration and cannot be used for other loads without modification (Schlaich and Schafer, 1991). Topology optimization, an approach that uses mathematical programming to optimize

the layout of material within a design domain, offers a potential solution strategy; it is gaining momentum in the structural engineering community, with several firms using it to generate concepts for tall buildings (e.g. Baker et al. (2008); Stromberg et al. (2011); Sarkisian et al. (2009)) and it has shown promise for automating the identification of minimum strain energy STM. When using topology optimization, the design problem is posed and solved as an optimization problem with the governing mechanics embedded in the formulation. The optimization design variable is constructed to indicate material concentration at a given location. For example, element cross-sectional areas are typically used as the design variables in optimization of truss structures, while material volume fraction is used in topology optimization of continuum structures. The constitutive tensor of the material is then design dependent, and expressed as a function of the design variables. Sensitivity analysis accounts for this relation and is used to guide design decisions by the optimizer. In this work, the optimization objective is to design a STM with minimum internal strain energy (maximum stiffness) for the given load and domain (this problem is often referred to as minimum compliance design in literature). This design objective is widely supported, including by Schlaich et al. (1987) who stated that an effective model is one that represents a minimum energy distribution through the D-regions, numerical results obtained by Ali and White (2001) who demonstrated with nonlinear finite element modeling to collapse ultimate strength increases as truss stiffness increases, and experimental results obtained by Kuchma et al. (2008). An example from Moen and

APPENDIX A. THREE-DIMENSIONAL FORCE FLOW PATHS AND REINFORCEMENT DESIGN IN CONCRETE VIA STRESS-DEPENDENT TRUSS-CONTINUUM TOPOLOGY OPTIMIZATION

Guest (2010), given in Fig.A.1, is used to illustrate how topology optimization can be used to visualize force paths and to develop strut-and-tie models. The STM, based on the traditional method, is developed for a reinforced concrete deep beam in Fig.A.1a and superposed over experimental results from Nagarajan and Pillai (2008a). The dashed black lines indicate compression struts of the STM, and the red solid lines the tension ties and subsequently the designed locations of steel reinforcement placement. In this STM, the steel reinforcement is orthogonal to cracks at midspan, but loses efficiency near the supports where cracks are diagonal. Fig.A.1b shows an alternative STM developed by minimum compliance topology optimization using truss elements. The result here shows that the optimizer places steel orthogonal to the compression struts, creating a steel reinforcement layout that is horizontal at midspan but angled away from midspan, bridging cracks orthogonally and thus more efficiently.

Several works have proposed using the truss topology optimization approach to design STM (Ali and White, 2000; Ali, 1998; Ali and White, 2001; Biondini et al., 1999, 2001; Kumar, 1978; Moen and Guest, 2010). The approach begins by densely meshing the design domain with truss elements, creating what is termed a ground structure that essentially defines all candidate load paths. Topology optimization is then used to determine the cross-sectional areas of the elements. Elements whose areas approach zero are deemed inefficient and removed from the mesh. An advantage of using truss topology optimization is that steel ties are guaranteed to be straight and can be sized based on axial forces directly output from the STM. Optimal layouts

APPENDIX A. THREE-DIMENSIONAL FORCE FLOW PATHS AND REINFORCEMENT DESIGN IN CONCRETE VIA STRESS-DEPENDENT TRUSS-CONTINUUM TOPOLOGY OPTIMIZATION

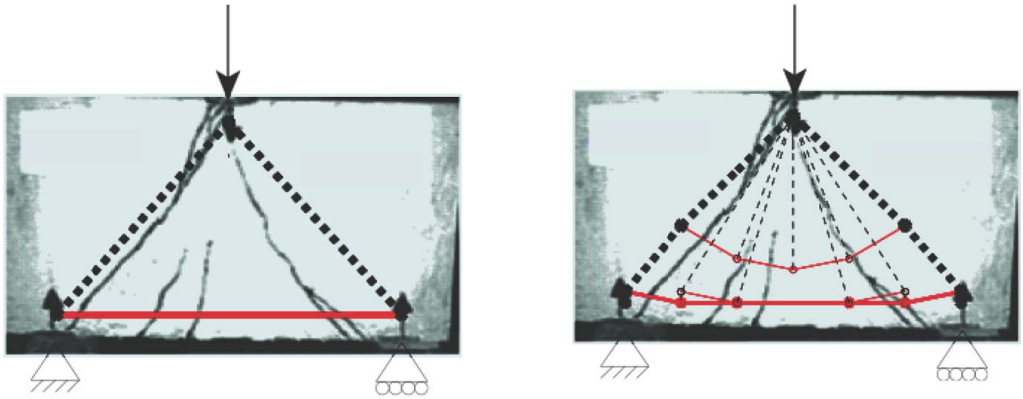

Figure A.1: Compare (a) traditional STM and (b) minimum compliance STM derived with topology optimization. Black dashed lines represent compression carried by the concrete, red solid lines represent tension carried by the reinforcing steel. Experimental results provided in the background are taken from Nagarajan and Pillai (2008a).

can also be made practical by limiting complexity in the initial ground structure (see e.g., Gaynor et al. (2012)). Solutions are dependent on the initial ground structure and thus simpler ground structures may lead to simpler topologies, but at the cost of material efficiency. One must therefore balance material and labor cost in selecting the most appropriate STM. Continuum, or free-form, topology optimization has also been used to optimize STM(Bruggi, 2009, 2010; Guan, 2005; Guan and Doh, 2007; Kim and Baker, 2002, 2001; Kwak and Noh, 2006; Lee et al., 2007; Leu et al., 2006; Liang, 2005, 2006; Nagarajan and Pillai, 2008b). In this approach, the design domain is discretized with finite elements, typically four node quadrilaterals in two dimensions, and the volume fraction of elements serve as the design variables. A volume fraction of zero indicates the element is not part of the STM model, or is non-load carrying concrete. A volume fraction of one indicates the element is part of the STM, or is load carrying, with principal stresses indicating whether the element is part of a compression or tension member. One of the disadvantages of this method is that tension regions are not defined as discrete bars, requiring post-processing of the continuum results to produce truss representations to size steel reinforcement. Design complexity is also more difficult to control directly. Inclined reinforcing steel, for example, can not be controlled, though general complexity can be influenced by controlling member length scales (see discussions in Gaynor et al. (2012); Moen and Guest (2010)). The advantage of continuum topology optimization is that material can be added or removed from any point in the design domain, meaning the optimizer

dictates locations of joints and connectivity thereby eliminating dependence on the mesh. The vast majority of the aforementioned topology optimization works assume linear elastic, isotropic (for continuum) constitutive equations and equivalent elastic moduli for steel reinforcement and concrete. Exceptions to this include Bogomolny and Amir (2012) who used nonlinear material-dependent elastoplastic models with the goal of enhancing performance at ultimate limit state. Luo and Kang (2013) developed a two-material topology optimization scheme with considering concrete compressive strength constraint and the volume constraint of steel. Another recent strategy has involved using continuum meshes embedded with truss elements. The truss elements are meant to represent steel reinforcement and, as truss elements, are placed in straight segments with topological complexity controllable with initial ground structure selection, aiding construction. Axial forces are also directly output from the model, enabling steel sizing. The continuum mesh is meant to represent the concrete compression load paths. Topological complexity is not an issue in compression load paths as they are simply idealized subdomains of the larger concrete design domain, and thus are not explicitly constructed. This idea was implemented in Gaynor et al. (2012) using stress-dependent, bilinear elastic moduli with magnitudes constructed to require tension to be carried by the steel truss elements and compression by the concrete continuum elements. Specifically, the tension modulus of the truss elements was set to the modulus of steel and the compression modulus to zero. For the continuum elements, the compression modulus was set to the

modulus of concrete and the tension modulus to a very small magnitude, and these were related through an orthotropic constitutive relation proposed by Darwin and Pecknold (1977). This model was shown to produce load direction dependent STM. Perhaps more importantly, it was shown to properly identify and reinforce regions of load spreading that cause the formation of minor principal stresses that are tensile (for example, transverse reinforcement in a column). We note the work of Amir and Sigmund (2013) also used truss elements embedded in continuum, but focused instead on improving ultimate strength using material-dependent, continuum damage models with strain-softening to guide placement of steel reinforcement. While these more sophisticated topology optimization methods and constitutive relations continue to show promise in STM design, they have been limited to two-dimensional structural domains. Only a few papers have investigated generating three-dimensional STM with topology optimization, and the majority of these have assumed linear elastic behavior (e.g., Bruggi (2009); Guest and Moen (2010); Leu et al. (2006)) with only Amir and Sigmund (2013) considering nonlinearity. It is the goal of this work to create a new three-dimensional automated tool for visualizing the flow of forces in reinforced concrete structural members and for designing optimized STM. In particular, the truss-continuum hybrid model initially developed in Gaynor et al. (2012) is generalized to account for more complex 3D stress states based on the bilinear stress dependent materials theory. As in the original 2D work, this approach will be shown to identify and reinforce regions of tensile minor principal stresses. A fea-

ture that is missed in conventional STM and those found with linear elastic topology optimization.

A.2 Hybrid Truss-Continuum Topology Optimization and Stress-Dependent Constitutive Relations

The hybrid truss-continuum approach attempts to leverage the advantages of both truss and continuum topology optimization. That is steel truss ties are placed in straight segments, with complexity directly influenced by the ground structure selected by the designer, and with axial forces directly output from the model for reinforcement sizing. This is in contrast to the concrete continuum compression paths, which are free to take any shape or inclination and need not be post-processed for sizing, as these paths are subdomains of the concrete structure and are not explicitly constructed.

The hybrid concept requires that tensile stresses be carried by the truss elements and compressive stresses carried by the continuum. This is achieved using bilinear (stress dependent) elastic moduli for the truss and continuum elements. Although isotropy is typically assumed for the continuum material, it was shown in Gaynor et al. (2012) that the major principal stresses govern the stiffness assignment to an element, and that this may consequently misrepresent regions where the major and minor

principal stresses are different directions. This is particularly problematic for STM when the major principal stresses are compressive and the minor principal stresses are tensile, as the optimizer would not place reinforcement to carry these tensile stresses. This was corrected in Gaynor et al. (2012) using a square symmetric constitutive relation with rotation dependence, and is extended here to three dimensions using an orthotropic material model. The hybrid mesh and orthotropic stress-dependent models are described below.

A.2.1 Hybrid Truss-Continuum Domain Discretization

As stated in the introduction, truss topology optimization typically begins with a densely meshed domain, referred to as ground structure (e.g., A.2), and the cross-sectional areas of the truss elements are then optimized. Low area elements are then removed from the ground structure as inefficient and elements remaining represent the STM. In continuum topology optimization, the design domain is discretized with finite elements and the optimizer is tasked with determining the volume fraction within each element, with volume fractions of zero and one indicating void and solid elements, respectively. The connectivity of the solid elements then represents the STM, with the major principal stresses indicated whether the member is a compression strut or tension tie.

For the hybrid truss-continuum approach, we simply combine the two discretizations onto a mesh of shared nodes. A.2c illustrates this idea for a very simple domain

meshed with 27 continuum elements and 28 truss elements. The truss and continuum elements are connected, and therefore transfer forces, wherever they share a node. In A.2c, the meshes are connected at every fourth node of the continuum mesh. In general, the truss domain is meshed more coarsely than the continuum domain to prevent excessive complexity of the steel reinforcing network (see Gaynor et al. (2012) for additional discussion).

A.2.2 Bilinear Material Model

In order to direct tensile forces to the steel and compression forces to the concrete, the approach taken here is to use negligible tensile stiffness for the concrete, and negligible compressive stiffness for the steel. We note this will prevent the appearance of compression steel, but this is consistent with the STM approach. A key challenge in such an approach is that the elastic moduli are not only nonlinear (bilinear), but that the continuum concrete models are dependent on the relative orientation of the principal stresses, adding a rotation dependency. In 2D, Gaynor et al. (2012) proposed a novel idea to capture this effect by using a 2D orthotropic material model originally proposed by Darwin and Pecknold (1977). It can be seen that this model is actually a special case of the generalized 3D bilinear material model proposed by Ambartsumyan and Khachatryan (1966) with some specific requirements that shear modulus is independent of axis orientation. Ambartsumyan and Khachatryan (1966) assumed Youngs modulus and Poissons ratio are E_t and ν_t, respectively, when the

APPENDIX A. THREE-DIMENSIONAL FORCE FLOW PATHS AND REINFORCEMENT DESIGN IN CONCRETE VIA STRESS-DEPENDENT TRUSS-CONTINUUM TOPOLOGY OPTIMIZATION

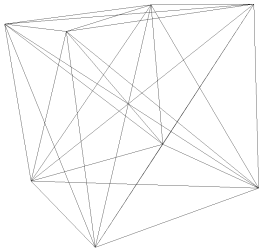

(a) Truss model

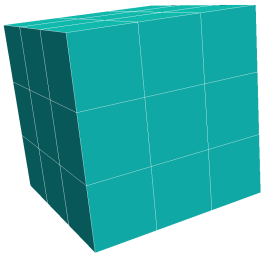

(b) Continuum model

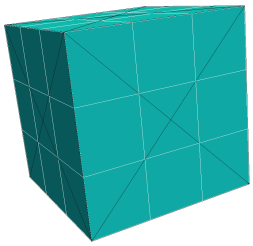

(c) Hybrid truss-continuum model

Figure A.2: Example of truss, continuum, and hybrid mesh schemes

corresponding principal stress is in tension along certain direction; and that Youngs modulus and Poissons ratio are E_c and ν_c, respectively, when the corresponding principal stress is in compression along certain direction, but ignores shear modulus. Liu and Meng (2002) discussed the influence of shear modulus on the convergence of numerical calculations and showed that the solution is not stable without considering shear modulus. Mathematically, the improved constitutive equation can be shown as follows (Liu and Meng (2002)):

$$\boldsymbol{\varepsilon}_p = \boldsymbol{a}\boldsymbol{\sigma}_p = \boldsymbol{d}^{-1}\sigma_p \tag{A.1}$$

where $\boldsymbol{\varepsilon}_p = \lfloor \varepsilon_{p1}, \varepsilon_{p2}, \varepsilon_{p3}, 0, 0, 0 \rfloor^T$ and $\boldsymbol{\sigma}_p = \lfloor \sigma_{p1}, \sigma_{p2}, \sigma_{p3}, 0, 0, 0 \rfloor^T$ denote the complete stress and strain vectors in the principal stress coordinate system, respectively. Tensors $\boldsymbol{a}$ and $\boldsymbol{d}$ are the flexibility tensor and constitutive tensor, respectively. In order to determine the constitutive tensor, the flexibility tensor $\boldsymbol{a}$ needs to be computed

firstly corresponding to principal stresses as follows:

$$(i) \quad if \quad \sigma_{p1} > 0, \sigma_{p2} > 0, \sigma_{p3} > 0;$$

$$a_{ii} = \frac{1}{E_t}(i = 1, 2, 3), \quad a_{ik} = -\frac{\nu_t}{E_t}(i, k = 1, 2, 3, i \neq k),$$

$$(ii) \quad if \quad \sigma_{p1} < 0, \sigma_{p2} < 0, \sigma_{p3} < 0;$$

$$a_{ii} = \frac{1}{E_c}(i = 1, 2, 3), \quad a_{ik} = -\frac{\nu_c}{E_c}(i, k = 1, 2, 3, i \neq k),$$

$$(iii) \quad if \quad \sigma_{p1} > 0, \sigma_{p2} > 0, \sigma_{p3} < 0;$$

$$a_{11} = a_{22} = \frac{1}{E_t}, \quad a_{22} = \frac{1}{E_c}, \quad a_{12} = a_{21} = a_{31} = a_{32} = -\frac{\nu_t}{E_t},$$

$$a_{13} = a_{23} = -\frac{\nu_c}{E_c}$$

$$(iiii) \quad if \quad \sigma_{p1} > 0, \sigma_{p2} < 0, \sigma_{p3} < 0;$$

$$a_{11} = \frac{1}{E_c}, \quad a_{22} = a_{33} = \frac{1}{E_t}, \quad a_{12} = a_{13} = a_{23} = a_{32} = -\frac{\nu_c}{E_c},$$

$$a_{21} = a_{31} = -\frac{\nu_t}{E_t} \tag{A.2}$$

By assuming normal stresses and shear stresses are decoupled, the coefficients associated with three principle stresses in the constitutive tensor then can be obtained by inverting corresponding coefficients in the flexibility tensor $\boldsymbol{a}$. The shear coefficients d_{44} , d_{55} , and d_{66} can be obtained without knowing a_{44} , a_{55} ,and a_{66} and computed by assuming the following

$$d_{44} = d_{55} = d_{66} = \frac{\eta E_t + (1 - \eta)E_c}{2\eta(1 + \nu_t) + 2(1 - \eta)(1 + \nu_c)} \tag{A.3}$$

where η is equal to the ratio of the sum of positive principal stresses and the sum of absolute value of all principal stresses, thus $0 \leq \eta \leq 1$. Then the constitutive tensor

in global coordinate system, denoted as $\boldsymbol{D}$, can be obtained as follows:

$$\boldsymbol{D} = \boldsymbol{L}^T \boldsymbol{d} \boldsymbol{L} \tag{A.4}$$

$$\boldsymbol{L} = \begin{bmatrix} l_1^2 & m_1^2 & n_1^2 & l_1 m_1 & m_1 n_1 & n_1 l_1 \\ l_2^2 & m_2^2 & n_2^2 & l_2 m_2 & m_2 n_2 & n_2 l_2 \\ l_3^2 & m_3^2 & n_3^2 & l_3 m_3 & m_3 n_3 & n_3 l_3 \\ 2l_1 l_2 & 2m_1 m_2 & 2n_1 n_2 & l_1 m_2 + l_2 m_1 & m_1 n_2 + m_2 n_1 & n_1 l_2 + n_2 l_1 \\ 2l_2 l_3 & 2m_2 m_3 & 2n_2 n_3 & l_2 m_3 + l_3 m_2 & m_2 n_3 + m_3 n_2 & n_2 l_3 + n_3 l_2 \\ 2l_3 l_1 & 2m_3 m_1 & 2n_3 n_1 & l_3 m_1 + l_1 m_3 & m_3 n_1 + m_1 n_3 & n_3 l_1 + n_1 l_3 \end{bmatrix} \tag{A.5}$$

where $\boldsymbol{L}$ is the transformation matrix and l_i , m_i and n_i are the direction cosines of the i-th principal stress to global $x-$, $y-$, and $z-$directions, respectively. The stiffness matrix is then formulated in the standard manner.

The elastic properties for concrete and steel used herein are illustrated in Fig.A.3. Youngs moduli for the concrete are assumed 24.9 GPa (3600 ksi) in compression and 2.0 GPa (290 ksi) in tension, while moduli for the steel are assumed 200 GPa (29000 ksi) in tension and zero in compression. We emphasize that these moduli are chosen to focus tensile forces in the steel and compressive forces in the concrete, consistent with STM methodology. It is also noted that the tensile stiffness of the concrete is negligible but nonzero to prevent singularities in the global stiffness matrix.

APPENDIX A. THREE-DIMENSIONAL FORCE FLOW PATHS AND REINFORCEMENT DESIGN IN CONCRETE VIA STRESS-DEPENDENT TRUSS-CONTINUUM TOPOLOGY OPTIMIZATION

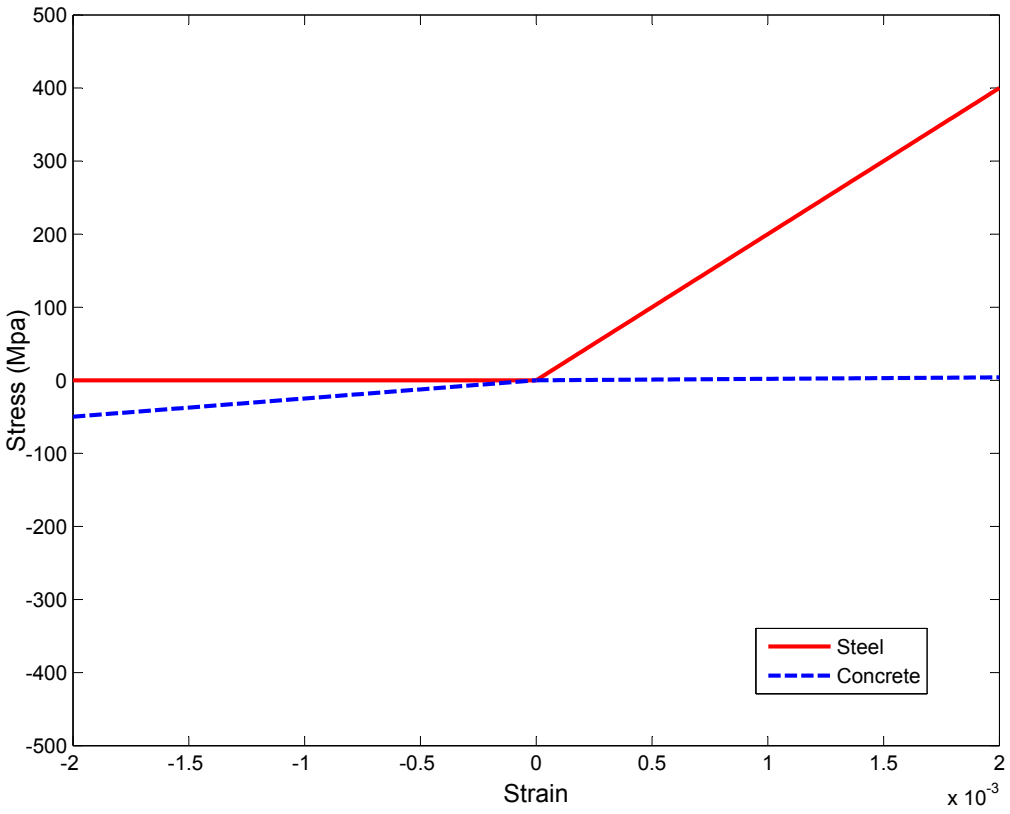

Figure A.3: Stress-strain relationship for continuum concrete and truss steel models

A.2.3 Finite Element Solution Scheme

Since the constitutive tensor is a function of the stress state of a point, which is not known in advance, it is necessary to use an iterative solution strategy. As the moduli are bilinear, load stepping is not required. More simply a direct iterative method is used where the constitutive tensor for each element is adjusted and element stiffness re-computed based on the computed principal stresses in the previous FE iteration.

A.3 Problem Formulation and Solution Algorithm

A.3.1 Hybrid Topology Optimization Formulation

The minimum compliance design problem is to minimize external work (maximize stiffness) of the system using a maximum allowable volume V_0 of load-carrying material (material in the STM). This is expressed formally for the hybrid, stress-dependent

truss-continuum approach as

$$\begin{aligned} \min_{\boldsymbol{\rho}_c,\boldsymbol{\rho}_t} \quad & f(\boldsymbol{\rho}_c,\boldsymbol{\rho}_t) = \boldsymbol{F}^T\boldsymbol{u} \\ s.t. \quad & \boldsymbol{K}(\boldsymbol{\rho}_c,\boldsymbol{\rho}_t,\boldsymbol{\sigma}_c,\boldsymbol{\sigma}_t)\boldsymbol{u} = \boldsymbol{F} \\ & \sum_{e\in\Omega_c} \rho_c^e v_c^e + \sum_{e\in\Omega_t} \rho_t^e v_t^e \leq V_0 \\ & 0 \leq \rho_c^e \leq 1, \quad \forall e \in \Omega_c \\ & 0 \leq \rho_t^t, \quad \forall e \in \Omega_t \end{aligned} \tag{A.6}$$

where $\boldsymbol{F}$ are the applied nodal loads, $\boldsymbol{u}$ are the nodal displacements, $\boldsymbol{\rho}_c$ are the design variables representing the volume fraction of the continuum concrete elements and $\boldsymbol{\rho}_t$ the design variables representing the cross-sectional areas for the steel truss elements. The variable v_c^e denotes the element volume for continuum and v_t^e the element length for the truss elements. Note that the truss and continuum members pull from the same total volume, allowing steel and concrete to be used as necessary to maximize system stiffness. The global stiffness matrix $\boldsymbol{K}$ is assembled in the usual manner from the continuum and truss elemental stiffness matrices $\boldsymbol{K}_c^e$ and $\boldsymbol{K}_t^e$,respectively, which are functions of the continuum element stress tensors $\boldsymbol{\sigma}_c$ and truss element axial stresses $\boldsymbol{\sigma}_t$, respectively, as previously discussed. Specifically, the global stiffness matrix is given as

$$\boldsymbol{K}(\boldsymbol{\rho}_c,\boldsymbol{\rho}_t,\boldsymbol{\sigma}_c,\boldsymbol{\sigma}_t) = \underset{e\in\Omega_c}{\mathrm{A}} \boldsymbol{K}_c^e(\rho_c^e,\sigma_c^e) + \underset{e\in\Omega_t}{\mathrm{A}} \boldsymbol{K}_c^e(\rho_t^e,\sigma_t^e) \tag{A.7}$$

$$\boldsymbol{K}_c^e(\rho_c^e,\sigma_c^e) = ((\rho_c^e)^{p_c} + \rho_{min}^e)\boldsymbol{K}_{0c}^e(\sigma_c^e) \tag{A.8}$$

$$\boldsymbol{K}_t^e(\rho_t^e, \sigma_t^e) = (\rho_t^e)\boldsymbol{K}_{0t}^e(\sigma_t^e) \tag{A.9}$$

where $\boldsymbol{K}_{0c}^e(\sigma_c^e)$ and $\boldsymbol{K}_{0t}^e(\sigma_t^e)$ are the element stiffness matrices for unit design variable magnitude for the concrete and reinforcing steel, respectively. These two matrices are functions of stress and thus have to be determined iteratively in each optimization iteration. The variable ρ_{min}^e is equal to a small positive number to maintain positive definiteness of the global stiffness matrix. Using the exponent $p_c = 3$ in Eq. (A.8) is a standard approach in topology optimization known as the Solid Isotropic Material with Penalization (SIMP) method (Bendsøe, 1989). This approach essentially reduces the stiffness of elements whose volume fractions are between zero and one, thereby making them uneconomical and driving the optimizer to select or for each element, indicating non-load carrying and (compression) load carrying concrete, respectively.

A.3.2 Implementation

As previously discussed, the equilibrium conditions are governed by a nonlinear material model and thus require iterative analysis. However, load-stepping is not required due to the fact that the material is bilinear elastic, meaning they are not load-magnitude dependent. The analysis is initialized by assuming all truss elements have $E_t = 200GPa$ and that the continuum is isotropic with $E_c = 24.9GPa$ (or equivalently that all principle stresses are assumed compressive). Nodal displacements and element principal stresses are then computed and the constitutive tensors are updated according to Eq. (A.2) and element stiffness matrices according to Eqs. (A.8)

and (A.8). The analysis is repeated and constitutive tensors updated until convergence in displacements is satisfied. The convergence criterion used herein is defined as $\|\boldsymbol{u}_i - \boldsymbol{u}_{i-1}\|/\|\boldsymbol{u}_{i-1}\| \leq \varepsilon$, where ε is a very small positive number (e.g. 10^{-6}). Although oscillations were not observed in the two-dimensional stress-dependent work of Gaynor et al. (2012) and Liu and Qiao (2011), oscillations in the sign of the minor principal stresses were detected when solving the three-dimensional problems considered herein. However, these oscillations occurred in the void (non-load carrying) elements, whose stiffness is negligible but required to be nonzero in order to maintain positive definiteness of the global stiffness matrix. As they have no detectable effect on the optimized STM, the convergence check was limited to the deflection degrees of freedom associated with non-void elements, a similar strategy as was used by Buhl et al. (2000) for topology optimization under large deflections. Finally, we note sensitivities are computed using the converged results. This implementation is illustrated by the flow chart in Fig.A.4.

A.4 Hybrid Stress-Dependent Topology Optimization Results

Four examples are presented to show the effectiveness of the proposed hybrid topology optimization algorithm. The first example is used to clearly illustrate that the proposed algorithm is capable of capturing transverse tensile stresses that occur

APPENDIX A. THREE-DIMENSIONAL FORCE FLOW PATHS AND REINFORCEMENT DESIGN IN CONCRETE VIA STRESS-DEPENDENT TRUSS-CONTINUUM TOPOLOGY OPTIMIZATION

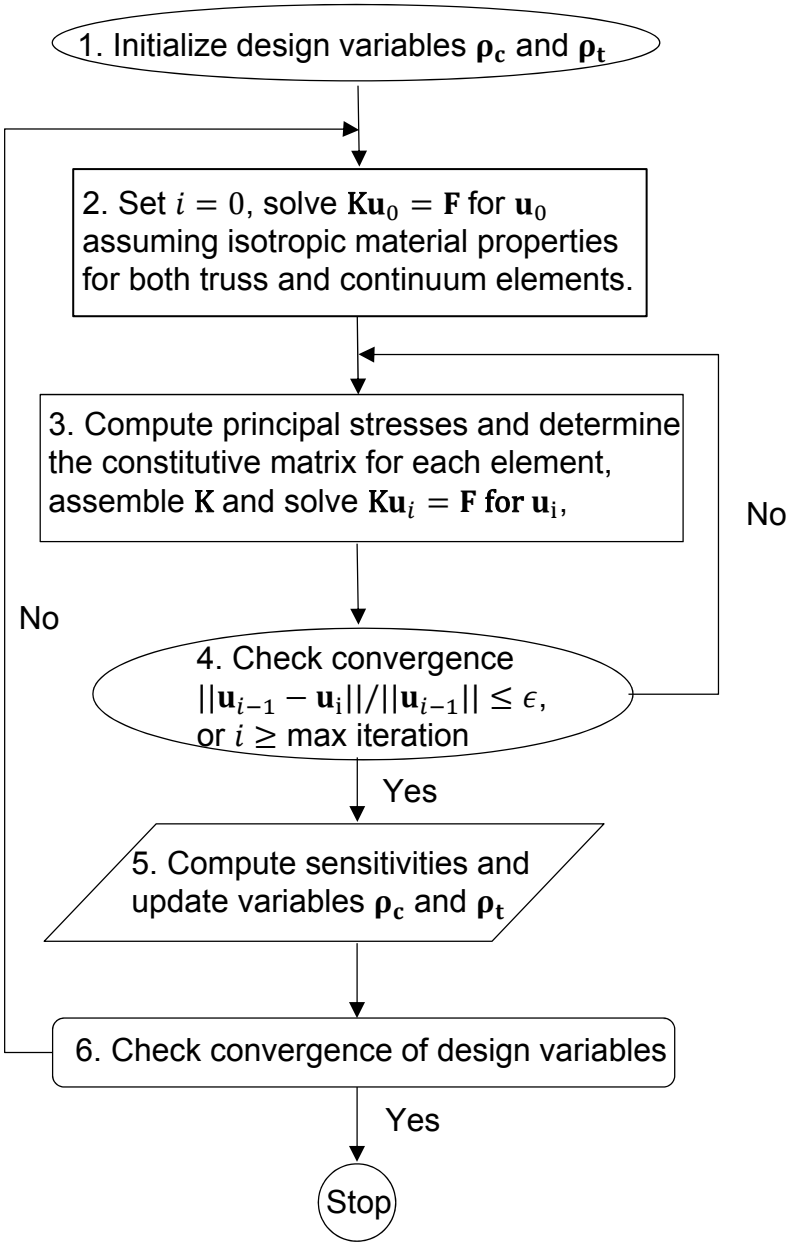

Figure A.4: Flow chart of the topology optimization scheme

due to load spreading. The algorithm is then used to design the STM for a pile cap, hammerhead bridge pier, and anchorage zone of an externally prestressed concrete structure. All examples use 8-node brick elements for the continuum, assume an initial guess of uniformly distributed material, and use a unit load for all concentrated applied loads unless otherwise mentioned.

A.4.1 Concrete Block

The first example is the concrete block shown in Fig.A.5, essentially a 3D version of the problem studied in Gaynor et al. (2012). The column has a square cross section with height to width ratio of 3. The column is subjected to a compressive force acting over a square domain comprising the center 16% of the top surface. The magnitude of volume constraint is equal to 50% of the total volume. This structure is meant to represent the anchorage zone of a prestressed beam or a column. Figs.figs. A.5b and A.5c contain the optimal topologies found using linear elastic continuum-only and truss-only topology optimization models, respectively. As discussed in previous work Gaynor et al. (2012), these STM models indicate compressive load paths only, thus suggesting reinforcing steel is not required. However, though the major principal stresses are compressive, the minor principal stresses in the region under the applied load are tensile due to the force spreading effect. The solution found using the proposed stress dependent truss-continuum approach is shown in Figs.figs. A.5d and A.5e These figures clearly illustrate that the hybrid approach captures these tensile stresses

and places horizontal steel members to carry the tension. Not surprisingly, the vertical distance that reinforcing steel is required is approximately equal to the width of the compression block.

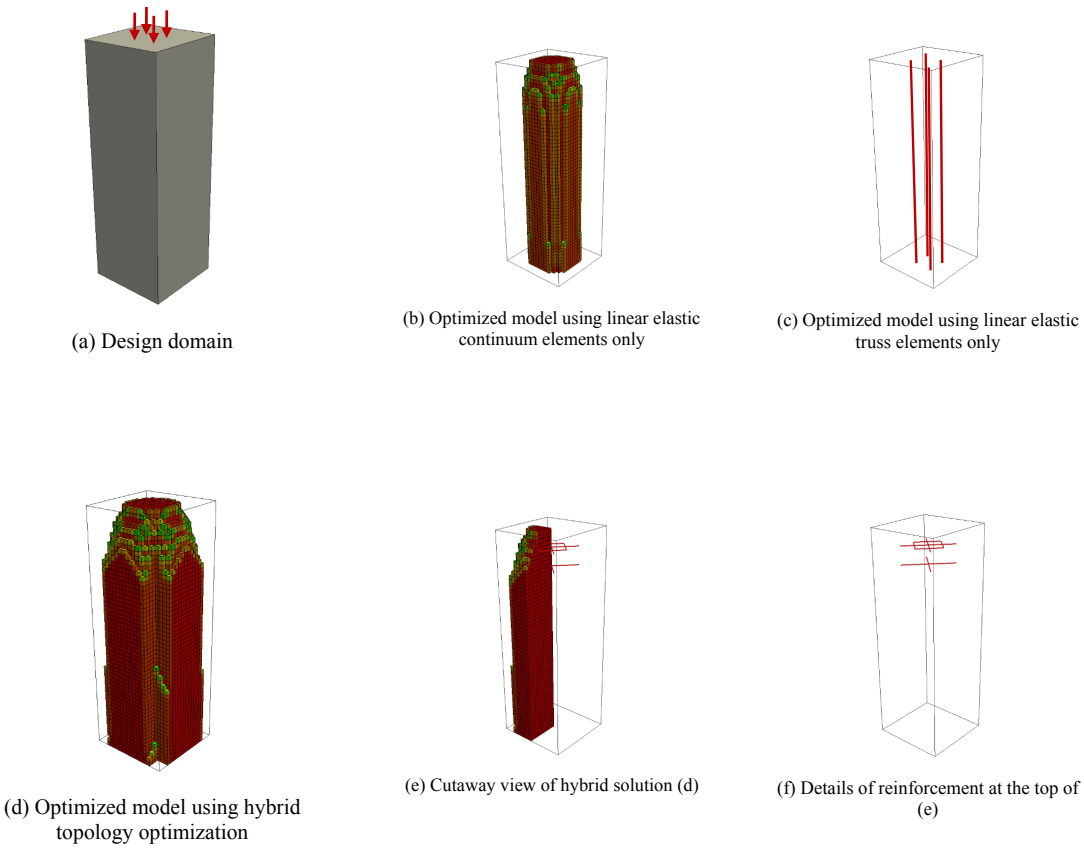

Figure A.5: Topology optimized solutions for the concrete block design example (a). Traditional solutions (b,c) indicate only compressive load paths, while the hybrid model correctly

A.4.2 Pile Cap

A pile cap, whose function is to transfer load from a column to piles, is shown in Fig.A.6a. A STM found using continuum topology optimization with linear elastic material model is shown in Fig.A.6b. One of the challenges with this solution is the tension zone on the bottom of the domain is essentially a plate. One would then need to post-process this design to create a rebar layout that mimics this plate system. One could also adjust the parameters, such as use smaller volume fraction or impose a maximum length scale on the plate (Guest, 2009a), but ultimately the continuum algorithm is free to design any shaped tension path. In contrast, the optimized STM using the stress dependent truss-continuum approach is shown in Fig.A.7. The volume constraint is set to 0.1. It can been seen that compression is focused into four primary load paths (Fig.A.7b) connecting each pile to the load, and this is optimally balanced with a discrete tension system of rebar that includes inclined members that connect to a central tension system plane near the bottom of the domain (Fig.A.7c).

A.4.3 Hammerhead Pier

Fig.A.8a shows a hammerhead bridge pier loaded with eight vertical concentrated forces from deck girders. Exploiting the symmetry, only a quarter of the pier is modeled. 5% of the total volume (truss and continuum together) is used as the volume constraint. Fig.A.8b shows the optimal STM found using the proposed hybrid

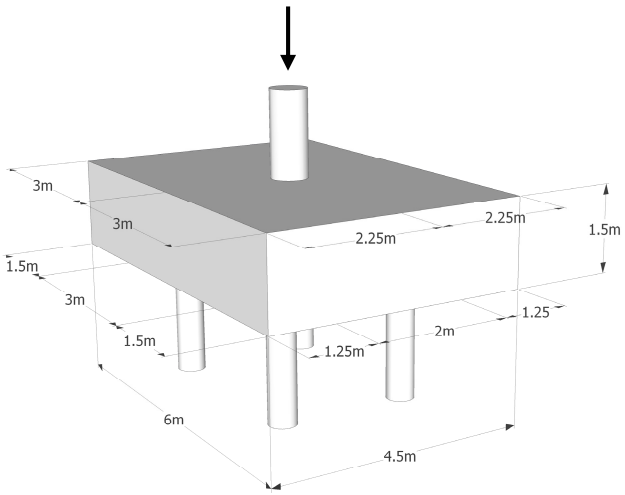

(a) Pile cap design domain

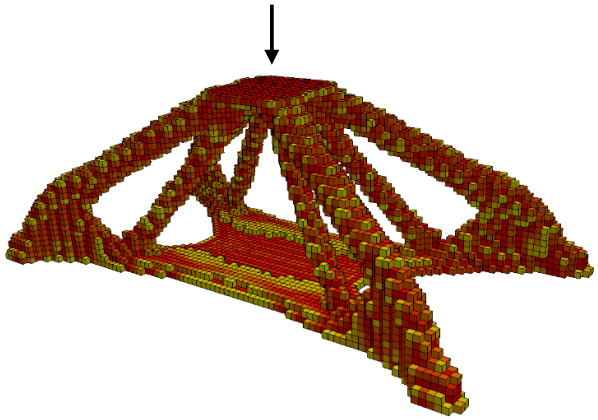

(b) Linear elastic continuum solution

Figure A.6: Pile cap design domain and linear elastic continuum solution

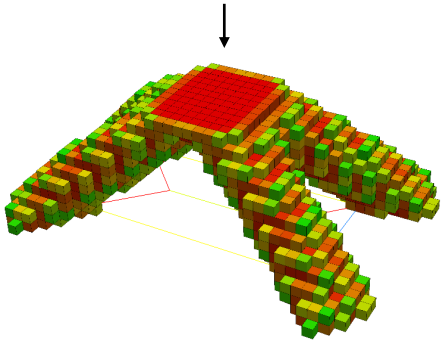

(a) Optimized STM

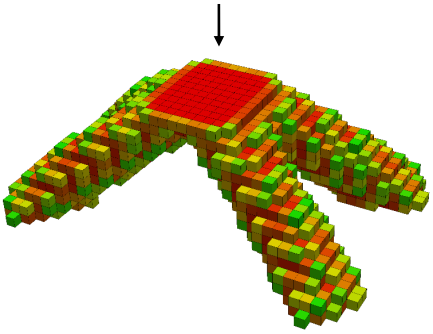

(b) Optimized compression (concrete) load paths

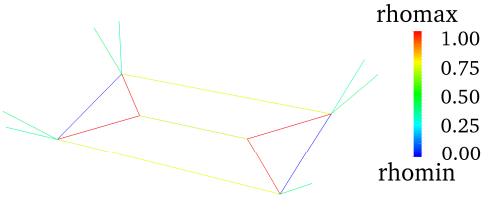

(c) Optimized tension (steel) load paths

Figure A.7: Topology optimized solutions for the pile cap example

topology optimization approach, with load-carrying concrete highlighted in Fig.A.8c and steel rebar in Fig.A.8d. It is clear the optimizer has designed horizontal tension ties near the top surface of the pier with inclined reinforcement to balance the inclined compression paths as the load move towards the central core of the pier.

A.4.4 Anchorage Zone of an Externally Prestressed concrete beam

The anchorage zone of an externally prestressed concrete beam is a typical discontinuous region. In order to transfer the external prestressing force to the entire beam, solid concrete diaphragms are added to the ends. Due to the symmetry, half of the structure, shown in Fig.A.9, is optimized. This design is discretized by 6,000 8-node brick elements and 20,000 truss elements. The volume constraint is equal to 5% of the total volume. The external load is transferred from the point of load application to the beam according to the compression load paths shown in Fig.Figures A.9b and A.9d. Primary tension load paths, shown in Fig.A.9c, are located near the applied load and on the back face of the anchorage zone. These results are consistent with design practice that places splitting reinforcement on both anchorage faces. The advantage of the topology optimization solution is that the rebar size, spacing, and orientation is automatically identified instead of asking an engineer to use their judgment in performing complex 3D STM calculations. In the anchorage concrete block, inclined truss elements with small areas are needed to carry tension as the anchorage

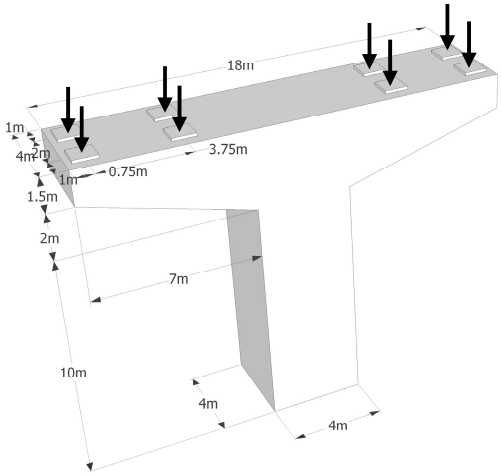

(a) Hammerhead pier design domain

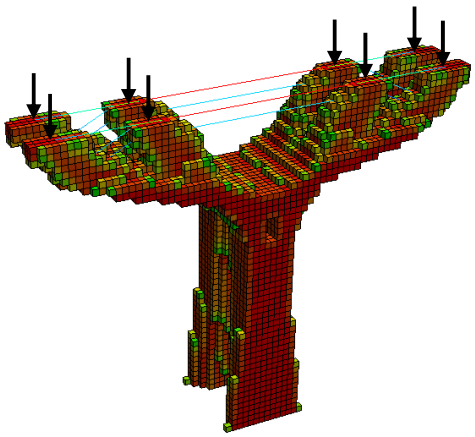

(b) Optimized STM

Figure A.8: Topology optimized solutions for the hammerhead pier example

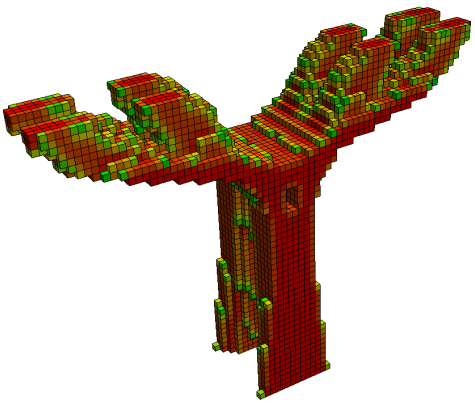

(c) Optimized compression (concrete) load paths

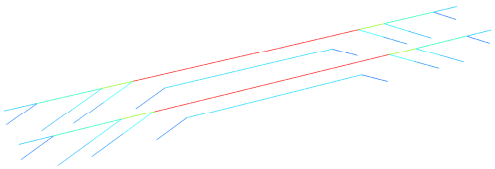

(d) Optimized tension (steel) load paths

Figure A.8: Topology optimized solutions for the hammerhead pier example

force spreads into the beam top flange.

A.5 Optimizing Reinforcement Layout in Concrete Design Considering Constructability

Although design complexity can be controlled through selection of the truss ground structure , placement cost of reinforcing steel has not been investigated. The presence of inclined reinforcing steel, for example, may increase labor costs and perhaps total costs of a system, over a simpler design of horizontal bars that is less efficient and thus uses more steel. Thus, considering construction cost is crucial to make the optimized results practical. Recently, Asadpoure et al. (2015) addressed a similar problem in the design of truss structures by adding a per-element unit cost to the material cost function. This cost was meant to represent the cost of placing a truss member into the structural system and the labor cost of making two connections. The approach is adapted here to the hybrid topology optimization approach and used to penalize, through cost, complex reinforcing patterns.

The minimum compliance (maximum stiffness) optimization problem we proposed

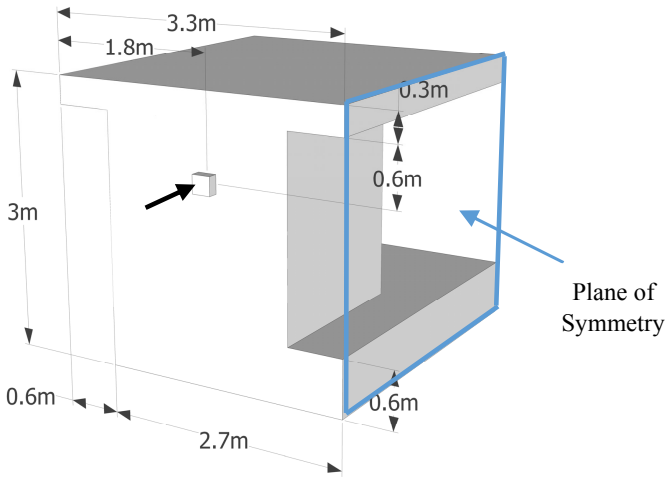

a) Design domain

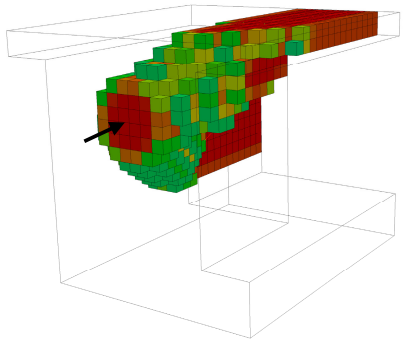

(b) Optimal compression load paths

Figure A.9: Topology optimized solutions for the prestressed beam example

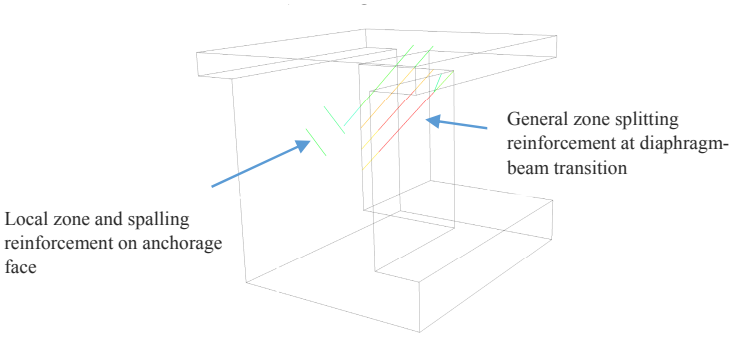

(c) Optimal tension load paths

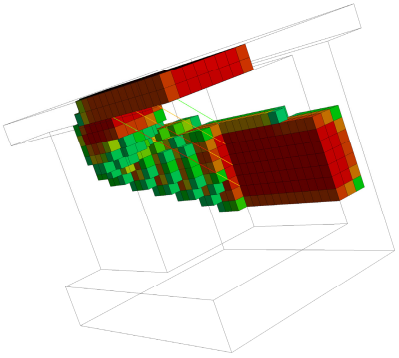

(d) Optimal STM rotated 90° about vertical axis

Figure A.9: Topology optimized solutions for the prestressed beam example

can then be stated as:

$$
\begin{aligned}
&\min_{\boldsymbol{\rho}_c,\boldsymbol{\rho}_t} \quad f(\boldsymbol{\rho}_c,\boldsymbol{\rho}_t) = \boldsymbol{F}^T\boldsymbol{u} \\
&s.t. \quad \boldsymbol{K}(\boldsymbol{\rho}_c,\boldsymbol{\rho}_t,\boldsymbol{\sigma}_c,\boldsymbol{\sigma}_t)\boldsymbol{u} = \boldsymbol{F} \\
&\qquad \sum_{e\in\Omega_c} \alpha_c^e \rho_c^e v_c^e + \sum_{e\in\Omega_t} \alpha_s^e \rho_t^e v_t^e + \sum_{e\in\Omega_t} \alpha_f^e H^e(\rho_t^e) \leq TC \\
&\qquad H^e(\rho_t^e) = 1 - e^{-\beta(\rho_t^e)} + (\rho_t^e)e^{-\beta} \\
&\qquad 0 \leq \rho_c^e \leq 1, \quad \forall e \in \Omega_c \\
&\qquad 0 \leq \rho_t^t, \quad \forall e \in \Omega_t
\end{aligned} \tag{A.10}
$$

where the second constraint is the total cost TC constraint, composed of the material cost M and construction cost C. In the total cost constraint, the material cost is computed as

$$
M(\rho_c^e,\rho_t^e) = \sum_{e\in\Omega_c} \alpha_c^e \rho_c^e v_c^e + \sum_{e\in\Omega_t} \alpha_s^e \rho_t^e v_t^e \tag{A.11}
$$

where α_c^e and α_t^e represent material cost per unit volume for concrete and steel, respectively. The construction cost, recently proposed in Asadpoure et al. (2015) to represent fabrication cost in discrete structures, is computed as

$$
C(\rho_c^e,\rho_t^e) = \sum_{e\in\Omega_t} \alpha_f^e H^e(\rho_t^e) \tag{A.12}
$$

where the function H represents the Heaviside step function such that any truss element with cross-sectonal area greater than zero counts as an element that must be constructed, or placed. Note that only the truss (steel) elements appear in this

function as the continuum elements represent the concrete domain. The variable α_f^e denotes the construction cost of placing the element e. In truss structures, for example, it represented the labor cost of member placement (including crane time) and making two connections, one at each end of the member. The magnitude of the element construction cost is ultimately dictated by the local market and construction methods, but our goal herein is to show how the magnitude of this cost term can be used to influence the constructability of rebar schedules.

As the step function H is discrete, it must be regularized for use with gradient-based optimizers. We use the regularization function discussed in Asadpoure et al. (2015), originally proposed by Guest et al. (2004a) for projection methods in continuum topology optimization, given as follows:

$$H^e(\rho_t^e) = 1 - e^{-\beta(\rho_t^e)} + (\rho_t^e)e^{-\beta} \tag{A.13}$$

where β is a regularization parameter that dictates how aggressively the step function approximated (Guest et al., 2011a), set to 10 in this section. Note that using this expression, if a steel truss member achieves a non-zero cross-sectional area, this function yields a magnitude of one, which imposes the elements unit cost on the total cost function.

It is seen that when $\alpha_c^e = \alpha_s^e$ and $\alpha_f^e = 0$, this total cost constraint is equivalent to the simple volume constraint used in Yang et al. (2013). For the sake of comparing the material and construction costs and showing the effect of the latter on simplifying the optimized placement of reinforcing steel, α_c^e and α_s^e are set fixed and equal to unit.

Thus changing the value of will change the ratio of construction and material cost. We want to emphasize that the values of these parameters can be determined based on actual cost of concrete and steel, and local labor costs of placing steel bars.

The first numerical example is the benchmark simply-supported beam problem loaded at midspan, as shown in Fig.A.10a. A traditional STM is shown in Fig.A.10b along with a topology-optimized solution considering only material cost, without construction cost, in Fig.A.10c. It is well-known that minimum strain energy topologies will mimic the principal stress trajectories, and so we have enabled a fine structural topology to closely approximate this and emphasize the difference when considering constructability. Of course simpler topologies could be achieved by altering the initial ground structure (see Gaynor et al. (2012) for a discussion on this). Fig.A.10d displays the solution when significantly increasing the unit labor cost to unit material cost ratio. The topology clearly contains fewer bars and is a significantly simpler topology that would be easier (and cheaper) to construct. These bars, however, have significantly larger cross-sectional area, leading to a much larger total material cost than those found Fig.A.10c. The solution in Fig.A.10e was found by assigning a high cost to the use of inclined rebar relative to the cost of horizontal and vertical rebar. This led the algorithm to avoid using inclined rebar, despite there extreme structural efficiency for this design example. Note that two inclined bars did appear in the final topology, as the cost was not high enough to overcome their structural efficiency and corresponding material cost savings.

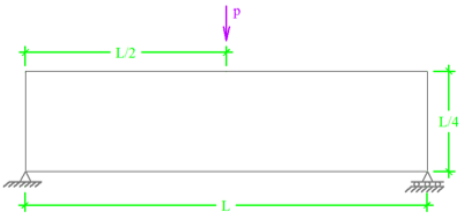

(a)

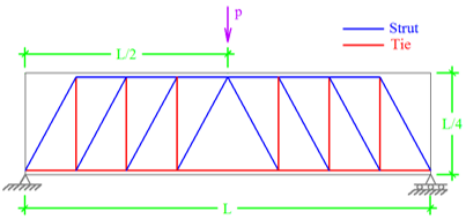

(b)

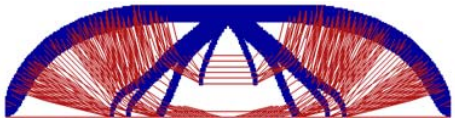

(c)

(d)

(e)

Figure A.10: Topology optimization of STM considering construction cost; (a) Design domain, (b) A traditional STM, (c) Optimized STM without considering construction cost($\alpha_c^e = \alpha_s^e = 1$ and $\alpha_f^e = 0$), (d) Optimized STM considering construction cost $\alpha_c^e = \alpha_s^e = 1$ and $\alpha_f^e = 2$ for all steel reinforcement, (e) Optimized STM considering construction cost $\alpha_c^e = \alpha_s^e = 1$ and $\alpha_f^e = 2$ for inclined rebar, $\alpha_f^e = 0.5$ for all others

Another benchmark example is a deep beam with cutouts as shown in Fig.A.11a. A traditional STM with horizontal and vertical steel ties only is illustrated in Fig.A.11b. Fig.A.11c gives a topology-optimized solution considering only material cost. It has been seen that it consists of a large number of steel rebar, which makes the proposed STM less practical. In Fig.A.11d, the result accounting for both material and construction costs has a much simpler STM. In Fig.A.11e, a different STM which has less inclined steel reinforcement is obtained by increasing the construction cost of these steel rebar. While these results should be considered preliminary, they show the potential of incorporating labor cost into STM optimization. Of course one of the key challenges is properly quantifying labor costs, which are highly driven by local markets. In this work, however, we simply express these costs as a ratio to material costs to illustrate the idea and explore the tradeoffs between material and constriction costs.

A.6 Conclusions

Topology optimization has recently been shown as an effective design tool for visualizing the flow of forces in concrete and producing efficient STM. This paper uses a hybrid truss-continuum model, following the idea of Gaynor et al. (2012), to focus tensile forces in the steel (truss) and compressive forces in the concrete (continuum). The work is extended herein to generalized concrete material constitutive equations to account for more complex three-dimensional stress states and domains. Key ad-

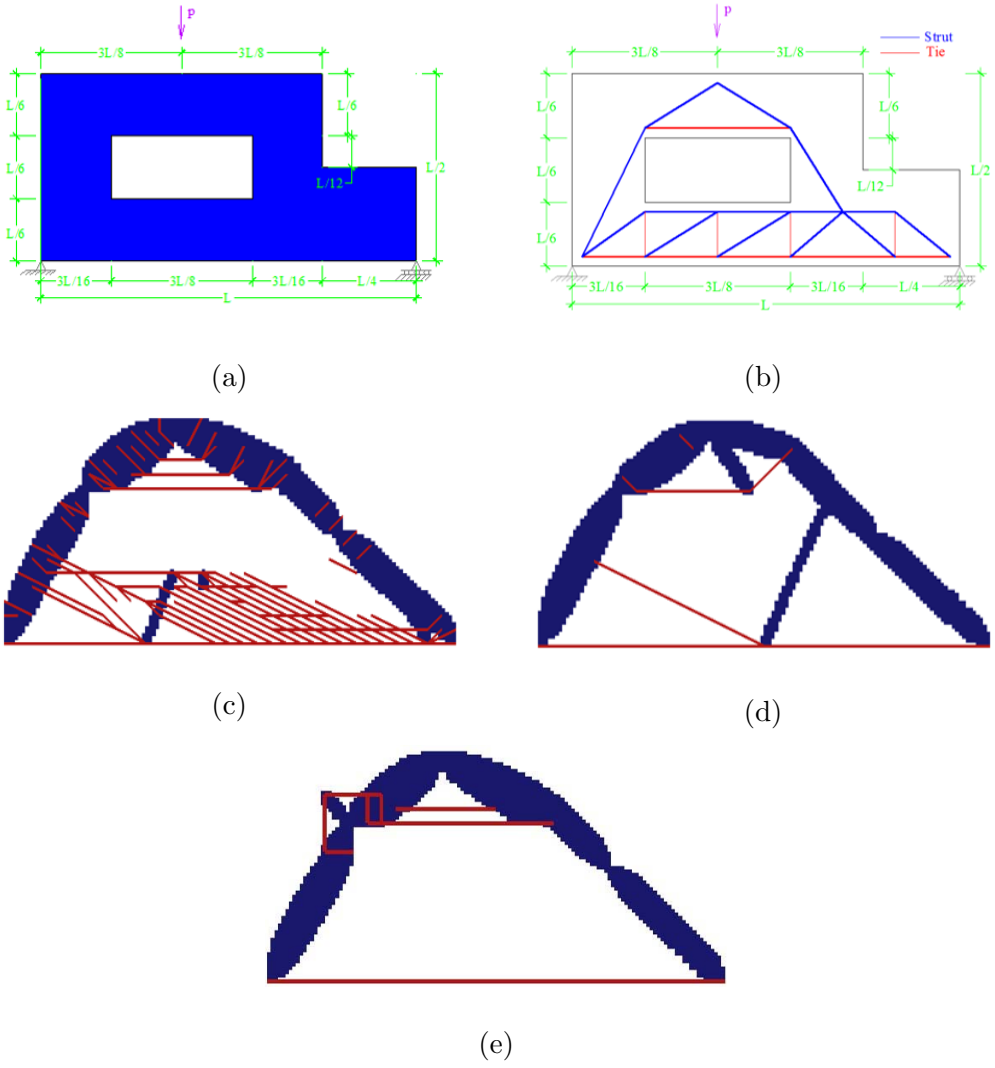

Figure A.11: Topology optimization of STM considering construction cost; (a) Design domain, (b) A traditional STM, (c) Optimized STM without considering construction cost($\alpha_c^e = \alpha_s^e = 1$ and $\alpha_f^e = 0$), (d) Optimized STM considering construction cost $\alpha_c^e = \alpha_s^e = 1$ and $\alpha_f^e = 2$,(e) Optimized STM considering construction cost $\alpha_c^e = \alpha_s^e = 1$ and $\alpha_f^e = 2$ for inclined rebar, $\alpha_f^e = 0.5$ for all others

vantages of the approach are that (i) the steel rebar is modeled by truss elements which directly determine the locations and, after a linear scaling based on the yield stress of the steel, the amount of reinforcing steel required, (ii) design complexity can be controlled through selection of the truss ground structure, and (iii) the bilinear hybrid model successfully captures tensile stresses that develop due to force spreading, an effect missed by linear elastic approaches.

More fundamentally, the approach offers the ability to focus compressive and tensile forces into specific structural elements, allowing treatment of other systems composed of stress-dependent constituents, such as cables and composites. Extension to nonlinear properties, such as optimizing for strength (Amir and Sigmund, 2013; Bogomolny and Amir, 2012) or ductility using compressive steel, may also be possible through this approach. There are also very practical functions still left to be treated formally by the optimization algorithm, such as incorporating constructability measurements into the optimization algorithm and accounting for detailing requirements.

While traditional topology optimization approaches consider only material cost, this work proposes including construction cost, which is also of great importance, into the topology optimization of STM. Following the work of Asadpoure et al. (2015), construction cost is estimated as a unit cost associated with placing a rebar element, with different elements potentially having different unit costs depending on their geometry and position. Although this is a simple cost model, results clearly illustrate that the complexity of STM can be influenced through this construction cost algo-

rithm. It is the goal of future work to develop more sophisticated, more realistic construction cost models.

Bibliography

H. M. Adelman and R. T. Haftka. Sensitivity analysis of discrete structural systems. *AIAA journal*, 24(5):823–832, 1986.

M. Ali and R. White. Formulation of optimal strut-and-tie models in design of reinforced concrete structures. *Special Publication*, 193:979–998, 2000.

M. A. Ali. Automatic generation of truss models for the optimal design of reinforced concrete structures. 1998.

M. A. Ali and R. N. White. Automatic generation of truss model for optimal design of reinforced concrete structures. *Structural Journal*, 98(4):431–442, 2001.

G. Allaire and F. Jouve. A level-set method for vibration and multiple loads structural optimization. *Computer methods in applied mechanics and engineering*, 194(30): 3269–3290, 2005.

S. A. Ambartsumyan and A. A. Khachatryan. The different-modules theory of elasticity. *Mechanics of Solids*, 1(6):64–67, 1966.

BIBLIOGRAPHY

O. Amir and O. Sigmund. Reinforcement layout design for concrete structures based on continuum damage and truss topology optimization. *Structural and Multidisciplinary Optimization*, 47(2):157–174, 2013.

A. Asadpoure, M. Tootkaboni, and J. K. Guest. Robust topology optimization of structures with uncertainties in stiffness–application to truss structures. *Computers & Structures*, 89(11):1131–1141, 2011.

A. Asadpoure, J. K. Guest, and L. Valdevit. Incorporating fabrication cost into topology optimization of discrete structures and lattices. *Structural and Multidisciplinary Optimization*, 51(2):385–396, 2015.

I. Babuška and J. Osborn. Numerical treatment of eigenvalue problems for differential equations with discontinuous coefficients. *Mathematics of Computation*, 32(144): 991–1023, 1978.

W. Baker, A. Beghini, J. Carrion, A. Mazeika, and A. Mazurek. Numerical tools in structural optimization. In *Proc., 6th Int. Conf. on Computation of Shell and Spatial Structures*, pages 772–775. Curran Associates Red Hook, NY, 2008.

F. Belblidia and S. Bulman. Constrained adaptive topology optimization for vibrating shell structures. *Structural and multidisciplinary optimization*, 22(2):167–176, 2001.

A. Ben-Tal and A. Nemirovski. Robust truss topology design via semidefinite programming. *SIAM Journal on Optimization*, 7(4):991–1016, 1997.

BIBLIOGRAPHY

M. P. Bendsøe. Optimal shape design as a material distribution problem. *Structural optimization*, 1(4):193–202, 1989.

M. P. Bendsøe and O. Sigmund. Material interpolation schemes in topology optimization. *Archive of applied mechanics*, 69(9-10):635–654, 1999.

O. R. Bilal and M. I. Hussein. Ultrawide phononic band gap for combined in-plane and out-of-plane waves. *Physical Review E*, 84(6):065701, 2011.

F. Biondini, F. Bontempi, and P. Malerba. Optimal strut-and-tie models in reinforced concrete structures. *Computer Assisted Mechanics and Engineering Sciences*, 6(3-4):280–293, 1999.

F. Biondini, F. Bontempi, and P. G. Malerba. Stress path adapting strut-and-tie models in cracked and uncracked rc elements. *Structural Engineering and Mechanics*, 12(6):685, 2001.

F. Bloch. Quantum mechanics of electrons in crystal lattices. *Z. Phys*, 52:555, 1928.

M. Bogomolny. Topology optimization for free vibrations using combined approximations. *International Journal for Numerical Methods in Engineering*, 82(5):617–636, 2010.

M. Bogomolny and O. Amir. Conceptual design of reinforced concrete structures using topology optimization with elastoplastic material modeling. *International Journal for Numerical Methods in Engineering*, 90(13):1578–1597, 2012.

BIBLIOGRAPHY

L. Brillouin. *Wave propagation in periodic structures: electric filters and crystal lattices*. Courier Corporation, 2003.

M. Bruggi. Generating strut-and-tie patterns for reinforced concrete structures using topology optimization. *Computers & Structures*, 87(23):1483–1495, 2009.

M. Bruggi. On the automatic generation of strut and tie patterns under multiple load cases with application to the aseismic design of concrete structures. *Advances in Structural Engineering*, 13(6):1167–1181, 2010.

M. Bruggi and A. Taliercio. Maximization of the fundamental eigenfrequency of micropolar solids through topology optimization. *Structural and Multidisciplinary Optimization*, 46(4):549–560, 2012.

T. Buhl, C. B. Pedersen, and O. Sigmund. Stiffness design of geometrically nonlinear structures using topology optimization. *Structural and Multidisciplinary Optimization*, 19(2):93–104, 2000.

S. Calvel and M. Mongeau. Topology optimization of a mechanical component subject to dynamic constraints. Technical report, Technical Report LAAS N0, 2005.

F. Cervera, L. Sanchis, J. Sanchez-Perez, R. Martinez-Sala, C. Rubio, F. Meseguer, C. Lopez, D. Caballero, and J. Sánchez-Dehesa. Refractive acoustic devices for airborne sound. *Physical review letters*, 88(2):23902, 2001.

S. Chen, W. Chen, and S. Lee. Level set based robust shape and topology optimization

under random field uncertainties. *Structural and Multidisciplinary Optimization*, 41(4):507–524, 2010.

A. Cleland, D. Schmidt, and C. Yung. Thermal conductance of nanostructured phononic crystals. *Physical Review B*, 64(17):172301, 2001.

R. W. Clough and J. Penzien. Dynamics of structures, berkeley: Computers & structures, 1995.

S. J. Cox and D. C. Dobson. Band structure optimization of two-dimensional photonic crystals in h-polarization. *Journal of Computational Physics*, 158(2):214–224, 2000.

O. Curadelli and M. Amani. Integrated structure-passive control design of linear structures under seismic excitations. *Engineering Structures*, 81:256–264, 2014.

R. L. Dailey. Eigenvector derivatives with repeated eigenvalues. *Aiaa Journal*, 27(4): 486–491, 1989.

D. Darwin and D. A. Pecknold. Nonlinear biaxial stress-strain law for concrete. *Journal of Engineering Mechanics*, 103(ASCE 12839 Proceeding), 1977.

A. Diaz and M. Bendsøe. Shape optimization of structures for multiple loading conditions using a homogenization method. *Structural Optimization*, 4(1):17–22, 1992.

A. Diaz, A. Haddow, and L. Ma. Design of band-gap grid structures. *Structural and Multidisciplinary Optimization*, 29(6):418–431, 2005.

BIBLIOGRAPHY

D. C. Dobson and S. J. Cox. Maximizing band gaps in two-dimensional photonic crystals. *SIAM Journal on Applied Mathematics*, 59(6):2108–2120, 1999.

I. Doltsinis and Z. Kang. Robust design of structures using optimization methods. *Computer Methods in Applied Mechanics and Engineering*, 193(23):2221–2237, 2004.

J. Du and N. Olhoff. Topological design of freely vibrating continuum structures for maximum values of simple and multiple eigenfrequencies and frequency gaps. *Structural and Multidisciplinary Optimization*, 34(2):91–110, 2007.

R. Fox and M. Kapoor. Rates of change of eigenvalues and eigenvectors. *AIAA journal*, 6(12):2426–2429, 1968.

M. Friswell. The derivatives of repeated eigenvalues and their associated eigenvectors. *Journal of vibration and acoustics*, 118(3):390–397, 1996.

A. T. Gaynor, J. K. Guest, and C. D. Moen. Reinforced concrete force visualization and design using bilinear truss-continuum topology optimization. *Journal of Structural Engineering*, 139(4):607–618, 2012.

G. A. Gazonas, D. S. Weile, R. Wildman, and A. Mohan. Genetic algorithm optimization of phononic bandgap structures. *International journal of solids and structures*, 43(18):5851–5866, 2006.

BIBLIOGRAPHY

I. Gidaris and A. A. Taflanidis. Performance assessment and optimization of fluid viscous dampers through life-cycle cost criteria and comparison to alternative design approaches. *Bulletin of Earthquake Engineering*, 13(4):1003–1028, 2015.

C. Goffaux and J. Sánchez-Dehesa. Two-dimensional phononic crystals studied using a variational method: Application to lattices of locally resonant materials. *Physical Review B*, 67(14):144301, 2003.

H. Guan. Effect of sizes and positions of web openings on strut-and-tie models of deep beams. *Advances in Structural Engineering*, 8(1):69–84, 2005.

H. Guan and J.-H. Doh. Development of strut-and-tie models in deep beams with web openings. *Advances in Structural Engineering*, 10(6):697–711, 2007.

J. K. Guest. Imposing maximum length scale in topology optimization. *Structural and Multidisciplinary Optimization*, 37(5):463–473, 2009a.

J. K. Guest. Topology optimization with multiple phase projection. *Computer Methods in Applied Mechanics and Engineering*, 199(1):123–135, 2009b.

J. K. Guest and T. Igusa. Structural optimization under uncertain loads and nodal locations. *Computer Methods in Applied Mechanics and Engineering*, 198(1):116–124, 2008.

J. K. Guest and C. D. Moen. Reinforced concrete design with topology optimization.

In *Proceedings of the 19th Analysis & Computation Specialty Conference. Reston: American Society of Civil Engineers*, pages 445–454, 2010.

J. K. Guest and L. C. Smith Genut. Reducing dimensionality in topology optimization using adaptive design variable fields. *International journal for numerical methods in engineering*, 81(8):1019–1045, 2010.

J. K. Guest, J. H. Prévost, and T. Belytschko. Achieving minimum length scale in topology optimization using nodal design variables and projection functions. *International journal for numerical methods in engineering*, 61(2):238–254, 2004a.

J. K. Guest, J. H. Prévost, and T. Belytschko. Achieving minimum length scale in topology optimization using nodal design variables and projection functions. *International journal for numerical methods in engineering*, 61(2):238–254, 2004b.

J. K. Guest, A. Asadpoure, and S.-H. Ha. Eliminating beta-continuation from heaviside projection and density filter algorithms. *Structural and Multidisciplinary Optimization*, 44(4):443–453, 2011a.

J. K. Guest, A. Asadpoure, and S.-H. Ha. Eliminating beta-continuation from heaviside projection and density filter algorithms. *Structural and Multidisciplinary Optimization*, 44(4):443–453, 2011b.

T. Hahn. *International Tables for Crystallography, Space-Group Symmetry*. Springer Science & Business Media, 2005.

BIBLIOGRAPHY

S. Halkjær and O. Sigmund. Optimization of beam properties with respect to maximum band-gap. In *Mechanics of the 21st Century, Procedings of 21st International Congress of Theoretical and Applied Mechanics*. IUTAM, Warsaw, Poland, 2004.

S. Halkjær, O. Sigmund, and J. S. Jensen. Maximizing band gaps in plate structures. *Structural and Multidisciplinary Optimization*, 32(4):263–275, 2006.

A.-C. Hladky-Hennion and J.-N. Decarpigny. Analysis of the scattering of a plane acoustic wave by a doubly periodic structure using the finite element method: Application to alberich anechoic coatings. *The Journal of the Acoustical Society of America*, 90(6):3356–3367, 1991.

K. Ho, C. Chan, and C. Soukoulis. Existence of a photonic gap in periodic dielectric structures. *Physical Review Letters*, 65(25):3152, 1990.

G. W. Housner. Characteristics of strong-motion earthquakes. *Bulletin of the Seismological Society of America*, 37(1):19–31, 1947.

H. Hu. On some variatinal principles in the theory of elasticity and the theory of plasticity. *Scientia Sinica*, 4:33, 1955.

M. Hussein. Reduced bloch mode expansion for periodic media band structure calculations. *Proceedings of the Royal Society A: Mathematical, Physical and Engineering Science*, 465(2109):2825, 2009.

BIBLIOGRAPHY

T. Igusa. A unified mode combination theory for stationary response of structural systems. *Earthquake engineering & structural dynamics*, 21(2):109–126, 1992.

J. S. Jensen. Phononic band gaps and vibrations in one-and two-dimensional mass–spring structures. *Journal of Sound and Vibration*, 266(5):1053–1078, 2003.

J. S. Jensen. Topology optimization of dynamics problems with padé approximants. *International journal for numerical methods in engineering*, 72(13):1605–1630, 2007.

J. S. Jensen and O. Sigmund. Systematic design of photonic crystal structures using topology optimization: Low-loss waveguide bends. *Applied Physics Letters*, 84(12): 2022–2024, 2004.

C. Jog. Topology design of structures subjected to periodic loading. *Journal of Sound and Vibration*, 253(3):687–709, 2002.

Z. Kang, X. Zhang, S. Jiang, and G. Cheng. On topology optimization of damping layer in shell structures under harmonic excitations. *Structural and Multidisciplinary Optimization*, 46(1):51–67, 2012.

Y. Kawabe and S. Yoshida. Structural optimization by density distribution for maximization of natural frequency. *Journal of Mechanical Design*, 118(1):157–159, 1996.

A. Khelif, A. Choujaa, B. Djafari-Rouhani, M. Wilm, S. Ballandras, and V. Laude.

BIBLIOGRAPHY

Trapping and guiding of acoustic waves by defect modes in a full-band-gap ultrasonic crystal. *Physical Review B*, 68(21):214301, 2003.

N. Khot, V. Venkayya, H. Oz, R. Grandhi, and F. Eastep. Optimal structural design with control gain norm constraint. *AIAA Journal*, 26(5):604–611, 1988.

H. Kim and G. Baker. Topology optimization for reinforced concrete design. In *WCCM V fifth world congress on computational mechanics. Vienna, Austria*. Citeseer, 2002.

H. A. Kim and G. Baker. Topology optimisation of reinforced concrete structures. In *Computational Mechanics-New Frontiers for the New Millennium: proceedings for the 1st Asian-Pacific congress on computational mechanics*, volume 2, pages 1251–1256. Citeseer, 2001.

T. S. Kim and Y. Y. Kim. Mac-based mode-tracking in structural topology optimization. *Computers & Structures*, 74(3):375–383, 2000.

I. Kosaka and C. C. Swan. A symmetry reduction method for continuum structural topology optimization. *Computers & Structures*, 70(1):47–61, 1999.

L. A. Krog and N. Olhoff. Optimum topology and reinforcement design of disk and plate structures with multiple stiffness and eigenfrequency objectives. *Computers & Structures*, 72(4):535–563, 1999.

D. Kuchma, S. Yindeesuk, T. Nagle, J. Hart, and H. H. Lee. Experimental validation

of strut-and-tie method for complex regions. *ACI Structural Journal*, 105(5):578, 2008.

P. Kumar. Optimal force transmission in reinforced concrete deep beams. *Computers & Structures*, 8(2):223–229, 1978.

H.-G. Kwak and S.-H. Noh. Determination of strut-and-tie models using evolutionary structural optimization. *Engineering Structures*, 28(10):1440–1449, 2006.

E. Landry, M. Hussein, and A. McGaughey. Complex superlattice unit cell designs for reduced thermal conductivity. *Physical Review B*, 77(18):184302, 2008.

H.-J. Lee, W. Choi, and J.-J. Lee. Development of the stress path search model using triangulated irregular network and refined evolutionary structural optimization. *Journal of The Korean Society of Agricultural Engineers*, 49(6):37–46, 2007.

L.-J. Leu, C.-W. Huang, C.-S. Chen, and Y.-P. Liao. Strut-and-tie design methodology for three-dimensional reinforced concrete structures. *Journal of structural engineering*, 132(6):929–938, 2006.

K. Leung and Y. Liu. Full vector wave calculation of photonic band structures in face-centered cubic dielectric media. Technical report, DTIC Document, 1990.

X.-F. Li, X. Ni, L. Feng, M.-H. Lu, C. He, and Y.-F. Chen. Tunable unidirectional sound propagation through a sonic-crystal-based acoustic diode. *Physical review letters*, 106(8):084301, 2011.

BIBLIOGRAPHY

Q. Q. Liang. *Performance-based Optimization of Structures: Theory and applications*. CRC Press, 2005.

Q. Q. Liang. Performance-based optimization of strut-and-tie models in reinforced concrete beam-column connections. In *Proceedings of the 10th East Asia-Pacific Conference on Structural Engineering and Construction: Materials, Experimentation, Maintenance and Rehabilitation (EASEC-10)*, volume 4, pages 347–352. Asian Institute of Technology, 2006.

Z.-Q. Lin, H. C. Gea, and S.-T. Liu. Design of piezoelectric energy harvesting devices subjected to broadband random vibrations by applying topology optimization. *Acta Mechanica Sinica*, 27(5):730–737, 2011.

S. Liu and H. Qiao. Topology optimization of continuum structures with different tensile and compressive properties in bridge layout design. *Structural and Multidisciplinary Optimization*, 43(3):369–380, 2011.

W. K. Liu, T. Belytschko, and A. Mani. Random field finite elements. *International Journal for Numerical Methods in Engineering*, 23(10):1831–1845, 1986.

X.-b. Liu and Q.-c. Meng. On the convergence of finite element method with different extension-compression elastic modulus. *JOURNAL-BEIJING UNIVERSITY OF AERONAUTICS AND ASTRONAUTICS*, 28(2; ISSU 114):231–234, 2002.

Z.-F. Liu, B. Wu, and C.-F. He. Systematic topology optimization of solid-solid

phononic crystals for multiple separate band-gaps with different polarizations. *Ultrasonics*, 65:249 – 257, 2016.

J. Lógó. New type of optimality criteria method in case of probabilistic loading conditions#. *Mechanics Based Design of Structures and Machines*, 35(2):147–162, 2007.

J. Lógó, M. Ghaemi, and M. M. Rad. Optimal topologies in case of probabilistic loading: the influence of load correlation. *Mechanics based design of structures and machines*, 37(3):327–348, 2009.

Y. Lu and A. Srivastava. Variational methods for phononic calculations. *Wave Motion*, 60:46–61, 2016.

E. Lund. Finite element based design sensitivity analysis and optimization. *Institute of Mechanical Engineering, Aalborg University, Denmark*, 1994.

Y. Luo and Z. Kang. Layout design of reinforced concrete structures using two-material topology optimization with drucker–prager yield constraints. *Structural and Multidisciplinary Optimization*, 47(1):95–110, 2013.

L. D. Lutes. *Stochastic analysis of structural and mechanical vibrations*. Prentice Hall, 1997.

Z.-D. Ma, N. Kikuchi, and I. Hagiwara. Structural topology and shape optimization for a frequency response problem. *Computational mechanics*, 13(3):157–174, 1993.

BIBLIOGRAPHY

Z.-D. Ma, N. Kikuchi, and H.-C. Cheng. Topological design for vibrating structures. *Computer methods in applied mechanics and engineering*, 121(1):259–280, 1995.

M. Maldovan, C. K. Ullal, W. C. Carter, and E. L. Thomas. Exploring for 3d photonic bandgap structures in the 11 fcc space groups. *Nature materials*, 2(10):664–667, 2003.

P. Marti. On plastic analysis of reinforced concrete. Rep. No. 104, Institute of Structural Engineers, ETH, Zurich, Switzerland, 1980.

P. Marti. Basic tools of reinforced concrete beam design. In *Journal Proceedings*, volume 82, pages 46–56, 1985.

R. Martinezsala, J. Sancho, J. Sanchez, V. Gómez, J. Llinares, and F. Meseguer. Sound-attenuation by sculpture. *Nature*, 378(6554):241–241, 1995.

H. Men, K. Y. Lee, R. M. Freund, J. Peraire, and S. G. Johnson. Robust topology optimization of three-dimensional photonic-crystal band-gap structures. *Optics express*, 22(19):22632–22648, 2014.

W. C. Mills-Curran. Calculation of eigenvector derivatives for structures with repeated eigenvalues. *AIAA journal*, 26(7):867–871, 1988.

W. C. Mills-Curran. Comment on" eigenvector derivatives with repeated eigenvalues". *AIAA journal*, 28(10):1846–1846, 1990.

BIBLIOGRAPHY

S. Min, N. Kikuchi, Y. Park, S. Kim, and S. Chang. Optimal topology design of structures under dynamic loads. *Structural optimization*, 17(2-3):208–218, 1999.

S. Minagawa and S. Nemat-Nasser. Harmonic waves in three-dimensional elastic composites. *International Journal of Solids and Structures*, 12(11):769, 1976.

C. D. Moen and J. K. Guest. Reinforced concrete analysis and design with truss topology optimization. In *3rd fib international congress*, 2010.

E. Morsch. Concrete steel construction,(translation of the 3rd german edition of der eisenbetonbau by e. p. goodrich), 1909.

P. Nagarajan and M. Pillai. Analysis and design of simply supported deep beams using strut and tie method. *Advances in Structural Engineering*, 11(5):491–499, 2008a.

P. Nagarajan and T. M. Pillai. Development of strut and tie models for simply supported deep beams using topology optimization. *Sonklanakarin Journal of Science and Technology*, 30(5):641, 2008b.

S. Nemat-Nasser. General variational methods for waves in elastic composites. *Journal of Elasticity*, 2(2):73–90, 1972.

S. Nemat-Nasser. Refraction characteristics of phononic crystals. *Acta Mechanica Sinica*, 31(4):481–493, 2015a. ISSN 0567-7718.

BIBLIOGRAPHY

S. Nemat-Nasser. Anti-plane shear waves in periodic elastic composites: band structure and anomalous wave refraction. In *Proc. R. Soc. A*, volume 471, page 20150152. The Royal Society, 2015b.

S. Nemat-Nasser, F. Fu, and S. Minagawa. Harmonic waves in one-, two-and three-dimensional composites: Bounds for eigenfrequencies. *International Journal of Solids and Structures*, 11(5):617, 1975.

B. Niu, J. Yan, and G. Cheng. Optimum structure with homogeneous optimum cellular material for maximum fundamental frequency. *Structural and Multidisciplinary Optimization*, 39(2):115–132, 2009.

I. Ojalvo. Efficient computation of mode-shape derivatives for large dynamic systems. *AIAA journal*, 25(10):1386–1390, 1987.

N. Olhoff, B. Niu, and G. Cheng. Optimum design of band-gap beam structures. *International Journal of Solids and Structures*, 49(22):3158–3169, 2012.

J.-S. Ou and N. Kikuchi. Integrated optimal structural and vibration control design. *Structural optimization*, 12(4):209–216, 1996.

J. H. Page, S. Yang, X. Liu, M. L. Cowan, C. T. Chan, and P. Sheng. Tunneling and dispersion in 3d phononic crystals. *Zeitschrift f Kristallographie*, 220:859, 2005.

E. Pagnacco, S. Lambert, L. Khalij, and D. Rade. Design optimisation of linear struc-

tures subjected to dynamic random loads with respect to fatigue life. *International Journal of Fatigue*, 43:168–177, 2012.

N. L. Pedersen. Maximization of eigenvalues using topology optimization. *Structural and multidisciplinary optimization*, 20(1):2–11, 2000.

Z. Qiao, Z. Weihong, Z. Jihong, and G. Tong. Layout optimization of multi-component structures under static loads and random excitations. *Engineering Structures*, 43:120–128, 2012.

W. Ritter. Die bauweise hennebique (hennebiques construction method). 1899.

J. Rong, Y. Xie, X. Yang, and Q. Liang. Topology optimization of structures under dynamic response constraints. *Journal of Sound and Vibration*, 234(2):177–189, 2000.

J. H. Rong, Z. L. Tang, Y. M. Xie, and F. Y. Li. Topological optimization design of structures under random excitations using sqp method. *Engineering Structures*, 56:2098–2106, 2013.

E. Sandgren and T. Cameron. Robust design optimization of structures through consideration of variation. *Computers & structures*, 80(20):1605–1613, 2002.

M. Sarkisian, E. Long, D. Shook, and C. Doo. Optimization tools for the design of structures. In *Proceedings of 78th convention for structural engineers association of California (SEAOC). San Diego, CA*, 2009.

BIBLIOGRAPHY

J. Schlaich and K. Schafer. Design and detailing of structural concrete using strut-and-tie models. *Structural Engineer*, 69:113–25, 1991.

J. Schlaich, K. Schäfer, and M. Jennewein. Toward a consistent design of structural concrete. *PCI journal*, 32(3):74–150, 1987.

W. Setyawan and S. Curtarolo. High-throughput electronic band structure calculations: Challenges and tools. *Computational Materials Science*, 49(2):299–312, 2010.

A. P. Seyranian, E. Lund, and N. Olhoff. Multiple eigenvalues in structural optimization problems. *Structural optimization*, 8(4):207–227, 1994.

L. Shu, M. Y. Wang, Z. Fang, Z. Ma, and P. Wei. Level set based structural topology optimization for minimizing frequency response. *Journal of Sound and Vibration*, 330(24):5820–5834, 2011.

O. Sigmund. *Design of Materials Structures Using Topology Optimization*. Department of Solid Mechanics, Technical University of Denmark, 1994.

O. Sigmund and J. S. Jensen. Systematic design of phononic band–gap materials and structures by topology optimization. *Philosophical Transactions of the Royal Society of London. Series A: Mathematical, Physical and Engineering Sciences*, 361 (1806):1001–1019, 2003.

C. A. Soto and A. R. Diaz. Layout of plate structures for improved dynamic response

using a homogenization method. *ASME DES ENG DIV PUBL DE, ASME, NEW YORK, NY,(USA), 1993,*, 65:667–674, 1993.

A. Srivastava. Gpu accelerated variational methods for fast phononic eigenvalue solutions. In *SPIE Smart Structures and Materials+ Nondestructive Evaluation and Health Monitoring*, pages 94381F–94381F. International Society for Optics and Photonics, 2015.

A. Srivastava and S. Nemat-Nasser. Mixed-variational formulation for phononic band-structure calculation of arbitrary unit cells. *Mechanics of Materials*, 74:67–75, 2014.

L. L. Stromberg, A. Beghini, W. F. Baker, and G. H. Paulino. Application of layout and topology optimization using pattern gradation for the conceptual design of buildings. *Structural and Multidisciplinary Optimization*, 43(2):165–180, 2011.

A. Sukhovich, L. Jing, and J. Page. Negative refraction and focusing of ultrasound in two-dimensional phononic crystals. *Physical Review B*, 77(1):014301, 2008.

K. Svanberg. The method of moving asymptotesa new method for structural optimization. *International journal for numerical methods in engineering*, 24(2):359–373, 1987.

A. A. Taflanidis and J. T. Scruggs. Performance measures and optimal design of linear structural systems under stochastic stationary excitation. *Structural Safety*, 32(5):305–315, 2010.

BIBLIOGRAPHY

D. Tcherniak. Topology optimization of resonating structures using simp method. *International Journal for Numerical Methods in Engineering*, 54(11):1605–1622, 2002.

L. H. Tenek and I. Hagiwara. Static and vibrational shape and topology optimization using homogenization and mathematical programming. *Computer methods in applied mechanics and engineering*, 109(1):143–154, 1993.

S. L. Vatanabe, G. H. Paulino, and E. C. Silva. Maximizing phononic band gaps in piezocomposite materials by means of topology optimization. *The Journal of the Acoustical Society of America*, 136(2):494–501, 2014.

I. A. Veres and T. Berer. Complexity of band structures: Semi-analytical finite element analysis of one-dimensional surface phononic crystals. *Physical Review B*, 86(10):104304, 2012.

K. Washizu. On the variational principles of elasticity and plasticity. Technical report, Contract N5ori-07833,MIT, 1955.

S. R. White, J. W. Wilkins, and M. P. Teter. Finite-element method for electronic structure. *Physical Review B*, 39(9):5819, 1989.

S. Yang, J. Page, Z. Liu, M. Cowan, C. Chan, and P. Sheng. Ultrasound tunneling through 3d phononic crystals. *Physical review letters*, 88(10):104301, 2002.

BIBLIOGRAPHY

S. Yang, J. Page, Z. Liu, M. Cowan, C. Chan, and P. Sheng. Focusing of sound in a 3d phononic crystal. *Physical review letters*, 93(2):24301, 2004.

X. Yang and Y. Li. Topology optimization to minimize the dynamic compliance of a bi-material plate in a thermal environment. *Structural and Multidisciplinary Optimization*, 47(3):399–408, 2013.

Y. Yang, J. K. Guest, and C. D. Moen. Computer-generated force flow paths for concrete design: An alternative to traditional strut-and-tie models. In *Proc. of the 2013 PCI Convention and National Bridge Conference, Grapevine, TX*, 2013.

G. H. Yoon. Structural topology optimization for frequency response problem using model reduction schemes. *Computer Methods in Applied Mechanics and Engineering*, 199(25):1744–1763, 2010.

N. Zen, T. A. Puurtinen, T. J. Isotalo, S. Chaudhuri, and I. J. Maasilta. Engineering thermal conductance using a two-dimensional phononic crystal. *Nature communications*, 5, 2014.

Z. Zhang and S. Satpathy. Electromagnetic wave propagation in periodic structures: Bloch wave solution of maxwell equations. *Physical review letters*, 65(21):2650, 1990.

M. Zhou and G. Rozvany. The coc algorithm, part ii: topological, geometrical and

generalized shape optimization. *Computer Methods in Applied Mechanics and Engineering*, 89(1-3):309–336, 1991.

Vita

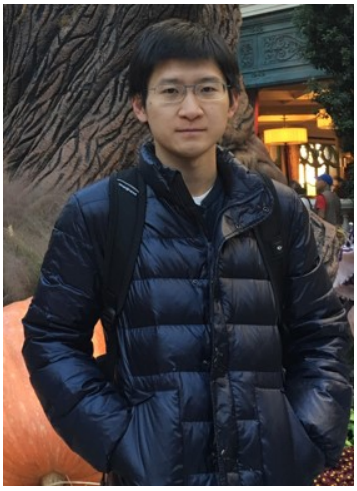

Yang Yang was born in Beijing, China. He received the B.S. degree in Civil Engineering from Tongji University in 2008, and enrolled in the Civil Engineering M.S.E. program at Syracuse University in 2009. Then he pursued to the Ph.D. degree at Johns Hopkins University in 2011. His research focuses on topology optimization on eigenvalue problems.